Effects of Noncommuting Charges in Quantum Information and Thermodynamics

by

Shayan Majidy

A thesis
presented to the University of Waterloo
in fulfilment of the
thesis requirement for the degree of
Doctor of Philosophy
in
Physics (Quantum Information)

Waterloo, Ontario, Canada, 2024

Examining Committee Membership

The following served on the Examining Committee for this thesis. The decision of the Examining Committee is by majority vote.

External Examiner:	Christopher Jarzynski Distinguished Professor, Dept. of Chemistry and Biochemistry, University of Maryland
Supervisor:	Raymond Laflamme Professor, Dept. of Physics and Astronomy, University of Waterloo
Internal Member:	Alan Jamison Assistant Professor, Dept. of Physics and Astronomy, University of Waterloo
Internal-External Member:	Christopher Wilson Professor, Dept. of Electrical and Computer Engineering, University of Waterloo
Other Member(s):	Alex May Adjunt Faculty, Dept. of Physics and Astronomy, University of Waterloo

Author's Declaration

This thesis consists of material all of which I authored or co-authored: see Statement of Contributions included in the thesis. This is a true copy of the thesis, including any required final revisions, as accepted by my examiners.

I understand that my thesis may be made electronically available to the public.

Statement of Contributions

Chapters 2 to 6 of this thesis are based on, respectively, references [1, 2, 3, 4, 5]. Excerpts of Chapters 1 and 7 also draw from reference [1]. Below, I outline my contributions to these works.

[1] **S. Majidy**, W. F. Braasch, Jr., A. Lasek, T. Upadhyaya, A. Kalev, and N. Yunger Halpern, "Noncommuting conserved charges in quantum thermodynamics and beyond," Nat. Rev. Phys. (2023).

- With NYH, I helped conduct a literature search on noncommuting charges and categorize the findings into five groups, assigning each to different co-authors, including myself. I read and summarized the papers in my category and designed the figures for all sections. I then played a key role in addressing the editor's and referees' comments.

[2] N. Yunger Halpern and **S. Majidy**, "How to build Hamiltonians that transport noncommuting charges in quantum thermodynamics," npj Quantum Information 8, 10 (2022)

- I conducted all of the proofs for each result, the $\mathfrak{su}(3)$ example, the superconducting-qutrit details, the Supplementary Notes, and led the referee revisions.

[3] **S. Majidy**, A. Lasek, D. A. Huse, and N. Yunger Halpern, "Non-abelian symmetry can increase entanglement entropy," Phys. Rev. B, 107, 045102 (2023).

- All authors contributed to designing the models. I conducted all of the analytic calculations with guidance from DH on how to do so. I performed the numerics for the microcanonical subspace analysis. I assisted AL with the numerics for the approximate microcanonical subspace analysis. I drafted the manuscript and implemented the referee revisions.

[4] **S. Majidy**, U. Agrawal, S. Gopalakrishnan, A. Potter, R. Vasseur, and N. Yunger Halpern "Critical phase and spin sharpening in SU(2)-symmetric monitored quantum circuits," Phys. Rev. B 108, 054307 (2023).

- I performed all of the numerics, drafted the manuscript and implemented the referee revisions.

[5] **S. Majidy** "Noncommuting charges' effect on the thermalization of local observables," arXiv 2403.13046 (2024).

- I was the sole contributor.

The following works were completed during my Ph.D. [6, 7, 8, 9, 10] but are not included in this thesis.

[6] **S. Majidy**, H. Katiyar, G. Anikeeva, J. Halliwell, and R. Laflamme, "Exploration of an augmented set of Leggett-Garg inequalities using a noninvasive continuous-in-time velocity measurement," Phys. Rev. A, 100, 042325 (2019).

[7] **S. Majidy**, J. J. Halliwell, and R. Laflamme, "Detecting violations of macrorealism when the original Leggett-Garg inequalities are satisfied," Phys. Rev. A 103, 062212 (2021)

[8] **S. Majidy** "A unification of the coding theory and OAQEC perspective on hybrid codes," Int. J. Theor. Phys. 62.8: 177 (2023).

[9] **S. Majidy**, C. Wilson, and R. Laflamme, "Building quantum computers: A practical introduction," Cambridge University Press, (2024).

[10] **S. Majidy** "Addressing misconceptions in university physics: A review and experiences from quantum physics educators," arXiv 2405.20923 (2024).

Abstract

The advancement of quantum theory is rooted in challenging established assumptions. This trend persists as quantum theory extends into other fields, including thermodynamics. One such assumption in thermodynamics is that conserved quantities, known as charges, commute. Lifting this assumption has led to a new subfield, noncommuting charges [1], at the intersection of quantum information and quantum thermodynamics. The work presented in this thesis identifies various effects of noncommuting charges and extends the topic to many-body physics and experiments.

Initially, the field's findings were conveyed in abstract information-theoretic terms. To transition these findings to experimental practice and tie them to many-body physics, constructing relevant Hamiltonians is essential. We introduce a method for constructing Hamiltonians that globally conserve noncommuting quantities while facilitating their local transport [2].

Having demonstrated the testability of noncommuting-charge physics, we aim to delineate its effects. To do so, we construct analogous models that differ in whether their charges commute [3]. We find that noncommuting models exhibit higher entanglement entropies. Since entanglement accompanies thermalization, our result challenges previous assertions that charges' noncommutation hinders thermalization.

Motivated by understanding noncommuting charges' effects on entanglement, we introduce them into monitored quantum circuits. Monitored quantum circuits typically transition from a highly entangled volume-law phase to a less entangled area-law phase as one increases the rate of measurements. This holds for monitored quantum circuits with no charges and commuting ones. We find that by introducing noncommuting charges into monitored quantum circuits, the area-law phase becomes replaced with a critical phase [4]. Since critical phases are characterized by long-range entanglement, this result reinforces entanglement enhancement by noncommuting charges.

Finally, we revisit the puzzle of whether noncommuting charges promote or hinder thermalization. Most quantum many-body systems thermalize; some don't. In those that don't, what effect do noncommuting charges have? One type of system that does not thermalize is a system whose Hamiltonian has so-called dynamical symmetries (or spectrum-generating algebras). We find that noncommuting charges promote thermalization by reducing the dynamical symmetries in a system [5].

Acknowledgements

First and foremost, I want to express my deep gratitude to Raymond Laflamme and Nicole Yunger Halpern. Ray, no number of birthday conferences I organize could ever equal your generosity. Thank you for taking a chance on me and offering unwavering support. You've shaped more than just my career; you've been a great role model. Nicole, I am immensely grateful for the time and energy you've invested in my development and for the scientific principles you've imparted. Like quantum steampunk, you are a unique blend of traditional wisdom with modern insights. The mentorship of a renowned senior scientist and a rising star has unique advantages, and I was lucky to have both.

I'm grateful for the serendipitous events that led me to other remarkable mentors. A cold email to Jonathan J. Halliwell led to many insightful discussions and two exciting projects. Jonathan, your generosity in sharing your expertise and unwavering support for my career is deeply appreciated. Becoming a teaching assistant for Christopher Wilson sparked the passion project of my Ph.D.—writing a textbook with Chris and Ray. Chris, I am grateful for the countless hours you devoted to answering my varied questions about quantum hardware and for serving on *all three* of my Ph.D. committees. Forming a quantum thermodynamics reading group introduced me to Eduardo Martin-Martinez and the vibrant 'Barrio RQI.' Edu, you've been my rock during difficult moments. Thank you for having faith in me, even when I lacked it myself. I owe much of my mental well-being to you. I'm unsure how I fell into the orbit of Sarang Gopalakrishnan, but I'm lucky I did. It's hard to say what's more brazen: my asking him to co-author a Banting application soon after we met or his immediate agreement. Sarang, thank you for making work fun, going above and beyond during my postdoc applications, and introducing me to the finer things in life, like dinners at 7/11. Finally, my greatest stroke of luck was selecting "Jane Russwurm" when booking my first meeting at the Writing and Communication Centre. Jane, your support with my Vanier and Banting applications exceeded my expectations. I wouldn't have won either without you.

Special thanks go to Christopher Jarzynski, John Preskill, Michael Gullans, Alan Jamison, and Alex May. Chris, I was overjoyed that you'd agreed to serve on my committee. Having you as a member was a special treat. John, thank you for the eloquent foreword for our textbook. Having you write it, after years of studying how you write science, was poetic. Michael, thank you for the warm welcome to your research group. I've greatly appreciated the chance to collaborate and learn from you, and I am eager to continue doing so. Alan and Alex, thank you for agreeing to join my examining committee. The prospect of forming a committee in a day and advancing the examination by three months could have been stressful, but because of you two, it wasn't.

I am grateful to the rest of my academic family. I sincerely thank Mike DeWeese, Roger Melko, Pooya Ronagh, and Martin Williams for being wonderful sources of advice as I navigate the various academic career stages. I'd also like to thank Vir Bulchandani, Andrew Cameron, Anirban Chowdhury, John Donohue, Matt Duschene, Emiliia Dyrenkova, Aleksander Lasek, Junan Lin, Zachary Mann, Alex May, Benjamin McLellan, Ryan Plestid, Abhinav Prem, and Mike Vasmer for your friendship and for the various feedback you've given on papers and fellowship applications over my PhD. I'm lucky to have you all.

I am most grateful for my family. I was blessed to be raised by four remarkable individuals—my mother Roya, my uncle Payam, and my aunties Sahideh and Sohilah—who sacrificed immensely for me. A decade later, my family expanded to include Arjomand and Sahba, who consistently put my needs above theirs. Finally, to my wife, Hasti, you are my everything. Thank you for enduring the challenges of being married to a PhD student.

Dedication

This work is dedicated to my beloved Hasti and our soon-to-arrive child.

Table of Contents

List of Figures

List of Tables

Chapter 1

Introduction

Thermodynamics problems have surprisingly many similarities with fairy tales. For example, most of them begin with a familiar opening. In thermodynamics, the phrase "Consider an isolated box of particles" serves a similar purpose to "Once upon a time" in fairy tales—both serve as a gateway to their respective worlds. Additionally, both have been around for a long time. Thermodynamics emerged in the Victorian era to help us understand steam engines, while Beauty and the Beast and Rumpelstiltskin, for example, originated about 4000 years ago. Moreover, each conclude with important lessons. In thermodynamics, we learn hard truths such as the futility of defying the second law, while fairy tales often impart morals like the risks of accepting apples from strangers. The parallels go on; both feature archetypal characters—such as wise old men and fairy godmothers versus ideal gases and perfect insulators—and simplified models of complex ideas, like portraying clear moral dichotomies in narratives versus assuming non-interacting particles in scientific models.

Of all the ways thermodynamic problems are like fairytales, one is most relevant to this thesis: both have experienced modern twists. In thermodynamics, the introduction of noncommuting conserved quantities, or charges, has been one such twist.

1.1 Motivation

Across physics, systems exchange conserved quantities. Such exchanges occur, for example, in electrochemical batteries, in a cooling cup of coffee, and when spins flip to align with a magnetic field. We call globally conserved quantities charges. Many of us initially

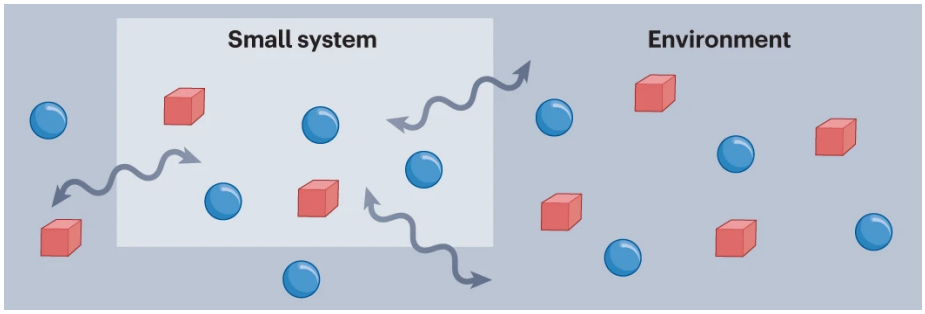

Figure 1.1: **Common thermodynamic paradigm:** A small system and large environment locally exchange quantities that are conserved globally. Common quantities include energy, as well as particles of different species.

encounter the concept of charges through the following setup from undergraduate statistical physics. Consider a global system partitioned into a small system $\mathcal{S}$ and a large environment $\mathcal{E}$. (Fig. 1.1). $\mathcal{S}$ and $\mathcal{E}$ exchange quantities which are globally conserved. Suppose that the systems are quantum. $\mathcal{S}$ may thermalize to the canonical state $\rho_{\text{can}} \propto e^{-\beta H^{(\mathcal{S})}}$ if the system and environment exchange only energy, where the energy can flow in the form of heat. The environment's inverse temperature is β, and $H^{(\mathcal{S})}$ denotes the system-of-interest Hamiltonian. If $\mathcal{S}$ and $\mathcal{E}$ exchange heat and particles, $\mathcal{S}$ may thermalize to the grand canonical state $\rho_{\text{GC}} \propto e^{-\beta(H^{(\mathcal{S})} - \mu \mathcal{N}^{(\mathcal{S})})}$. The chemical potential is μ, and $\mathcal{N}^{(\mathcal{S})}$ denotes the system-of-interest particle-number operator. This pattern extends to many exchanged quantities (electric charge, magnetization, etc.) and other thermal states. Since the exchanged quantities are conserved globally (across $\mathcal{SE}$), they are charges. Hermitian operators Q_a represent the conserved quantities; $\mathcal{S}$ has an operator $Q_a^{(\mathcal{S})}$, $\mathcal{E}$ has $Q_a^{(\mathcal{E})}$, and the global system has $Q_a^{\text{tot}} := Q_a^{(\mathcal{S})} + Q_a^{(\mathcal{E})} \equiv Q_a^{(\mathcal{S})} \otimes \mathbb{1}^{(\mathcal{E})} + \mathbb{1}^{(\mathcal{S})} \otimes Q_a^{(\mathcal{E})}$, where $\mathbb{1}$ is the identity operator. The index $a = 0, 1, \ldots, c$.

A common implicit assumption is that charges commute with each other: $[Q_a, Q_{a'}] = 0$ $\forall a, a'$. This assumption is rarely mentioned but underlies derivations of the form of thermal states [12, 13], linear-response coefficients [14], and more. However, observables' ability to fail to commute enables quintessentially quantum phenomena: uncertainty relations [15, 16], measurement disturbance [17, 18], foundational quantum tests [19, 20, 21], etc. Quantum physics, thus, compels us to lift the assumption that charges commute. Doing so has led to the discovery of new physics [1].

1.2 Familiar example

To clarify and illustrate the concept of noncommuting charges, we'll begin with a straightforward example. First, let's introduce some essential notation that will be consistently used throughout this thesis. We call a closed quantum many-body system (e.g., the composite $\mathcal{SE}$ in Fig. 1.1) a global system. N denotes the number of degrees of freedom in a global system. Often, $\mathcal{SE}$ will consist of N copies of $\mathcal{S}$. For example, N denotes the number of qubits in Fig. 1.2. Large but finite N—the mesoscale—interests us: as $N \to \infty$, $\mathcal{SE}$ grows classical, according to the correspondence principle [13]. Noncommutation enables nonclassical phenomena[1], so we should expect charges' noncommutation to influence thermodynamic phenomena at finite N. Continuing with notation, we denote by σ_a the Pauli-a operator, for $a = x, y, z$; by $\sigma_a^{(j)}$, a spin component of qubit j; and by $\sigma_a^{\text{tot}} \coloneqq \sum_j \sigma_a^{(j)}$, a total spin component. Furthermore, we ascribe to the Pauli operators σ_a eigenstates $|a\pm\rangle$ associated with the eigenvalues ± 1. Subscripts index charges (as in $\sigma_a^{(j)}$), whereas superscripts index sites or other subsystems (e.g., $\mathcal{S}$ and $\mathcal{E}$). In this and the next chapter, we often denote commuting charges, or other observables that might commute, with a tilde ($\tilde{Q}_a' s$).Tensored-on $\mathbb{1}$'s are implicit where necessary to make operators act on the appropriate Hilbert spaces.

We can now present a simple example of a system with noncommuting charges, the well-known Heisenberg model. Consider a chain of trapped ions. A few (e.g., two) qubits form $\mathcal{S}$, and the other qubits form $\mathcal{E}$. The chain constitutes a closed quantum many-body system of the sort whose internal thermalization has recently been studied theoretically and experimentally (e.g., [22, 23, 24, 25]). According to the main result of Chapter 3, one can construct a Hamiltonian H that overtly transports quanta of each σ_a locally, $\left[H, \sigma_\alpha^{(j)}\right] \neq 0$ $\forall \alpha$, while conserving the three σ_a^{tot}'s globally, $[H, \sigma_\alpha^{\text{tot}}] = 0$ $\forall \alpha$ [3]. Denote the σ_z ladder operators by $\sigma_{\pm z} \coloneqq \frac{1}{2}(\sigma_x \pm i\sigma_y)$. The operator $\sigma_{+z}^{(j)}\sigma_{-z}^{(j+1)} + \sigma_{-z}^{(j)}\sigma_{+z}^{(j+1)}$ transports one σ_z quantum from qubit $j+1$ to qubit j and vice versa, in superposition. Define ladder operators and couplings analogously for σ_x and σ_y. The Hamiltonian

$$H_{\text{Heis}}^{\text{tot}} = \sum_{\langle j,k \rangle} \sum_{\alpha=x,y,z} \left(\sigma_{+\alpha}^{(j)} \sigma_{-\alpha}^{(k)} + \sigma_{-\alpha}^{(j)} \sigma_{+\alpha}^{(k)} \right), \tag{1.1}$$

$$= \sum_{\langle j,k \rangle} \vec{\sigma}^{(j)} \cdot \vec{\sigma}^{(k)}, \tag{1.2}$$

[1] In classical mechanics, the components of the angular momentum vector do not commute under the Poisson bracket. Thus, noncommutation is not an exclusively quantum phenomenon. How nonclassical is noncommuting-charge physics is an open question we touch on in Chapter 7.

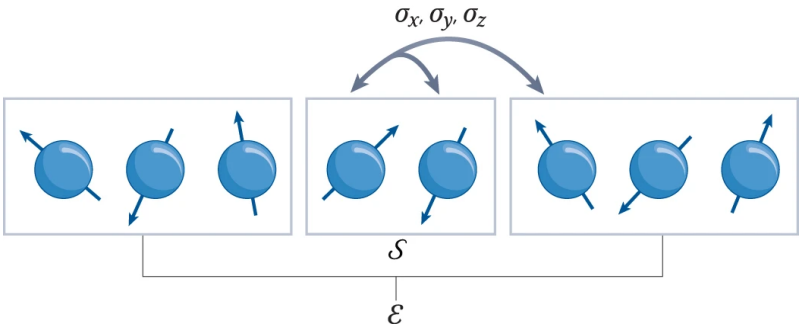

Figure 1.2: **Example thermodynamic system that conserves noncommuting charges:** Two qubits form the system $\mathcal{S}$ of interest, and the rest form the environment $\mathcal{E}$. A qubit's three spin components, $\sigma_{a=x,y,z}$, form the local noncommuting charges. The dynamics locally transport and globally conserve the charges.

where $\langle j, k \rangle$ denotes nearest neighbour coupling, transports the σ_a's locally, while conserving them globally. $H^{\text{tot}}_{\text{Heis}}$ is often expressed as in (1.2) and rarely expressed as in (1.1)—as locally transporting and globally conserving three noncommuting charges. We can easily extend $H^{\text{tot}}_{\text{Heis}}$ to nonintegrable models (which promote thermalization) by, for example, adding next-nearest neighbour coupling. This is one example of a system with noncommuting charges. Using the procedure in reference [3], we can readily find Hamiltonians that transport noncommuting charges whose subsystems extend beyond qubits and to charges beyond spin components.

1.3 Outline

Noncommuting charges have emerged as a distinct subfield within quantum thermodynamics, presenting numerous foundational questions. This thesis, the first on the subject, tackles two of these: identifying the effects of noncommuting charges and integrating these findings into broader scientific contexts, such as many-body physics and experimental research.

Chapters 2 to 6 of this thesis correspond to references [1, 2, 3, 4, 5], respectively. References [1, 2, 3, 4, 5] resulted from collaboration with some combination of the following researchers: U. Agrawal, W. F. Braasch, S. Gopalakrishnan, D. A. Huse, A. Kalev, A. Lasek, A. Potter, T. Upadhyaya, R. Vasseur, and N. Yunger Halpern. Please refer to the Statement of Contributions for details of my specific contributions to each project.

Reference [5] I authored independently. I didn't include the work published during my PhD unrelated to noncommuting charges [6, 7, 8, 9].

The chapters do not precisely replicate the respective papers; while they generally correspond, content from some papers has been shifted to chapters of others, and many sections have been rewritten. These edits eliminate redundancy and align with my evolved writing style on the topic.

Chapter 2 first reviews the history of noncommuting charge physics and then introduces new results that are relevant to this thesis. Chapter 3 introduces a method for constructing Hamiltonians that globally conserve noncommuting quantities while facilitating their local transport [2]. This work was done to help transition the abstract information-theoretic findings of noncommuting charges physics to experimental practice, numerical studies, and many-body physics.

Chapters 4 to 6 focus on uncovering new phenomena arising from the noncommutation of charges. In Chapter 4, we present analogous models that differ in whether their charges commute [3]. We find that the noncommuting charge model exhibits higher average entanglement entropy. This increase is quantified with a Page curve: consider partitioning the system into two subsystems, calculating a subsystem's entanglement entropy, and averaging the entropy over states drawn randomly from the full system's Hilbert space. The average, plotted against the subsystem's size, forms a Page curve. Entanglement typically accompanies thermalization in quantum systems, yet noncommuting charges were initially believed to impede this process. Consequently, Reference [3] opened up a now widely explored question: do noncommuting charges facilitate or obstruct thermalization?

Chapter 5 integrates noncommuting charges into monitored quantum circuits—unitary circuits interspersed with mid-circuit projective measurements—to investigate their impact on entanglement dynamics. Typically, monitored quantum circuits exhibit a transition from a highly entangled volume-law phase to a less entangled area-law phase. However, we find that noncommuting charges result in a critical phase in place of the area-law phase [4]. Characterized by long-range entanglement, among other features, this critical phase underscores the role of noncommuting charges in enhancing entanglement. Furthermore, we find a new type of phase transition within these systems, a "spin-sharpening" transition.

Chapter 6 concludes our exploration of how noncommuting charges affect thermalization. Dynamical symmetries are sufficient conditions for a system not to thermalize, according to the Eigenstate Thermalization Hypothesis (ETH) [26, 27]. In this chapter, we establish a link between noncommuting charges and dynamical symmetries, by essentially formulating a "Noether-like" theorem for dynamical symmetries. Using this theorem, we find that noncommuting charges facilitate thermalization by diminishing the number

of local observables that do not thermalize according to the ETH [5]. This further bolsters the argument that noncommuting charges are conducive to thermalization.

The thesis ends each chapter with a summary, highlighting the main findings and suggesting directions for future research. Chapter 7 presents a complete summary of the entire thesis, placing its findings within the broader context of the field's most pressing research questions. We have also included an Index that tracks where terminology is first defined.

Chapter 2

Background on noncommuting charges

Excerpts from this chapter are based on reference [1] and overlap with its text.

2.1 Overview

This chapter reviews the major developments in the physics of noncommuting charges, excluding those results presented in the later chapters of this thesis. We begin by discussing the early work on noncommuting charges in Section 2.2. This research underscores the importance of seriously considering the noncommutation of charges. The Eigenstate Thermalization Hypothesis has played a significant role in the study of noncommuting charges, and it is introduced properly in Section 2.3. We then explore some of the new physics that arises from the noncommutation of charges in Section 2.4.

2.2 Early work

In the studies discussed in this section, a recurring theme becomes apparent: the breakdown of previously understood derivations and the efforts to formulate a new framework that incorporates noncommuting charges. These findings underscore, but do not entirely encompass, the many outcomes predicated on the commutation of charges. Challenging

this assumption can be likened to removing a block from a Jenga tower[1], causing a cascade of subsequent results. Critics may contend, "If you're merely rederiving known results, isn't this field somewhat redundant?" However, the actual situation is more interesting. As researchers have worked to rebuild this theoretical Jenga tower, they have discovered ways in which noncommuting charges cause new physics. However, the discussion of new phenomena is saved for Section 2.4.

2.2.1 First appearance in the 1950s

There is a blink-and-you'll-miss-it reference to noncommuting charges in E.T. Jaynes's 1957 formalization of the maximum entropy principle [28]. The principle of maximum entropy pinpoints the state $\rho = \sum_k p_k |k\rangle\langle k|$ most reasonably attributable to a system about which one knows little. Imagine knowing about ρ only the expectation values $\langle \tilde{Q}_a \rangle$ of observables $\tilde{Q}_a$. The state obeys the constraints $\mathrm{Tr}\left(\rho \tilde{Q}_a\right) =: q_a^{\mathrm{avg}} \in \mathbb{R}$[2], plus the normalization condition $\mathrm{Tr}(\rho) = 1$. According to the maximum-entropy principle, whichever constraint-obeying state maximizes the von Neumann entropy $S_{\mathrm{vN}}(\rho) := -\mathrm{Tr}(\rho \log(\rho))$ is most reasonable. (This subsection's logarithms are base-e.) The entropy maximization encapsulates our ignorance of everything except the constraints. To maximize the entropy subject to these constraints, we introduce Lagrange multiplies $\lambda, \tilde{\mu}_a \in \mathbb{R}$. The function maximized, i.e. the Lagrange function, is

$$\mathcal{L}(\rho, \lambda, \{\tilde{\mu}_a\}) := S_{\mathrm{vN}}(\rho) - \lambda \left[\mathrm{Tr}(\rho) - 1\right] - \sum_a \tilde{\mu}_a \left[\mathrm{Tr}\left(\rho \tilde{Q}_a\right) - q_a^{\mathrm{avg}}\right]. \tag{2.1}$$

Maximizing $\mathcal{L}(\rho, \lambda, \{\tilde{\mu}_a\})$ with respect to p_k yields[3]

$$\rho = \frac{1}{Z} \exp\left(-\sum_a \tilde{\mu}_a \tilde{Q}_a\right), \tag{2.2}$$

where the $\tilde{\mu}_a$'s denote generalized chemical potentials. Maximizing with respect to λ fixes the partition function: $Z = \mathrm{Tr}\left(e^{-\sum_a \tilde{\mu}_a \tilde{Q}_a}\right)$. Maximizing with respect to $\tilde{\mu}_a$ yields

[1] Jenga is a game with a tower of wooden blocks. Players take turns removing a block and placing it on top, trying to avoid collapsing the tower.

[2] The additional notation of q_a^{avg} is introduced for clarity in the calculation of Eq. (2.1).

[3] You may be asking where the Hamiltonian and β are in Eq. (2.2). The energy is technically a charge for any closed system since H always commutes with itself. Since H is a special charge, most literature doesn't refer to it as a charge, but some do. When they do, they often label it using the subscript 0. In Eq. (2.2), $H = \tilde{Q}_0$ and $\beta = \tilde{\mu}_0$.

$q_a^{\text{avg}} = -\frac{\partial}{\partial \tilde{\mu}_a} \log(Z)$. Jaynes noted that this procedure works even if the $\tilde{Q}_a$'s do not commute. Equation (2.2) is called the generalized Gibbs ensemble (GGE) regardless of whether the charges commute [29, 30, 31, 32]. However, if the charges don't commute, we refer to the generalized Gibbs ensemble as the non-Abelian thermal state (NATS) [13],

$$\rho_{\text{NATS}} := \frac{1}{Z} e^{-\beta(H - \sum_a \mu_a Q_a)}. \tag{2.3}$$

where $\beta := \tilde{\mu}_0$ is a special label given to the Lagrange multiplier corresponding to the Hamiltonian, and all other $\mu_\alpha := \beta \tilde{\mu}_\alpha$.

Jaynes's work shows that at least one derivation of the thermal state form remains valid even when our knowledge is restricted to the expectation values of noncommuting charges. This derivation is based on information theory. However, the more physical arguments break down when charges are free not to commute, i.e., when trying to derive the ρ_{NATS}. Examples of more physical arguments include those based on resource theories (discussed in the next section) or arguments like the following by Balian and Balazs [33].

Balian and Balazs were the first to seek such a physical justification. They imagined N copies of the system of interest, in the ensemble tradition of thermodynamics. In thermodynamics, we regard all copies except one ($\mathcal{S}$) as forming an effective environment ($\mathcal{E}$) [34]. Imagine $\mathcal{S}$ exchanging energy and particles with $\mathcal{E}$. How do we typically prove that $\mathcal{S}$ is in a grand canonical state ρ_{GC}? We assume that $\mathcal{SE}$ has a fixed particle number and an energy in a small window, i.e., assume that $\mathcal{SE}$ is in a microcanonical subspace, aka a simultaneous eigenspace of the charges. Tracing out $\mathcal{E}$ from the microcanonical state yields $\mathcal{S}$'s state, which equals ρ_{GC} (if $\mathcal{S}$ and $\mathcal{E}$ couple weakly [35]). Suppose that $\mathcal{S}$ and $\mathcal{E}$ exchange several commuting charges $\tilde{Q}_a$. The microcanonical subspace is an eigenspace shared by the $\tilde{Q}_a^{\text{tot}}$'s. However, if $\mathcal{S}$ and $\mathcal{E}$ exchange noncommuting charges Q_a, the Q_a^{tot} share no eigenbasis. Thus, the charges might share no eigenspaces, and microcanonical subspaces might not exist. Balian and Balazs tried to overcome this challenge by observing that the charge densities Q_a^{tot}/N commute in the infinite-N limit: $\lim_{N\to\infty} \frac{1}{N^2}[Q_a^{\text{tot}}, Q_{a'}^{\text{tot}}] = 0$ $\forall a, a'$. However, they could not construct a well-justified generalization of microcanonical subspaces for noncommuting charges. To be clear, what is failing here is that the notion of microcanonical subspaces does not accommodate noncommuting charges.

2.2.2 Reemergence in the 2010s

For decades, no literature addressed the ability of thermodynamic charges not to commute. The topic gained attention a decade ago at the intersection of quantum information

and quantum thermodynamics. In 2014, separate work by Lostaglio and Yunger Halpern demonstrated that noncommuting charges can defy thermodynamic expectations [36, 12][4].

Lostaglio demonstrated that noncommuting charges overturn an expectation about free energy [36]. Consider a system of interest $\mathcal{S}$ in the state $\rho^{(\mathcal{S})}$ and an environment $\mathcal{E}$ in the state $\rho^{(\mathcal{E})}$, wherein $\rho^{(\mathcal{E})}$ has the generalized Gibbs ensemble form (2.2). The system and environment begin uncorrelated: $\rho^{(\mathcal{S})} \otimes \rho^{(\mathcal{E})}$. $\mathcal{S}$ and $\mathcal{E}$ have c commuting charges, $\tilde{Q}_a^{(\mathcal{S})}$ and $\tilde{Q}_a^{(\mathcal{E})}$. One can attribute to $\mathcal{S}$ a "free energy"[5] for each of its charges

$$F_a^{(\mathcal{S})}(\rho) \coloneqq -\frac{1}{\beta\mu_a} S_{\rm vN}(\rho) + \mathrm{Tr}\Big(\tilde{Q}_a \rho\Big). \tag{2.4}$$

We now evolve $\mathcal{SE}$ under a charge-conserving unitary U to a final state $\rho_{\rm f}^{(\mathcal{SE})}$: $[U, \tilde{Q}_a^{\rm tot}] = 0$ $\forall a$. Subscript f's will also distinguish $\mathcal{S}$'s and $\mathcal{E}$'s final states. $\mathcal{E}$'s $j^{\rm th}$ subsystem ends up in $\rho_{\rm f}^{(\mathcal{E},j)} \coloneqq \mathrm{Tr}_{\bar{j}}(\rho_{\rm f}^{(\mathcal{E})})$. Here, and throughout the thesis, we use the notation $\mathrm{Tr}_{\bar{j}}$ to denote tracing over the complement of j. Furthermore, $D(\rho_1 || \rho_2) = -\mathrm{Tr}(\rho_1[\log\rho_1 - \log\rho_2])$ is the quantum relative entropy [37]. The quantum relative entropy is the classical analog of the classical relative entropy, or Kullback–Leibler divergence, and it quantifies the distance between quantum states $\rho_{1,2}$.

Three more quantities change under the charge-conserving unitary U: $\mathcal{S}$'s von Neumann entropy, by $\Delta S_{\rm vN}^{(\mathcal{S})} \coloneqq S_{\rm vN}(\rho_{\rm f}^{(\mathcal{S})}) - S_{\rm vN}(\rho^{(\mathcal{S})})$; the $a^{\rm th}$ charge's environmental expectation value, by $\Delta\langle\tilde{Q}_a^{(\mathcal{E})}\rangle \coloneqq \mathrm{Tr}(\tilde{Q}_a^{(\mathcal{E})}[\rho_{\rm f}^{(\mathcal{E})} - \rho^{(\mathcal{E})}])$; and the system's $a^{\rm th}$ "free energy," by $\Delta F_a^{(\mathcal{S})}$. These changes are related (see Eq. 2.24 of Ref. [36]):

$$D\left(\rho_{\rm f}^{(\mathcal{SE})} \,||\, \rho_{\rm f}^{(\mathcal{S})} \otimes \rho_{\rm f}^{(\mathcal{E})}\right) - \Delta S_{\rm vN}^{(\mathcal{S})} = \beta \sum_a \mu_a \left(\Delta\langle\tilde{Q}_a^{(\mathcal{E})}\rangle - \Delta F_a^{(\mathcal{S})}\right) - D\left(\rho_{\rm f}^{(\mathcal{E})} \,||\, \otimes_j \rho_{\rm f}^{(\mathcal{E},j)}\right). \tag{2.5}$$

The right-hand side of the equation contains a sum of terms that depend on distinct charges. When charges fail to commute, the terms cannot be cleanly attributed to individual charges, and the derivation fails.

An intuition for why this derivation should break down is that noncommuting charges do not necessarily move independently of one another. A simple way to see this is to consider two sites exchanging quanta of spin angular momentum in a spin chain via an interaction H. Say that H conserves the z-component of the spin $\left[H, \sigma_z^{(1)} + \sigma_z^{(1)}\right] = 0$, but

[4] Yunger Halpern's paper was published in 2018 but appeared on the arXiv in 2014.

[5] The quotation marks reflect the controversy surrounding free energies defined information theoretically for out-of-equilibrium states.

transfers the spins locally: $\left[H, \sigma_z^{(1)}\right] \neq 0 \neq \left[H, \sigma_z^{(2)}\right]$. The most general Hamiltonian that satisfies the conservation equation is: $H = c_{zi}\sigma_z^{(1)} + c_{iz}\sigma_z^{(2)} + c_{zz}\sigma_z^{(1)}\sigma_z^{(2)} + c_{xx}(\sigma_x^{(1)}\sigma_x^{(2)} + \sigma_y^{(1)}\sigma_y^{(2)}) + c_{xy}(\sigma_x^{(1)}\sigma_y^{(2)} - \sigma_y^{(1)}\sigma_x^{(2)})$. Any of these coefficients can be zero. However, to also satisfy the transport condition, we need that $c_{xx} \neq \pm i c_{xy}$. Thus, c_{xx} or c_{xy} must be non-zero. Thus, this Hamiltonian necessarily transports the quanta of the other spin components, $\sigma_x^{(j)}$ and $\sigma_y^{(j)}$. Since noncommuting charges do not move independently, it is natural then to expect one can not define free energies for them independently.

Yunger Halpern reasoned about noncommuting charges using thermodynamic resource theories [12]. Resource theories are information-theoretic frameworks used to quantify how effectively an agent can perform a task, subject to some constraints. These constraints are typically placed on the operations performable and on the systems that are accessible [38]. Using a resource theory, one can calculate the optimal efficiency for extracting work from a nonequilibrium quantum system. In thermodynamics, the first law constrains operations to conserve energy. Every unitary U performable on a closed, isolated system conserves the total Hamiltonian: $[U, H^{\text{tot}}] = 0$ [39]. Now suppose that U must also conserve commuting global charges $\tilde{Q}_a^{\text{tot}}$: $[U, \tilde{Q}_a^{\text{tot}}] = 0$ [40]. From which systems can the agent not perform work for free? Systems in the equilibrium state, Eq. (2.2) [40, 41]. However, the proof fails if the charges fail to commute [12]. This is ultimately because the noncommutation of charges does not allow one to use the Backer–Campbell-Hausdorff Formula to equate $\prod_{\alpha=0} \exp\left(-\frac{1}{k_B} F_\alpha Q_\alpha^{\text{tot}}\right) = \exp\left(-\frac{1}{k_B} \sum_{\alpha=0} F_\alpha Q_\alpha^{\text{tot}}\right)$ where F_i are free energies and Q_α^{tot} are charges.

Building on these two results, three separate groups presented physically motivated derivations of the form of the thermal state for systems with noncommuting charges using resource-theory-related argumentss [13, 42, 43, 44]. Ultimately, the form of the NATS was recovered in each work. The trio of papers physically justified ρ_{NATS}'s form in various ways. We highlight one of these below because it will be important in Chapter 4, and it completes the story that Balian and Balazs started.

The authors of reference [13] realized that noncommuting charges prevent microcanonical subspaces from existing (in abundance). The authors therefore generalized microcanonical to approximate microcanonical subspaces. In an approximate microcanonical subspace $\mathcal{M}$, every Q_a^{tot} has a fairly well-defined value: measuring any Q_a^{tot} has a high probability of yielding a value near the expectation value $\langle Q_a^{\text{tot}} \rangle$. In other words, the probability distribution of possible outcomes has one peak with a variance that is small and grows slowly with the system size. The authors defined $\mathcal{M}$ and proved its existence under

certain conditions [13]. Denote by $\Pi_{\mathcal{M}}$ the projector onto $\mathcal{M}$[6]. Consider ascribing the approximate microcanonical state $\Pi_{\mathcal{M}}/\operatorname{Tr}(\Pi_{\mathcal{M}})$ to the global system, formed from N copies of the system $\mathcal{S}$ of interest. Trace out all copies except the ℓ^{th}: $\rho^{(\ell)} = \operatorname{Tr}_{\bar{\ell}}(\Pi_{\mathcal{M}}/\operatorname{Tr}(\Pi_{\mathcal{M}}))$. Compare $\rho^{(\ell)}$ with ρ_{NATS} using the relative entropy. Average over ℓ. This average distance is upper-bounded as

$$\left\langle D\big(\rho^{(\ell)} || \rho_{\text{NATS}}\big) \right\rangle_{\ell} \leq \frac{\theta}{\sqrt{N}} + \theta', \tag{2.6}$$

where θ, θ' depend on various parameters (the number c of charges, their expectation values, etc.) but not N. As the global system grows ($N \to \infty$), the $1/\sqrt{N} \to 0$, so the distance shrinks. Hence a physical argument, based on an ensemble in an approximate microcanonical subspace, complements Jaynes's information-theoretic derivation of ρ_{NATS}. Furthermore, the approximate microcanonical subspace enabled later noncommuting-charge work [3, 45, 46, 47].

2.3 Eigenstate Thermalization Hypothesis

Isolated quantum many-body systems undergo reversible dynamics. How, then, can they come to thermal equilibrium? This question is largely answered by the Eigenstate Thermalization Hypothesis (ETH) [26, 27]. The following section and the results of Chapter 5 hinge on the ETH. In the spirit of efficiently killing birds with stones,[7] we will take a detour to thoroughly introduce the ETH.

To begin, we need to define what is meant by thermalization. Consider a closed quantum system consisting of a lattice with N sites. Each site corresponds to a Hilbert space $\mathcal{H}$ of finite dimensionality d. The system is governed by a Hamiltonian $H = \sum_k E_k |\psi_k\rangle\langle\psi_k|$, where $|\psi_k\rangle$ are energy eigenstates with energies E_k. The time-dependent state $|\Phi(t)\rangle = \sum_k \exp(-iE_k t) c_k |\psi_k\rangle$[8] will have a fixed total energy $E = \langle\Phi(t)|H|\Phi(t)\rangle$, where we set $\hbar = 1$. The expectation value of an observable $\mathcal{O}$ for the state $|\Phi(t)\rangle$ is

$$\langle \mathcal{O}(t) \rangle = \sum_{j,k} e^{-i(E_k - E_j)t} c_j^* c_k \langle \psi_j | \mathcal{O} | \psi_k \rangle . \tag{2.7}$$

[6] To be clear on terminology, if $\mathcal{M}$ was the computational basis $\Pi_{\mathcal{M}} = |0\rangle\langle 0| + |1\rangle\langle 1|$.

[7] "Kill two birds with one stone" is an idiom for successfully achieving two things with one action.

[8] Having a pure initial state is not necessary for the ETH. However, the paradox of unitary dynamics leading to thermalization is most pronounced in pure states; therefore, we consider them.

$\langle \mathcal{O} \rangle_{\text{th}} := \text{tr}[\rho_{\text{th}} O]$ is the thermal expectation value, where ρ_{th} is the thermal state with temperature fixed by the energy of the initial state. We say a system is in thermal equilibrium at time t if $\langle O_i(t) \rangle \approx \langle O_i \rangle_{\text{th}}$ for a set of observable O_i. If the Hamiltonian and local observables satisfy the ETH, the system will thermalize in this sense.

We can also state the approximation $\langle O_i(t) \rangle \approx \langle O_i \rangle_{\text{th}}$ in a different and more precise way. Imagine we begin with an out-of-equilibrium state $|\Phi(0)\rangle$. We expect $\langle \mathcal{O}(t) \rangle$ to (i) initially deviate greatly from $\langle \mathcal{O} \rangle_{\text{th}}$, (ii) approach $\langle \mathcal{O} \rangle_{\text{th}}$ over time, and (iii) fluctuate around $\langle \mathcal{O} \rangle_{\text{th}}$. Thus, if we take the time-average of $\langle \mathcal{O}(t) \rangle$ for a long enough time, we expect it to equal $\langle \mathcal{O} \rangle_{\text{th}}$ up to some correction:

$$\lim_{t \to \infty} \frac{1}{t} \int_0^t dt' \ \langle \mathcal{O}(t') \rangle = \langle \mathcal{O} \rangle_{\text{th}} + O(N^{-1}). \tag{2.8}$$

Throughout this subsection, big-O notation means "scales as."

Myriad numerical and experimental observations support the ETH, which has been applied across many-body physics. Despite the apparent tension between unitary dynamics and thermalization, most quantum many-body systems thermalize [48]. However, not all combinations of Hamiltonians, states, and observables obey the ETH, nor should we expect them to, based on classical thermodynamics. Below, we explain more precisely when the ETH holds and what its physically motivated assumptions are.

What are the conditions for the ETH? The first two conditions restrict the initial state so that it is possible to define a notion of temperature. The first condition is that the energy scales with the system size,

$$E = \ \langle \Phi(t) | H | \Phi(t) \rangle \sim N. \tag{2.9}$$

This ensures we have a finite amount of energy per degree of freedom, which is necessary for defining a finite temperature. Second, the energy uncertainty is small,

$$\Delta E = \sqrt{\langle H^2 \rangle - \langle H \rangle^2} \sim N^{\gamma} \tag{2.10}$$

where $\gamma < 1$. Expand your initial state in energy eigenstates; this condition restricts the range of energies one is superposing to be small compared to the total energy. This is also necessary for defining a temperature. If your initial state is, for example, a superposition of two states with extremely different energies, then it is unclear how to define the temperature because if the energy is not well defined, the temperature is not well defined. These first two conditions place restrictions on the states $|\Phi(0)\rangle$, but most physically realistic states satisfy these first two conditions. States that do not satisfy these conditions exist; however,

we do not expect those states to adhere to classical statistical mechanics, which is what the ETH is trying to derive.

The ETH is largely an ansatz for the forms of matrix elements. We can break Eq. (2.7) into two terms,

$$\langle \mathcal{O}(t) \rangle = \sum_k \left(|c_k|^2 \langle \psi_k | \mathcal{O} | \psi_k \rangle \right) + \sum_{j \neq k} \left(e^{-i(E_k - E_j)t} c_j^* c_k \langle \psi_j | \mathcal{O} | \psi_k \rangle \right). \tag{2.11}$$

The first term is time-independent, thus we expect it to correspond to the time-independent average value around which $\langle \mathcal{O}(t) \rangle$ fluctuates, denoted by $\langle \mathcal{O} \rangle_{\text{th}}$. We then expect the second term to correspond to the fluctuations. However, the first term in Eq. (2.11) contains detailed information about the initial state, specifically the sum of $|c_k|^2$. In contrast, $\langle \mathcal{O} \rangle_{\text{th}}$ contains very little information about the initial state, only its energy.

To resolve this discrepancy, we add a third assumption—if we plotted $\langle \psi_k | \mathcal{O} | \psi_k \rangle$ against the E_k in ascending order, the function would vary smoothly. We can then plot $|c_k|^2$ against the same E_k. This second plot will not vary smoothly. However, since ΔE is small, the non-negligible values of $|c_k|^2$ should be concentrated in a small energy window. Since $\langle \psi_k | \mathcal{O} | \psi_k \rangle$ varies smoothly, the exact values of $|c_k|^2$ become less significant, and multiplying them with the eigenvalues of some operator will yield approximately the same value. Thus, our second and third assumptions explain why the first term depends only on the energy and not the specific $|c_k|^2$.

We now turn to the second term, which needs to account for the fluctuations. We need these fluctuations to be small. To ensure this, we add a fourth assumption—the Hamiltonian is nondegenerate and that $\langle \psi_j | \mathcal{O} | \psi_k \rangle$ are exponentially small in N. Note that it is still possible to have specific times when the second term is large due to the majority of the small terms interfering constructively. In fact, we know this is possible because non-equilibrium needs to be possible, for example, at $t = 0$. However, most times, this is not true. Finally, the degeneracy condition is not strictly necessary but is for mathematical convenience. Assumptions three and four place restrictions on the observables. There exist many observables which satisfy these conditions.

2.4 New physics

We are finally ready to introduce the new physics related to noncommuting thermodynamic charges that were not discovered by the research presented in this thesis. We organize the results indicating that noncommuting charges obstruct thermalization in the

first subsection (Section 2.4.1) and the remaining results in the second subsection (Section 2.4.2).

2.4.1 Why noncommuting charges may inhibit thermalization

Earlier works in the field proposed that noncommuting charges may inhibit thermalization, offering two justifications. One justification is that charges impede physical derivations of the thermal state's form [12, 13]. Another is that noncommuting charges force degeneracies on $H^{\rm tot}$ according to Schur's lemma, a group-theoretic result (App. A.1 and [49, 50, 45]). Nondegenerate Hamiltonians underlie foundational assumptions of thermalization, mixing, and equilibration present in conventional theories (refer to [27, 26, 51, 52]), which noncommuting charges challenge. The following results give three further reasons.

Decreased thermodynamic-entropy production

Noncommuting charges reduce entropy production, which quantifies irreversibility [14]. Throughout this subsection, by entropy, we mean, thermodynamic entropy, not entanglement entropy. Moreover, reference [14] studies the entropy production per collision in a collisional model where each collision is governed by unitary U. The collision model consists of two systems each composed of many subsystems. One subsystem from each system is drawn at random, the two subsystems "collide" by evolving under U, and are then returned to their respective systems. With collisions as a proxy for time, we can think of the entropy production per collision as the entropy-production rate.

Consider systems $X = A, B$ with charges $Q_a^{(X)}$ that might or might not commute. Each system begins in a generalized Gibbs ensemble $\rho_{\vec{\mu}^{(X)}}^{(X)} \propto \exp\left(-\sum_a \mu_a^{(X)} Q_a^{(X)}\right)$, wherein $\vec{\mu}^{(X)} = (\mu_0^{(X)}, \mu_1^{(X)}, ...)$ [53] (Fig. 2.1). Hence AB begins in $\rho(0) \coloneqq \rho_{\vec{\mu}^{(A)}}^{(A)} \otimes \rho_{\vec{\mu}^{(B)}}^{(B)}$. Let us specialize to the linear-response regime, where small external perturbations lead to proportional changes in the system's behavior. For example, when a small force is applied to a spring, the spring stretches by an amount proportional to the force (Hooke's Law). If the force is doubled, the displacement doubles. To stay in this regime we restrict the differences in chemical potential between the systems to be small: $\vec{\mu}^{(A)} \approx \vec{\mu}^{(B)}$. A charge-conserving unitary U can shuttle charges between the systems, producing entropy. Denote by $\delta\mu_a \coloneqq \mu_a^{(A)} - \mu_a^{(B)}$ the difference between the systems' a-type chemical potentials. System A's a-type charge changes, in the Heisenberg picture, by $U^\dagger Q_a^{(A)} U - Q_a^{(A)}$. We

combine the foregoing two quantities into

$$\tilde{\Sigma} \coloneqq \sum_a \delta\mu_a \big(U^\dagger Q_a^{(A)} U - Q_a^{(A)} \big). \tag{2.12}$$

Taking the expectation value of $\tilde{\Sigma}$ in the initial state, we obtain the net entropy production, $\Sigma = \mathrm{Tr}\big(\tilde{\Sigma}\, \rho(0)\big)$.

According to the linear-response assumption[9], the initial state lies near the fixed point. This will be a tensor product of Gibbs ensembles for each subsystem: $\pi \coloneqq \rho^{(A)}_{\vec{\mu}^{(A)}} \otimes \rho^{(B)}_{\vec{\mu}^{(A)}}$ of U. π and $\tilde{\Sigma}$ have a Wigner–Yanase–Dyson skew information

$$I_y(\pi, \tilde{\Sigma}) \coloneqq -\frac{1}{2} \mathrm{Tr}\left([\pi^y, \tilde{\Sigma}] [\pi^{1-y}, \tilde{\Sigma}] \right), \tag{2.13}$$

whose parameter $y \in (0, 1)$. $I_y(\pi, \tilde{\Sigma})$ quantifies the coherence that $\tilde{\Sigma}$ has relative to π's eigenbasis. Said differently, $I_y(\pi, \tilde{\Sigma})$ quantifies the amount of information that is lost due to the non-commutativity of an observable and a state. Thus, it is natural to expect that the Wigner–Yanase–Dyson skew information contributes to the entropy production. The exact expression was found in Ref. [14]:

$$\Sigma = \frac{1}{2}\, \delta\Big(\tilde{\Sigma}\Big) - \frac{1}{2} \int_0^1 \mathrm{d}y\, I_y(\pi, \tilde{\Sigma}) \tag{2.14}$$

I_y is always ≥ 0 and is positive if and only if the charges fail to commute. Therefore, noncommuting charges lower Σ. Noncommuting charges decrease the entropy production [14]. Since entropy production accompanies thermalization, noncommutation may inhibit thermalization.

Two extensions support [14]. First, Shahidani numerically simulated an optomechanical system interacting with a squeezed thermal bath [54]. Second, Upadhyaya *et al.* progressed beyond the linear-response regime [55]. Even there, charges' noncommutation decreases entropy production.

Constraints on charge-conserving dynamics

A key result in quantum computing is that every N-qubit unitary decomposes into gates on pairs of qubits [56, 57, 58]. This decomposition can further reduce to gates acting

[9] In π, unlike in $\rho(0)$, A and B have the same lists of chemical potentials.

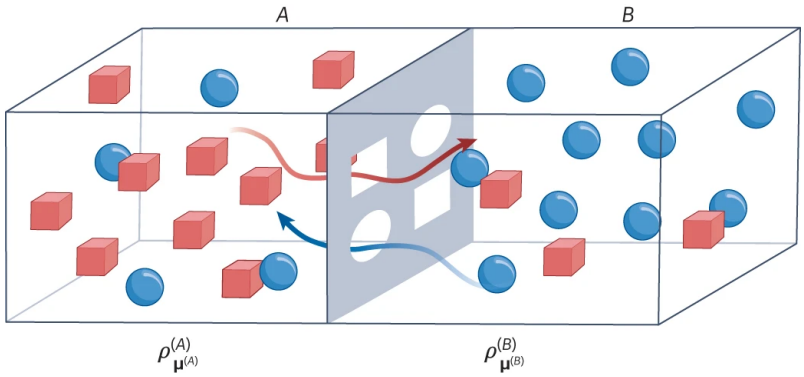

Figure 2.1: **Two thermal reservoirs exchange charges, producing entropy:** Blue spheres represent charges of one type, and red cubes represent charges of another.

on spatially local qubits. Can charge-conserving local unitaries implement every charge-conserving global unitary? Marvian proved that they cannot [59]. Locality-constrained charge-conserving unitaries fail to even approximate the global unitaries U. The reason is that the two types of unitaries form Lie groups of different dimensions [59, 60, 61, 62]. Marvian also highlighted that noncommuting charges uniquely impose more stringent restrictions on the global unitaries U. Specifically, noncommuting charges impose four types of constraints on the implementable global unitaries, in contrast to only two types from commuting charges [62]. These additional constraints might limit chaos, which often facilitates thermalization. Therefore, Marvian's results suggest that noncommuting charges could inhibit thermalization.

Conflicting with the ETH

Noncommuting charges cause the ETH to conflict with the Wigner–Eckart theorem [63], violating the ETH. Reference [47] therefore posited a non-Abelian ETH, which shows that noncommuting charges can lead to larger corrections to the ETH.

We briefly review the Wigner–Eckart theorem. Consider N qubits whose global spin components $S^{\text{tot}}_{x,y,z}$ are conserved, as in Section 1.2. Denote by $\{|\alpha, m\rangle\}$ the eigenbasis shared by H^{tot}, $(\vec{S}^{\text{tot}})^2$, and S^{tot}_z: if $\hbar = 1$, then $H^{\text{tot}}|\alpha, m\rangle = E_\alpha|\alpha, m\rangle$, $(\vec{S}^{\text{tot}})^2|\alpha, m\rangle = s_\alpha(s_\alpha+1)|\alpha, m\rangle$, and $S^{\text{tot}}_z|\alpha, m\rangle = m|\alpha, m\rangle$. The Wigner–Eckart theorem governs spherical tensor operators formed from components $T^{(k)}_q$ [63]. The $T^{(k)}_q$'s form a basis for the space of operators defined on the system's Hilbert space. For example, consider an atom absorbing a photon (of spin $k = 1$), gaining $q = 1$ quantum of z-type angular momentum. $T^{(k=1)}_{q=1}$

represents the photon's effect on the atom's state. Consider representing $T_q^{(k)}$ as a matrix relative to the energy eigenbasis. That matrix obeys the Wigner–Eckart theorem [63]:

$$\langle \alpha, m | T_q^{(k)} | \alpha', m' \rangle = \langle s_\alpha, m | s_{\alpha'}, m'; k, q \rangle \langle \alpha || T^{(k)} || \alpha' \rangle . \tag{2.15}$$

$\langle s_\alpha, m | s_{\alpha'}, m'; k, q \rangle$ denotes a Clebsch-Gordan coefficient, a conversion factor between the product state $|s_{\alpha'}, m'; k, q\rangle \equiv |s_{\alpha'}, m'\rangle \, |k, q\rangle$ and the total-spin eigenstate $|s_\alpha, m\rangle$. $\langle \alpha || T^{(k)} || \alpha' \rangle$ is a reduced matrix element—the part of $\langle \alpha, m | T_q^{(k)} | \alpha', m' \rangle$ that does not depend on magnetic spin quantum numbers. Clebsch–Gordan coefficients are used for adding a couple of spins, while the ETH is about many-body systems. However, the pairwise addition can be repeated iteratively. First, add two spins using the Clebsch-Gordan coefficients to find the possible resultant spin states and their corresponding coefficients. Next, take each resultant spin from this initial pairwise addition and add it to the next spin in the sequence. Continue this process iteratively, each time using all resultant spins from the previous step, until all spins have been added.

Continue Iteratively: Continue this process iteratively until all spins have been added. Each step involves adding the resultant spin from the previous step to the next spin in the sequence.

We can now see the source of conflict. Consider the term on the left-hand side of Eq. (2.15). The Wigner–Eckart theorem states this term should equal the right-hand side of Eq. (2.15). However, ETH states this term should equal something else, the right side of Eq. (2.11). The ETH states that off-diagonal elements $\langle \alpha, m | T_q^{(k)} | \alpha', m' \rangle$ must be exponentially small in N. The Wigner–Eckart theorem implies that these elements may be $O(1)$.

Reference [47] therefore posited a non-Abelian ETH. This ansatz depends on the average energy $\mathscr{E} := \frac{1}{2}(E_\alpha + E_{\alpha'})$, energy difference $\omega := E_\alpha - E_{\alpha'}$, average spin quantum number $\mathscr{S} := \frac{1}{2}(s_\alpha + s_{\alpha'})$, and difference $\nu := s_\alpha - s_{\alpha'}$. Denote by $S_{\rm th}(\mathscr{E}, \mathscr{S})$ the thermodynamic entropy at energy $\mathscr{E}$ and spin $\mathscr{S}$. The observable $T_q^{(k)}$ and Hamiltonian $H^{\rm tot}$ satisfy the non-Abelian ETH if, for smooth real functions $\mathcal{T}^{(k)}(\mathscr{E}, \mathscr{S})$ and $f_\nu^{(k)}(\mathscr{E}, \mathscr{S}, \omega)$,

$$\langle \alpha || T^{(k)} || \alpha' \rangle = \mathcal{T}^{(k)}(\mathscr{E}, \mathscr{S}) \, \delta_{\alpha,\alpha'} + e^{-S_{\rm th}(\mathscr{E},\mathscr{S})/2} \, f_\nu^{(k)}(\mathscr{E}, \mathscr{S}, \omega) \, R_{\alpha,\alpha'} . \tag{2.16}$$

$R_{\alpha,\alpha'}$ is an erratically varying number. The matrix element (2.15) deviates from the ordinary ETH through $\mathscr{S}$-dependent functions and a Clebsch–Gordan coefficient. Equation (2.16) has withstood numerical checks with a Heisenberg Hamiltonian on a two-dimensional qubit lattice [64].

The non-Abelian ETH predicts thermalization to the usual extent in some, but not all, contexts. Consider preparing the system in a state $|\psi(0)\rangle$ in an approximate microcanonical subspace (Section 2.2). Suppose that $|\psi(0)\rangle$ has an extensive magnetization along an axis that we call $\hat{z}$: $\langle\psi(0)|S_z^{\rm tot}|\psi(0)\rangle = O(N)$. According to the non-Abelian ETH,

$$\lim_{t\to\infty} \frac{1}{t} \int_0^t dt' \, \langle\psi(t')|T_q^{(k)}|\psi(t')\rangle = {\rm Tr}\left(T_q^{(k)}\rho_{\rm NATS}\right) + O\left(N^{-1}\right). \tag{2.17}$$

However, if $\langle\psi(0)|S_z^{\rm tot}|\psi(0)\rangle = 0$, the correction can become $O(N^{-1/2})$—polynomially larger. This result relies on an assumption argued to be physically reasonable: the smooth function $\mathcal{T}^{(k)}$ in (2.16), akin to a microcanonical average, can contain a nonzero term of $O(s_\alpha/N)$. The unusually large correction constitutes further evidence that charges' noncommutation can alter thermalization.

2.4.2 Other new physics

The effects of noncommuting charges have not been limited to topics related to thermalization. In this subsection, we complete our discussion on the new physics engendered by noncommuting charges.

More stationary states

Consider an open quantum system with a Liouvilian superoperator $\mathscr{L}$. $\rho_{\rm stat}$ is a stationary state of $\mathscr{L}$ if $\mathscr{L}\rho_{\rm stat} = 0$. One might associate a system's $j^{\rm th}$ stationary state, $\rho_{\rm stat}^{(j)}$, with a classical alphabet's $j^{\rm th}$ letter, L_j: $\rho_{\rm stat}^{(j)} \leftrightarrow L_j$.To encode L_j in the system, one would prepare any state that thermalizes to $\rho_{\rm stat}^{(j)}$.The more stationary states the system has, the more classical information the system may store. Denote by $n_{\rm stat}$ the number of stationary states. Zhang et al. derive a lower bound $n_{\rm NC}$ on $n_{\rm stat}$ for a system with noncommuting charges [65]: $n_{\rm NC} = \sum_j \mathcal{D}_j^2$, wherein $\mathcal{D}_j$ denotes the symmetry group's $j^{\rm th}$ irreducible representation's dimension. For example, $n_{\rm NC} \sim N^3$ for the Heisenberg model (Section 1.2) coupled to an environment that conserves the system-of-interest charges $\sigma_{x,y,z}^{(\mathcal{S})}$. If the charges commute, the lower bound $n_{\rm C}$ scales as the number of simultaneous eigenspaces shared by all the $Q_a^{(\mathcal{S})}$'s. Since $n_{\rm NC}$ and $n_{\rm C}$ scale differently, noncommuting charges could alter the number of stationary states and so the amount of information storable.

Hybrid energy-level statistics

Energy-level statistics diagnose quantum chaos and integrability [66]. Denote by $\omega = E_{j+1} - E_j$ the spacing between consecutive eigenenergies of a many-body Hamiltonian. Any given spacing (near the spectrum's center) has a probability density $P(\omega)$ of being of size ω. A Poissonian[10] $P(\omega)$ diagnoses integrability [66, Section 2.3]; and a Wigner–Dyson distribution, $A_\beta \omega^\beta \exp(-B_\beta \omega^2)$, chaos. The parameter $\beta \in \{1, 2, 4\}$ depends on the Hamiltonian's time-reversal and rotational symmetries. Normalization and the mean ω determine the coefficients A_β and B_β. Noncommuting charges break the Poisson-vs.-Wigner–Dyson dichotomy as commuting charges cannot: the charges generate a non-Abelian algebra, which has multidimensional irreducible representations. They induce statistics that interpolate between the two distributions [67, 64, 68]. Noh observed such statistics numerically using a 2D Heisenberg model [64].

Many-body localization

Many-body localization (MBL) is an effect that may occur in disordered interacting quantum systems. For example, consider a qubit chain subject to the disordered Heisenberg Hamiltonian $H^{\text{tot}}_{\text{MBL}} = \sum_{j=1}^{N} \left(J\vec{\sigma}^{(j)} \cdot \vec{\sigma}^{(j+1)} + h_j \sigma_z^{(j)} \right)$. The disorder term, $\sum_{j=1}^{N} h_j \sigma_z^{(j)}$, acts as an external field whose magnitude h_j varies randomly across sites. If the disorder is much stronger than the interaction, $h_j \gg J$, the system localizes. Imagine measuring each qubit's σ_z. The qubits approximately maintain the measured configuration long afterward. This behaviour contrasts with how thermalizing systems, such as classical gases, change configurations quickly. Hence MBL resists thermalization for long times. The reason is, the Hamiltonian decomposes as a linear combination of quasilocal degrees of freedom [69].

My examining committee asked me to comment on the controversy surrounding MBL, which I have added here. The theoretical existence of MBL in one-dimensional systems is mostly accepted, and its existence in higher dimensions is highly unlikely. Furthermore, it is clear that for any finite system and in any dimension, some regime exhibits MBL [70]. The controversy surrounding MBL concerns its late-time thermodynamic limit behaviour. There is debate over MBL being a distinct phase with its unique class, the precise conditions for MBL, and experimental evidence of MBL [71, 72].

Noncommuting charges seem to destabilize MBL [73]. Consider forcing a non-Abelian symmetry on $H^{\text{tot}}_{\text{MBL}}$. The resulting Hamiltonian, $H^{\text{tot}}_{\text{MBL}'}$, will have degeneracies, by Schur's

[10] This $P(\omega)$ is the Poisson distribution whose average-rate-of-occurrence parameter vanishes. The reason is, $P(\omega)\, d\omega$ equals the probability that zero eigenenergies lie in a width-$d\omega$ interval.

lemma (App. A.1). So will the quasilocal degrees of freedom, which can therefore become "excited" at no energy cost. Consider adding to $H^{\text{tot}}_{\text{MBL}'}$ an infinitesimal field that violates the symmetry. The resulting Hamiltonian, $H^{\text{tot}}_{\text{MBL}''}$, can map $H^{\text{tot}}_{\text{MBL}'}$ eigenstates $|\psi\rangle$ to same-energy eigenstates $|\tilde{\psi}\rangle$: $\langle\tilde{\psi}|H^{\text{tot}}_{\text{MBL}''}|\psi\rangle \neq 0$. Two such eigenstates can be zero-energy "excited" states of neighbouring quasilocal degrees of freedom. Hence $H^{\text{tot}}_{\text{MBL}''}$ can transport zero-energy "excitations" between quasilocal degrees of freedom—across the system. Such transport is inconsistent with MBL. In summary, non-Abelian symmetries force degeneracies in the spectrum, leading to instability once you allow for perturbations. This is the first result reviewed in this thesis that contradicts the earlier expectations that noncommuting charges hinder thermalization.

Chapter 3

Bridging to experiments and many-body physics

This chapter is based on reference [2] and overlaps with its text.

3.1 Introduction

In quantum information theory, "an abstract view of dynamics, minimal in the details of Hamiltonians, is often employed"[74], and so in quantum-information-theoretic thermodynamics. This approach has also been prevalent in the study of noncommuting charges. However, the realm of experiments and many-body theory necessitates detailed microscopic Hamiltonians. It is essential to construct Hamiltonians that facilitate the local transport of noncommuting charges while ensuring their global conservation to connect the result of noncommuting charges with practical experiments and many-body physics. Achieving this integration will allow using many-body tools to study the dynamic of noncommuting charge physics. Furthermore, the literature on noncommuting-charge physics is filled with results that merit experimental testing.

Before the work presented in this chapter, it was unknown (i) whether Hamiltonians that transport noncommuting observables locally, while conserving them globally, exist; (ii) how such Hamiltonians look, if they exist; (iii) how to construct such Hamiltonians for given noncommuting charges; and (iv) for which charges such Hamiltonians can be constructed. We answer these questions, enabling noncommuting charges to progress from

its quantum-information-theoretic-thermodynamic birthplace to experiments and many-body physics.

This chapter introduces a procedure for constructing Hamiltonians that overtly move noncommuting charges between subsystems while conserving the charges globally. The Hamiltonians can couple arbitrarily many subsystems together and can be integrable or nonintegrable. The procedure is general, being independent of any physical platforms. Consequently, the Hamiltonians can be realized with diverse physical systems, such as superconducting circuits, neutral atoms, and trapped ions.

The rest of the chapter is organized as follows. We detail our setup and review the mathematical background in Section 3.2. Section 3.3 presents our procedure. We first synthesize the procedure, crystallize the main result, and present two properties of the procedure. We then illustrate the procedure using an example familiar in quantum information, the Lie algebra $\mathfrak{su}(2)$. A richer example provides intuition in Section 3.4: Hamiltonians that transport and conserve charges in the Lie algebra $\mathfrak{su}(3)$. Section 3.5 concludes with a summary of our results.

3.2 Preliminaries

We begin by outlining our setup and then review the mathematical foundation pertinent to our study, focusing on the basics of Lie algebra theory. In Chapter 5, we revisit Lie algebras. To prevent redundancy, we include a few additional details in this section that will be relevant later.

3.2.1 Setup

Consider a closed quantum system consisting of a lattice with N sites. Each site corresponds to a Hilbert space $\mathcal{H}$ of finite dimensionality d. The system is governed by a global Hamiltonian H^{tot}. Let Q_α denote a Hermitian operator defined on $\mathcal{H}$. We denote by $Q_\alpha^{(j)}$ the observable defined on the j^{th} subsystem's $\mathcal{H}$. We denote an extensive observable

$$Q_\alpha^{\text{tot}} := \sum_{j=1}^{N} \tilde{Q}_\alpha^{(j)} \equiv \sum_{j=1}^{N} \mathbb{1}^{\otimes(j-1)} \otimes \tilde{Q}_\alpha^{(j)} \otimes \mathbb{1}^{\otimes(N-j)}. \tag{3.1}$$

We will construct H^{tot} that conserve noncommuting charges globally, $[H^{\text{tot}}, Q_\alpha^{\text{tot}}] = 0$, while transporting them locally, $\left[H^{\text{tot}}, Q_\alpha^{(j)}\right] \neq 0$ for some site j.

3.2.2 Lie Algebra background

Charges Q_α that generate Lie algebras are important in physics because they describe many conserved physical quantities, including angular momentum, particle number, electric charge, color charge, and weak isospin [1, 11, 75, 76], i.e., everything in the Standard Model of particle physics. The Lie algebras relevant to studying noncommuting charges are finite-dimensional because we study systems with a finite number of linearly independent charges [2]. The algebras are defined over the complex number because the operators are Hermitian. Finally, the algebras are semisimple so that the operator representation of the charges can be diagonalized (not necessarily simultaneously diagonalized) [77]. From this point onward, we denote by $\mathfrak{g}$ a finite-dimensional semisimple complex Lie algebra.

An algebra's dimension c equals the number of generators in a basis for the algebra. The algebra's rank r is the dimension of the algebra's maximal commuting subalgebra, the largest subalgebra in which all elements are commuting. For example, consider the usual basis for $\mathfrak{su}(2)$—the Pauli-operators. There are three generators in this basis, so $c = 3$, and none of these operators commute with one another, so $r = 1$. A Cartan subalgebra is a maximal Abelian subalgebra consisting of semisimple elements, $h \in \mathfrak{h}$. Every $\mathfrak{g}$ will have a $\mathfrak{h}$.

The $\mathfrak{g}$ definition includes a vector space V defined over a field F. A form is a map $V \times V \to F$. A representation of $\mathcal{A}$ is a Lie-bracket-preserving map from $\mathcal{A}$ to a set of linear transformations. The Killing form of operators $x, y \in \mathfrak{g}$ is the bilinear form

$$(x, y) := \mathrm{tr}(\mathrm{ad}x \cdot \mathrm{ad}y) \tag{3.2}$$

where ad$x$ is the image of x under the adjoint representation of $\mathfrak{g}$.

We have justified studying algebras that are finite-dimensional, semisimple, and over the complex numbers. We also assume that on $\mathcal{A}$ is defined a Killing form that induces a metric. Many physically significant algebras satisfy all of these assumptions—for example, $\mathfrak{su}(N)$, $\mathfrak{so}(N)$, and all other simple Lie algebras (see Appdenix B.1 and [11, 75, 76]). Table 1 lists the simple Lie algebras. Every Cartesian product of simple Lie algebras yields a semisimple Lie algebra $\mathcal{A}$. Such an algebra generates a semisimple Lie group $\mathcal{G}$. For example, if $\mathcal{A}$ consists of angular momentum, $\mathcal{A} = \mathfrak{su}(D)$, the corresponding $\mathcal{G}$ consists of rotations: $\mathcal{G} = \mathrm{SU}(D)$. To clarify, the script notation refers to the algebra, e.g. $\mathfrak{su}(D)$, and the non-script notation to the corresponding group, SU(D).

Essential to our study are Cartan–Weyl bases [77]. Such a basis consists of r elements forming a Cartan subalgebra and $c - r$ root vectors. We introduced the Cartan subalgebra

Algebra	Dimension (c)	Rank (r)	c/r
$\mathfrak{so}(2D)$	$D(2D-1)$	D	$2D-1$
$\mathfrak{sl}(D+1)$	$(D+1)^2-1$	D	$D+2$
$\mathfrak{so}(2D+1)$	$D(2D+1)$	D	$2D+1$
$\mathfrak{sp}(2D)$	$D(2D+1)$	D	$2D+1$
$\mathfrak{g}_2$	14	2	7
$\mathfrak{f}_4$	52	4	13
$\mathfrak{e}_6$	78	6	13
$\mathfrak{e}_7$	133	7	19
$\mathfrak{e}_8$	248	8	31

Table 3.1: **Simple Lie algebras:** c denotes an algebra's dimension, and r denotes the rank. We implicitly omit $\mathfrak{so}(2)$ and $\mathfrak{so}(4)$, which are not simple [11]. Also, $\mathfrak{su}(D)$ is a simple Lie algebra. However, including $\mathfrak{su}(D)$ would be redundant: the complexification of $\mathfrak{su}(D)$ is isomorphic to $\mathfrak{sl}(D)$.

above and will introduce the root vectors here. Let $\beta(h) \coloneqq (h'_\beta, h)$ where $h, h'_\beta \in \mathfrak{h}$. $\beta(h)$ is a root of $\mathfrak{g}$ relative to $\mathfrak{h}$ if there exists a non-zero operator $L_\beta \in \mathfrak{g}$ such that

$$[h, L_\beta] = \beta(h) L_\beta. \tag{3.3}$$

These operators L_β are the root vectors. Denote by Δ all roots of $\mathfrak{g}$ with respect to $\mathfrak{h}$. If $\beta \in \Delta$, then so is $-\beta$. Thus, root vectors always come in pairs $L_{\pm\beta}$. In practice, root vectors often have the form of ladder operators. Each β corresponds to two ladder operators, one raising ($+\beta$) and one lowering ($-\beta$). Hence β runs from 1 to $\frac{c-r}{2}$. Each $L_{\pm\beta}$ raises or lowers at least one Q_α. Every finite-dimensional semisimple complex Lie algebra $\mathcal{A}$ has a Cartan-Weyl basis. In fact, $\mathcal{A}$ has infinitely many. The choice of Cartan-Weyl is not unique.

3.3 Procedure

We first synopsize our procedure before offering a guided walkthrough to facilitate a more comprehensible presentation.

Below, we will refer to a preferred basis of charges. It is preferable for two reasons. First, the basis endows the Hamiltonian with a simple physical interpretation: the two-

body interaction we construct transports all these charges locally while conserving them globally. Second, the basis is (Killing-)orthogonal.

3.3.1 Synposis

We construct, as follows, Hamiltonians that transport noncommuting charges locally and conserve the charges globally:

1. Identify an arbitrary Cartan-Weyl basis for the algebra, $\mathcal{A}$.

2. The Cartan-Weyl basis contains r Hermitian operators that commute with each other. Scale each such operator such that it has a unit Hilbert-Schmidt norm [Eq. (3.5)]. Label the results $Q_{\alpha=1,2,\ldots,r}$. Include them in the preferred basis for the algebra.

3. The other Cartan-Weyl-basis elements are ladder operators that form raising-and-lowering pairs: $L_{\pm\beta}$, for $\beta = 1, 2, \ldots c - r$. From each pair, form one term in the two-body interaction, $H^{(j,j')}$ [Eq. (3.6)].

4. Write out the form of the most general element $U \in \mathcal{G}$ of the Lie group $\mathcal{G}$ generated by $\mathcal{A}$. Conjugate each charge Q_α and each ladder operator $L_{\pm\beta}$ with U [Eq. (3.7)]. The new charges and new ladder operators, together, form another Cartan-Weyl basis.

5. Constrain U such that every new charge Q_α is Killing-orthogonal to (i) each other new charge and (ii) each charge already in the basis [Eq. (3.9)].

6. Include each new Q_α in the basis for $\mathcal{A}$.

7. From each new pair $L_{\pm\beta}$ of ladder operators, form a term in the two-body interaction $H^{(j,j')}$ [Eq. (3.10)].

8. Repeat steps 4-7 until having identified c/r Cartan-Weyl bases, wherein c denotes the algebra's dimension. Each Cartan-Weyl basis contributes r elements Q_α to the preferred basis for $\mathcal{A}$. The basis is complete, containing $r \cdot \frac{c}{r} = c$ elements.

9. Constrain the two-body interaction to conserve each global charge [Eq. (3.14)], for all $\alpha = 1, 2, \ldots, c$. Solve for the hopping frequencies $J_\beta^{(j,j')}$ that satisfy this constraint.

10. If a k-body interaction is desired, for any $k > 2$: Perform the following substeps for $\ell = 3, 4, \ldots, k$: Multiply together ℓ unconstrained two-body interactions (3.12) cyclically:

$$H^{\left(j,j',\ldots,j^{(\ell)}\right)} = H^{(j,j')} H^{(j',j'')} \ldots H^{\left(j^{(\ell-1)},j^{(\ell)}\right)} H^{(j^{(\ell)},j)}. \tag{3.4}$$

Constrain the couplings so that $[H^{\left(j,j',\ldots,j^{(\ell)}\right)}, Q_\alpha^{\text{tot}}] = 0$ for all α. If $H^{\left(j,j',\ldots,j^{(\ell)}\right)}$ contains fewer-body terms that conserve all the Q_α^{tot}, subtract those terms off.

11. Sum the accumulated interactions $H^{\left(j,j',\ldots,j^{(k)}\right)}$ over the subsystems $j, j', \ldots$ to form H^{tot}.

12. If H^{tot} is to be nonintegrable, add longer-range interactions and/or large-k k-body interactions until breaking integrability, as signalled by, e.g., energy-gap statistics[1].

Having synopsized our procedure, we present two properties of it. The first property ensures that the procedure runs for an integer number of iterations (step 8).

Proposition 1. *Consider any finite-dimensional semisimple complex Lie algebra. The algebra's dimension, c, and rank, r, form an integer ratio: $c/r \in \mathbb{Z}_{>0}$.*

We prove this proposition in Appendix B.4. It seems possible that this Proposition has been proved before. However, we could not find such a deviation, so we provided one.

Theorem 1. *The charges $Q_1, Q_2, \ldots, Q_c$ produced by the procedure form a basis for the algebra $\mathcal{A}$.*

Proof. The charges are Killing-orthogonal by construction: $(Q_\alpha, Q_\beta) = 0$ for all α, β. The Killing form induces a metric on $\mathcal{A}$ by assumption. Therefore, the Q_α are linearly independent according to this metric.

The procedure produces c charges (step 8). c denotes the algebra's dimension, the number of elements in each basis for $\mathcal{A}$. Hence every linearly independent set of c $\mathcal{A}$ elements forms a basis for $\mathcal{A}$. Hence, the Q_α form a basis. □

[1] This is saying that if you want the system to be nonintegrable, you can keep adding interactions until it is

3.3.2 Pedagogical explanation using $\mathfrak{su}(2)$

The procedure's starting point is an algebra. We first identify an arbitrary Cartan–Weyl basis for the algebra. For this example we choose σ_z and $\sigma_{\pm z} = \frac{1}{2}(\sigma_x \pm i\sigma_y)$. We assign the Hermitian operators to our basis of charges, $Q_1 = \sigma_z$. If $r > 1$, we rescale these operators to endow them with unit Hilbert-Schmidt norms,

$$\mathrm{Tr}\big(Q_\alpha^\dagger Q_\alpha\big) = 1, \tag{3.5}$$

before including them in our preferred basis. In the $\mathfrak{su}(2)$ example, the ladder operators raise and lower σ_z: $L_{\pm z}\,|{\mp z}\rangle = |{\pm z}\rangle$. In other algebras, an $L_{\pm\beta}$ can raise and/or lower multiple Q_α's. Examples include $\mathfrak{su}(3)$ (Section 3.4).

From each ladder-operator pair, we construct an interaction that couples subsystems j and j'. Let $J_\beta^{(j,j')}$ denote a hopping frequency. An interaction that transports all the charges between j and j', while conserving each charge globally, has the form

$$H^{(j,j')} \propto \sum_{\beta=1}^{(c-r)/2} J_\beta^{(j,j')} \left(L_{+\beta}^{(j)} L_{-\beta}^{(j')} + L_{-\beta}^{(j)} L_{+\beta}^{(j')} \right). \tag{3.6}$$

We assemble the other terms in $H^{(j,j')}$ from other Cartan-Weyl bases, constructed as follows. Let U denote a general element of the group $\mathcal{G}$. We conjugate, with U, each element of our first Cartan-Weyl basis: for $\alpha = 1, 2, \ldots, r$ and $\beta = 1, 2, \ldots, \frac{c-r}{2}$,

$$Q_\alpha \mapsto U^\dagger Q_\alpha U = Q_{\alpha+r}, \quad \text{and} \tag{3.7}$$

$$L_{\pm\beta} \mapsto U^\dagger L_{\pm\beta} U = L_{\pm\left(\beta + \frac{c-r}{2}\right)}. \tag{3.8}$$

We include the new Q_α's (for which $\alpha = r+1, r+2, \ldots, 2r$) in our preferred basis for the algebra.

We constrain U such that each new Q_α is Killing-orthogonal to (i) each other new charge Q_β and (ii) each original charge Q_γ:

$$(Q_\alpha, Q_\beta) = (Q_\alpha, Q_\gamma) = 0 \tag{3.9}$$

for all $\alpha, \beta = r+1, r+2, \ldots, 2r$ and all $\gamma = 1, 2, \ldots, r$. For $\mathfrak{su}(n)$ the Killing form reduces to $(Q_\alpha, Q_\beta) = 2n\,\mathrm{tr}(Q_\alpha Q_\beta)$. This orthogonality restricts U, though not completely. The new

Q_α's generate a Cartan subalgebra Killing-orthogonal to the original Cartan subalgebra. The new ladder operators contribute to the interaction:

$$H^{(j,j')} \propto \sum_{\beta=1}^{c-r} J_\beta^{(j,j')} \left(L_{+\beta}^{(j)} L_{-\beta}^{(j')} + \text{h.c.} \right). \tag{3.10}$$

In the $\mathfrak{su}(2)$ example, U can be represented by the matrix $\left[\begin{smallmatrix} a & -b^* \\ b & a^* \end{smallmatrix}\right]$, wherein $a, b \in \mathbb{C}$ and $|a|^2 + |b|^2 = 1$. The procedure restricts U only via the Killing-orthogonality of $U^\dagger \sigma_z U$ to U. We enforce only this restriction in Appendix B.2. Here, we choose a U for pedagogical simplicity: $U = (\mathbb{1} + i\sigma_y)/\sqrt{2}$, such that $Q_{\alpha+r} = Q_2 = \sigma_x$. The new ladder operators, $\sigma_{\pm x} := \left(\frac{\mathbb{1}+i\sigma_y}{\sqrt{2}}\right) \sigma_{\pm z} \left(\frac{\mathbb{1}+i\sigma_y}{\sqrt{2}}\right)$, create and annihilate quanta of the x-component of the angular momentum. The interaction becomes

$$H^{(j,j')} \propto \sum_{\beta=z,x} J_\beta^{(j,j')} \left(\sigma_{+\beta}^{(j)} \sigma_{-\beta}^{(j')} + \text{h.c.} \right). \tag{3.11}$$

We repeat the preceding steps: write out the form of a general $U \in \mathcal{G}$. Conjugate each element of the original Cartan-Weyl basis with U. Constrain U such that the new Q_α's are orthogonal to each other and to the older Q_α's. Include the new Q_α's in our preferred basis for the algebra. Form a term, in $H^{(j,j')}$, from the new ladder operators $L_{\pm\beta}$.

Each Cartan-Weyl basis contributes r elements Q_α to the preferred basis. The basis contains c elements, so we form c/r mutually orthogonal Cartan-Weyl bases. c/r equals an integer for the finite-dimensional semisimple complex Lie algebras, according to Proposition 1 in Section 3.3.1. Table 1 confirms the claim for the simple Lie algebras. Our algebra's finite dimensionality ensures that our procedure halts. The two-body interaction is now

$$H^{(j,j')} = \sum_{\beta=1}^{\frac{c-r}{2}\cdot\frac{c}{r}} J_\beta^{(j,j')} \left(L_{+\beta}^{(j)} L_{-\beta}^{(j')} + \text{h.c.} \right). \tag{3.12}$$

In the $\mathfrak{su}(2)$ example, $c/r = 3/1 = 3$. Hence, we construct three Cartan-Weyl bases using two SU(2) elements. If the first unitary was $(\mathbb{1} + i\sigma_y)/\sqrt{2}$, the second unitary is $(\mathbb{1} - i\sigma_x + i\sigma_y + i\sigma_z)/2$, to within a global phase. Consequently, $Q_3 = \sigma_y$, the preferred basis for $\mathcal{A}$ is $\{\sigma_z, \sigma_x, \sigma_y\}$, and

$$H^{(j,j')} = \sum_{\beta=x,y,z} J_\beta^{(j,j')} \left(\sigma_{+\beta}^{(j)} \sigma_{-\beta}^{(j')} + \text{h.c.} \right). \tag{3.13}$$

Next, we constrain the interaction to conserve every global charge:

$$[H^{(j,j')}, Q_\alpha^{\rm tot}] = 0 \quad \forall \alpha = 1, 2, \ldots, c. \tag{3.14}$$

The commutation relations (3.14) constrain the hopping frequencies $J_\alpha^{(j,j')}$. The frequencies must equal each other in the $\mathfrak{su}(2)$ example: $J_\alpha^{(j,j')} \equiv J^{(j,j')}$ for all α. We show this in Appendix B.2.3. In this case, the Hamiltonian simplifies to the familiar Heisenberg model:

$$H^{(j,j')} = J^{(j,j')} \vec{\sigma}^{(j)} \cdot \vec{\sigma}^{(j')} = J^{(j,j')} \sum_{\alpha=x,y,z} \sigma_\alpha^{(j)} \sigma_\alpha^{(j')} \tag{3.15}$$

We have constructed a two-body interaction $H^{(j,j')}$ that couples subsystems j and j'. We construct k-body terms $H^{\left(j,j',\ldots,j^{(k)}\right)}$ by multiplying two-body terms (3.12) together, constraining the couplings such that $[H^{\left(j,j',\ldots,j^{(k)}\right)}, Q_\alpha^{\rm tot}] = 0$, and subtracting off any fewer-body terms that appear in the product. Section 3.3.1 details the formalism. In the $\mathfrak{su}(2)$ example, a three-body interaction has the form (see Appendix B.2)

$$H^{(j,j',j'')} \propto H^{(j,j')} H^{(j',j'')} H^{(j'',j)} \tag{3.16}$$

$$\propto J^{(j,j',j'')} [(\sigma_x \sigma_y \sigma_z + \sigma_y \sigma_z \sigma_x + \sigma_z \sigma_x \sigma_y) - (\sigma_z \sigma_y \sigma_x + \sigma_x \sigma_z \sigma_y + \sigma_y \sigma_x \sigma_z)]. \tag{3.17}$$

wherein $J^{(j,j',j'')} \in \mathbb{R}$.

The Hamiltonian we constructed may be integrable. For example, the one-dimensional (1D) nearest-neighbor Heisenberg model is integrable [78]. Integrable Hamiltonians have been featured in studies of noncommuting charges in thermodynamics [79]. But one might wish for the system to thermalize as much as possible, as is promoted by nonintegrability [66, 80]. Geometrically nonlocal couplings, many-body interactions, and multidimensional lattices tend to break integrability. Hence one can add terms $H^{(j,j')}$ and $H^{(j,j',\ldots,j^{(k)})}$ to the global Hamiltonian $H^{\rm tot}$, and keep growing the lattice's dimensionality, until $H^{\rm tot}$ becomes nonintegrable. Nonintegrability may be diagnosed with, e.g., energy-gap statistics [66]. In the $\mathfrak{su}(2)$ example, one can break integrability by creating next-nearest-neighbor couplings or by making the global system two-dimensional [45].

3.4 $\mathfrak{su}(3)$ example

Section 3.3.2 illustrated the Hamiltonian construction procedure with the algebra $\mathfrak{su}(2)$. The $\mathfrak{su}(2)$ example offered simplicity but lacks other algebras' richness. In other algebras,

each Cartan-Weyl basis contains multiple Hermitian operators and ladder-operator pairs. We demonstrate how our procedure accommodates this richness by constructing a two-body Hamiltonian that transports $\mathfrak{su}(3)$ elements locally while conserving them globally. Such Hamiltonians may be engineered for superconducting qutrits, as sketched in Chapter 7. However, this $\mathfrak{su}(3)$ example only illustrates our more general procedure, which works for all finite-dimensional semisimple complex Lie algebras on which the Killing form induces a metric.

Each basis for $\mathfrak{su}(3)$ contains $c = 8$ elements. The most famous basis consists of the Gell-mann matrices, $\tau_{i=1,2,\ldots,8}$ [81]. The τ_i generalizes the Pauli matrices in certain ways, being traceless and Killing-orthogonal. From the Gell-mann matrices is constructed the conventional Cartan-Weyl basis [82], reviewed in Appendix B.5. The $r = 2$ Hermitian elements are Gell-mann matrices:

$$Q_1 = \tau_3, \quad \text{and} \quad Q_2 = \tau_8. \tag{3.18}$$

Q_1 and Q_2 belong in the preferred basis of charges for $\mathfrak{su}(3)$. For pedagogical clarity, we will identify all the charges before addressing the ladder operators.

A general element $U \in \mathrm{SU}(3)$ contains eight real parameters. In the Euler parameterization [83],

$$U = e^{i\tau_3\phi_1/2} e^{i\tau_2\phi_2/2} e^{i\tau_3\phi_3/2} e^{i\tau_5\phi_4/2} e^{i\tau_3\phi_5/2} e^{i\tau_2\phi_6/2} e^{i\tau_3\phi_7/2} e^{i\tau_8\phi_8/2} . \tag{3.19}$$

The parameters $\phi_1, \phi_3, \phi_5, \phi_7 \in [0, 2\pi)$; $\phi_2, \phi_4, \phi_6 \in [0, \pi]$; and $\phi_8 \in [0, 2\sqrt{3}\pi)$. We now constrain U, identifying the instances U_i that map the first charges to $Q_3 = U_\mathrm{i}^\dagger Q_1 U_\mathrm{i}$ and $Q_4 = U_\mathrm{ii}^\dagger Q_2 U_\mathrm{ii}$ that are Killing-orthogonal to each other and to the original charges. Appendix B.5 contains the details. We label with a superscript (i) the parameters used to fix U_i: $\phi_1^{(\mathrm{i})}$, $\phi_3^{(\mathrm{i})}$, $\phi_7^{(\mathrm{i})}$, $\phi_8^{(\mathrm{i})}$, and $n^{(\mathrm{i})}$. For convenience, we package several parameters together: $a^{(\mathrm{i})} := \frac{1}{2}\left(\phi_3^{(\mathrm{i})} - \phi_7^{(\mathrm{i})} - \sqrt{3}\phi_8^{(\mathrm{i})} + \pi n^{(\mathrm{i})} + \frac{\pi}{2}\right)$, and $b^{(\mathrm{i})} := a^{(\mathrm{i})} + \phi_7^{(\mathrm{i})}$. In terms of these parameters, the new charges have the forms (see Appendix B.5)

$$\begin{aligned} Q_3 = \frac{1}{\sqrt{3}}\Big[&(-1)^{n^{(\mathrm{i})}+1}\sin\big(a^{(\mathrm{i})} - b^{(\mathrm{i})}\big)\tau_1 - (-1)^{n^{(\mathrm{i})}}\cos\big(a^{(\mathrm{i})} - b^{(\mathrm{i})}\big)\tau_2 - \sin\big(a^{(\mathrm{i})}\big)\tau_4 \\ &- \cos\big(a^{(\mathrm{i})}\big)\tau_5 + \sin\big(b^{(\mathrm{i})}\big)\tau_6 + \cos\big(b^{(\mathrm{i})}\big)\tau_7\Big] \quad \text{and} \end{aligned} \tag{3.20}$$

$$\begin{aligned} Q_4 = \frac{(-1)^{n^{(\mathrm{i})}}}{\sqrt{3}}\Big[&(-1)^{n^{(\mathrm{i})}+1}\cos\big(a^{(\mathrm{i})} - b^{(\mathrm{i})}\big)\tau_1 + (-1)^{n^{(\mathrm{i})}}\sin\big(a^{(\mathrm{i})} - b^{(\mathrm{i})}\big)\tau_2 + \cos\big(a^{(\mathrm{i})}\big)\tau_4 \\ &- \sin\big(a^{(\mathrm{i})}\big)\tau_5 + \cos\big(b^{(\mathrm{i})}\big)\tau_6 - \sin\big(b^{(\mathrm{i})}\big)\tau_7\Big]. \end{aligned} \tag{3.21}$$

Q_3 has the same form as Q_5 and Q_7, which satisfy the same Killing-orthogonality conditions. Similarly, Q_4 has the same form as Q_6 and Q_8. We denote the later charges' parameters by $a^{(\ell)}$ and $b^{(\ell)}$. These parameters are more restricted (see Appendix B.5). We have identified our preferred basis of charges.

Let us construct the ladder operators and Hamiltonian. Each Cartan-Weyl basis contains $c - r = 8 - 2 = 6$ ladder operators. The conventional Cartan-Weyl basis contains ladder operators formed from Gell-man matrices:

$$L_{\pm 1} := \tfrac{1}{2}(\tau_1 \pm i\tau_2), \quad L_{\pm 2} := \tfrac{1}{2}(\tau_4 \pm i\tau_5), \quad \text{and} \quad L_{\pm 3} := \tfrac{1}{2}(\tau_6 \pm i\tau_7). \tag{3.22}$$

Transforming these operators with unitaries $U_{\text{ii,iii,iv}}$ yields $L_{\pm 4}$ through $L_{\pm 12}$, whose forms appear in Appendix B.5. From each ladder operator, we form one term in the two-body Hamiltonian (3.6).

Finally, we determine the hopping frequencies $J_\alpha^{(j,j')}$, demanding that $[H^{(j,j')}, Q_\alpha^{\text{tot}}] = 0$ for all α. For all possible values of the $a^{(\ell)}$, $b^{(\ell)}$, and $n^{(\ell)}$, if all the frequencies are nonzero, then all the frequencies equal each other. We set $J_\alpha^{(j,j')} \equiv \frac{4}{3} J^{(j,j')}$, such that

$$H^{(j,j')} = J^{(j,j')} \sum_{\alpha=1}^{8} \tau_\alpha^{(j)} \tau_\alpha^{(j')} \propto \sum_{\alpha=1}^{8} Q_\alpha^{(j)} Q_\alpha^{(j')}. \tag{3.23}$$

The Hamiltonian collapses to a simple form analogous to the $\mathfrak{su}(2)$ example's Eq. (3.15) (see Appendix B.3).

3.5 Summary & Outlook

We have presented a procedure for constructing Hamiltonians that transport noncommuting charges locally while conserving the charges globally. The Hamiltonians can couple arbitrarily many subsystems together and can be integrable or nonintegrable. The procedure produces, as well as Hamiltonians, preferred bases of charges that are (i) overtly transported locally and conserved globally and (ii) Killing-form-orthogonal. This construction works whenever the charges form a finite-dimensional semisimple complex Lie algebra on which the Killing form induces a metric. Whether there exists any Hamiltonians that transport charges locally, while conserving the charges globally, outside of those found by our procedure, is an interesting open question for theoretical exploration.

This work systematically bridges noncommuting thermodynamic charges from abstract quantum information theory to condensed matter, AMO physics, and high-energy and

nuclear physics. The mathematical results that have accrued can now be tested experimentally via our construction. When we first wrote reference [2], we presented the following predictions that merited experimental exploration: (i) the emergence of the quantum equilibrium state in [43, 42, 12], (ii) the decrease in entropy production by noncommuting charges [14], (iii) applications of the entropy decrease to quantum engines [84], (iv) the conjecture that noncommuting charges hinder thermalization [13], and (v) the conjecture's application to quantum memories. Since then, the first bullet has been experimentally verified [46] using one of the Hamiltonians identified in this work[2]. Furthermore, other results have since been proposed that merit testing—increases in entanglement [3], critical phases [1], etc. Such experiments' benefits include the simulation of quantum systems larger than what classical computers can simulate, uncovering behaviours not predicted by theory, and grounding abstract QIT thermodynamics in physical reality.

As mentioned above, the Heisenberg model (3.13) can be implemented with various hardware. Reference [45] details how to harness these setups to study noncommuting thermodynamic charges. Here, we present a more intricate proposal by employing current superconducting qubit experimental platforms to implement our general framework's $\mathfrak{su}(3)$ instance.

Superconducting circuits can serve as qudits with Hilbert-space dimensionalities $d \geq 2$ [85]. Qutrits have been realized with transmons [86]. The lowest two energy levels often serve as a qubit, but the second energy gap nearly equals the first. Hence, the third level can be addressed relatively easily [87]. Superconducting qutrits offer a tabletop platform for transporting and conserving $\mathfrak{su}(3)$ charges as in Section 3.4.

Experiments with ≤ 5 qutrits have been run [88, 89]. Furthermore, many of the tools used to control and measure superconducting qubits can be applied to qutrits [87, 90, 91, 92, 93]. T_2^* relaxation times of ~ 39 μs, for the lowest energy gap, and ~ 14 μs, for the second-lowest gap, have been achieved [89]. Meanwhile, two-qutrit gates can be realized in $\sim 10 - 10^2$ ns [89, 94, 95]. Some constant number of such gates may implement one three-level gate that simulates a term in our Hamiltonian. If the number is order-10, information should be able to traverse an 8-qutrit system ~ 10 times before the qutrits decohere detrimentally. According to numerics in [13], a small subsystem nears thermalization once information has had time to traverse the global system a number of times linear in N. Therefore, realizations of our Hamiltonians are expected to thermalize the system internally. The states of small subsystems, such as qutrit pairs, can be read out via quantum state tomography [87, 90, 91, 92, 93]. Hence, by simulating the Hamiltonians constructed here, superconducting qutrits and other platforms can import noncommuting

[2]To be fair, this same Hamiltonian had come up in earlier literature on noncommuting charges[12]

charges from quantum thermodynamics to many-body physics.

Chapter 4

Noncommuting charges can increase average entanglement

This chapter is based on reference [3] and overlaps with its text.

4.1 Introduction

In Chapter 3, we successfully connected noncommuting charge physics with many-body physics and experiments. Now, we study the implications of charge noncommutation in quantum many-body theory. Entanglement tends to accompany thermalization in quantum systems. Justifying how a pure initial state can evolve unitarily to a state that looks thermal locally requires entanglement. Thus, entanglement serves as an ideal focal point for exploring the impacts of charge noncommutation.

Entanglement has illuminated quantum many-body phenomena from space-time's structure [96, 97, 98] to phases [99, 100, 101, 102] and thermalization [69]. A large, isolated many-body system thermalizes internally when evolved under a nonintegrable Hamiltonian (Section 2.3). Such dynamics tend to imbue an initial pure state, after long times, with properties closely approximated in pure states drawn randomly from the available Hilbert space. The random state's average bipartite entanglement is quantified with a Page curve [103]: consider partitioning the system into two subsystems, calculating a subsystem's entanglement entropy, and averaging the entropy over states drawn randomly from the full system's Hilbert space. The average, plotted against the subsystem's size,

forms a Page curve. (We present a more technical introduction to Page curves in Section 4.2).

Page curves have been studied in the context of Abelian symmetries, i.e., commuting charges [104, 105]. This is done by drawing random pure states from a chosen particle-number sector, a microcanonical subspace $\mathcal{S}$, instead of the full Hilbert space. More generally, the system may have multiple charges that commute with each other, so that the symmetry remains Abelian. $\mathcal{S}$ can be chosen to be an eigenspace shared by the charges. We aim to quantify how charges' noncommutation—a symmetry's non-Abelian nature—affects Page curves.

This comparison calls for two models that parallel each other closely, yet differ in whether their charges commute. Whether such models exist, what "parallel closely" should mean, and how to construct such models is unclear. We therefore posit criteria to encapsulate models' analogousness. Furthermore, we construct two models that meet these criteria. Each model consists of two-qubit sites. Every local charge is a product of two-qubit Pauli operators and/or identity operators.

We compare these models' Page curves in two settings. Conventional thermodynamics suggests one: a microcanonical subspace, a simultaneous eigenspace of the charges. The noncommuting-charge model has only one microcanonical subspace. Thus, we also identify approximate microcanonical subspaces (see Section 2.2.2) in the noncommuting-charge model and analogs in the commuting-charge model. Each pair of such subspaces yields another pair of Page curves.

We estimate the Page curves numerically and, in the microcanonical comparison, analytically. In every setting where we can do so, the nonconcommuting-charge Page curve lies above the commuting-charge curve. On average, therefore, charges' noncommutation appears to promote entanglement. For systems of $N \gg 1$ sites, the Page curves' separation decreases, but only polynomially in the system size, as $1/N$. We posit that the gap arises solely from whether the charges commute, due to the close parallel between our two models. This conjecture calls for testing with more parallel models and for more-general explanations, which we partially leave as a challenge for future research.

The rest of this paper is organized as follows. In Section 4.2, we overview Page curves; in Section 4.3, we present the analogous models. We compare the models' Page curves using microcanonical subspaces (Section 4.4), then using approximate microcanonical subspaces (Section 4.5). Section 4.6 concludes with opportunities established by this work.

4.2 Page-curve background

To introduce Page curves, we must introduce entanglement entropy. Consider an isolated ("global") system, associated with a Hilbert space $\mathcal{H}$, in a pure state $|\Phi\rangle$. Denote by A a subsystem associated with a dimension-D_A Hilbert space. Denote by B the rest of the system. The full system's Hilbert space is the tensor product of the subsystems' Hilbert spaces. The entanglement entropy is the von Neumann entropy of $\rho_A \coloneqq \mathrm{Tr}_B(|\Phi\rangle\langle\Phi|)$ [37]:

$$S_{\mathrm{E}} \coloneqq S(\rho_A) \coloneqq -\mathrm{Tr}(\rho_A \log \rho_A) \leq \log D_A. \tag{4.1}$$

The logarithms are base e, giving entropies in units of nats. A is entangled with B if $S_{\mathrm{E}} > 0$.

The Page curve quantifies the average entanglement in a subspace $\mathcal{S}$ of interest. Let A consist of N_A identical sites, and let B consist of N_B more, such that $N_A + N_B = N$. Consider selecting a global pure state from $\mathcal{S}$ uniformly at random according to the Haar measure [106]. Calculating S_{E}, then averaging over Haar-random states, yields

$$\langle S_{\mathrm{E}} \rangle_{\mathcal{S}} \coloneqq -\langle \mathrm{Tr}(\rho_A \log \rho_A) \rangle_{\mathcal{S}} \,. \tag{4.2}$$

Plotted against N_A, $\langle S_{\mathrm{E}} \rangle_{\mathcal{S}}$ forms the Page curve for subspace $\mathcal{S}$ [103].

We estimate the curve numerically as follows. Denote by $\{|\psi_\ell\rangle\}$ any basis for the subspace. We weight the ℓ^{th} element with a random number c_ℓ drawn from a complex normal distribution. Summing the weighted elements, and renormalizing with a constant C_{norm}, we form a Haar-random state: $\frac{1}{C_{\mathrm{norm}}} \sum_\ell c_\ell |\psi_\ell\rangle$. We sample 10^3–10^4 states, calculate each state's S_{E}, and average to estimate the Page curve.

In the best-known example, no charges constrain the system [103]. Denote by $\mathcal{H}$ the full Hilbert space and by d the local dimension (of a site's Hilbert space). The unconstrained Page curve is, for $N_A \leq N_B$,

$$\langle S_E \rangle_{\mathcal{H}} \approx N_A \log d - \frac{1}{2} d^{N_A - N_B}. \tag{4.3}$$

The terms in Eq. (4.3) stem from different physics, as do the analogous terms in constrained Page curves. Consider averaging the Haar-random states over $\mathcal{S}$ before calculating any entropy. The averaged state, $\langle \rho \rangle_{\mathcal{S}}$, is the maximally mixed state within $\mathcal{S}$. Tracing out B yields $\langle \rho_A \rangle_{\mathcal{S}} \coloneqq \mathrm{Tr}_B(\langle \rho \rangle_{\mathcal{S}})$, whose entropy follows from state-counting arguments (App. C.1). We therefore call $S\left(\langle \rho_A \rangle_{\mathcal{S}}\right)$ the subspace-$\mathcal{S}$ Page curve's state-counting term. In terms of it, the curve decomposes as

$$\langle S_{\mathrm{E}} \rangle_{\mathcal{S}} = S\left(\langle \rho_A \rangle_{\mathcal{S}}\right) + \left[\langle S_{\mathrm{E}} \rangle_{\mathcal{S}} - S\left(\langle \rho_A \rangle_{\mathcal{S}}\right)\right]. \tag{4.4}$$

Since $\langle \rho \rangle_{\mathcal{S}}$ is maximally mixed, $S\left(\langle \rho_A \rangle_{\mathcal{S}} \right)$ equals the greatest possible entropy: $\langle S_{\rm E} \rangle_{\mathcal{S}} \leq S\left(\langle \rho_A \rangle_{\mathcal{S}} \right)$. Hence the bracketed term in Eq. (4.4) is ≤ 0. That term encodes the interference between different states' contributions to the Page curve's Haar average. This interference term is exponentially small in $N_B - N_A$ [103]. In the unconstrained curve (4.3), $N_A \log d$ is the state-counting term, and $-\frac{1}{2} d^{N_A - N_B}$ is the interference term.

4.3 Analogous noncommuting-charge and commuting-charge models

We aim to identify how charges' noncommutation affects the Page curve. Therefore, we need two models that differ in whether their charges commute and otherwise differ minimally. Whether such models exist, what "differ minimally" should mean, and how to construct such models is unclear. For instance, the most commonly studied non-Abelian symmetry group is SU(2); the associated charges are the Pauli operators, X, Y, and Z. How to construct an analogous model with three commuting charges is not obvious. For example, the group $\mathrm{U}(1)^{\times 3}$ is generated by three charges that commute but are not multiplicatively interrelated. In contrast, $XY = iZ$.

We address this challenge by positing five criteria that capture what renders the model with noncommuting charges and commuting charges analogous. Then, we construct two models that meet these criteria. As in the last chapter, we denote by $Q_\alpha^{\rm tot}$ the global noncommuting charges. We denote by $C_\alpha^{\rm tot}$ the global commuting charges. The criteria concern also the subspaces used to calculate the Page curves. Denote by $|\psi\rangle$ any state from the noncommuting-charge subspace $\mathcal{Q}$. Measuring $Q_\alpha^{\rm tot}$ yields outcome μ with some probability. This probability, averaged over the $|\psi\rangle$, we denote by $p_\alpha^{\mathcal{Q}}(\mu)$. Define $p_\alpha^{\mathcal{C}}(\mu)$ analogously for the commuting-charge subspace $\mathcal{C}$.

We define as analogous any commuting-charge and noncommuting-charge models that satisfy five criteria:

1. In each model, the system consists of N sites, each formed from a d-level qudit. Each model has c charges.

2. Each global charge (i) is a sum of single-site observables and (ii) acts nontrivially and identically on all sites.

3. Each charge $Q_\alpha^{\rm tot}$ has the same spectrum as its analog $C_\alpha^{\rm tot}$.

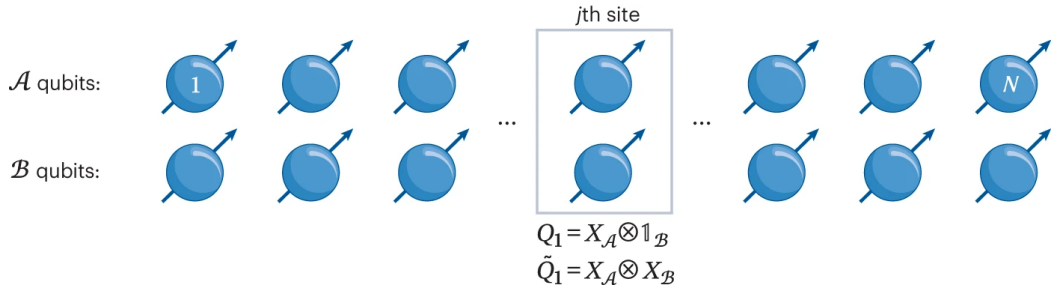

Figure 4.1: **Analogous noncommuting-charge and commuting-charge models.** Each model consists of N sites. A site consists of two qubits, a and b. The local noncommuting observables of interest include Q_1; and the local commuting observables, C_1.

4. Any two commuting charges form a product analogous to the analogous noncommuting charges' product.

5. The constrained subspaces, $\mathcal{Q}$ and $\mathcal{C}$, are such that $p_\alpha^\mathcal{Q}(\mu) = p_\alpha^\mathcal{C}(\mu)$.

We now construct two models that satisfy the criteria (Fig. 4.1). Each global charge ($Q_\alpha^{\rm tot}$ or $C_\alpha^{\rm tot}$) follows from summing single-site observables Q_α or C_α. Denote by $Q_\alpha^{(j)}$ an observable defined on site j's Hilbert space, and define $C_\alpha^{(j)}$ analogously. As in the last chapter, the global charges are extensive:

$$Q_\alpha^{\rm tot} := \sum_{j=1}^{N} \mathbb{1}^{\otimes(j-1)} \otimes Q_\alpha^{(j)} \otimes \mathbb{1}^{\otimes(N-j)} \equiv \sum_{j=1}^{N} Q_\alpha^{(j)}, \tag{4.5}$$

and $C_\alpha^{\rm tot} := \sum_{j=1}^{N} C_\alpha^{(j)}$.

The noncommuting charges can generate $\mathfrak{su}(2)$ if each site contains one qubit ($d = 2$). By criterion 2, three charges impose up to three restrictions on each site[1]. A fourth restriction follows from the normalization of the site's state. These restrictions suggest that, to support a model with three commuting charges, d should be ≥ 4. Choosing $d = 4$ for simplicity, we form each site's qudit from two qubits, a and b. The noncommuting local observables are

$$Q_1 = X_a \otimes \mathbb{1}_b, \quad Q_2 = Y_a \otimes \mathbb{1}_b, \text{ and } Q_3 = Z_a \otimes \mathbb{1}_b; \tag{4.6}$$

and the commuting local observables are

$$C_1 = X_a \otimes X_b, \quad C_2 = Y_a \otimes Y_b, \text{ and } C_3 = Z_a \otimes Z_b. \tag{4.7}$$

[1]The restrictions are on the global system. Depending on the charges, there could be less than three independent restrictions per site.

It is straightforward to check that $[Q_\alpha, Q_\beta] = 2i\epsilon_{\alpha\beta\gamma}Q_\gamma$ and $[C_\alpha, C_\beta] = 0$.

These models satisfy criteria 1–3 overtly and by simple calculation. Criterion 4 concerns products of charges. For unequal indices $\alpha, \beta, \gamma \in \{1, 2, 3\}$,

$$Q_\alpha Q_\beta = i\epsilon_{\alpha\beta\gamma}Q_\gamma, \quad \text{and} \quad C_\alpha C_\beta = -C_\gamma. \tag{4.8}$$

These equations parallel each other because multiplying two distinct charges yields the third charge times a constant. Furthermore, $Q_\alpha Q_\alpha = C_\alpha C_\alpha = \mathbb{1} \ \forall \alpha$.

Criterion 5 is satisfied if we choose subspaces adroitly. In the microcanonical subspaces identified below, the $p_\alpha^{\mathcal{Q}}(\mu)$'s and $p_\alpha^{\mathcal{C}}(\mu)$'s equal Kronecker delta functions and so each other. As detailed below, we can also construct approximate microcanonical subspaces such that $p_\alpha^{\mathcal{Q}}(\mu) = p_\alpha^{\mathcal{C}}(\mu)$ for all α and μ.

4.4 Microcanonical-subspace comparison

The noncommuting-charge model has exactly one microcanonical subspace, $\mathcal{Q}_0$: the eigenvalue-0 eigenspace shared by $Q_{1,2,3}^{\text{tot}}$. This subspace exists only if N is even. The analogous commuting-charge subspace, $\mathcal{C}_0$, is the eigenvalue-0 eigenspace shared by $C_{1,2,3}^{\text{tot}}$. This subspace exists only if N equals a multiple of four (App. C.1.2).

We estimate Page curves numerically using the procedure outlined in Section 4.2 and using [107]. Here, $\langle S_{\text{E}} \rangle_{\mathcal{S}}$ denotes the Page curve for a subspace $\mathcal{S}$, and $\langle S_E \rangle_{\mathcal{H}}$ denotes the unrestricted Page curve (4.3). To highlight the gap between the noncommuting-charge and commuting-charge curves, we plot $\langle S_{\text{E}} \rangle_{\mathcal{S}} - \langle S_E \rangle_{\mathcal{H}}$ for $\mathcal{S} = \mathcal{Q}_0, \mathcal{C}_0$ in Fig. 4.2. At all partition locations N_A, the noncommuting-charge Page curve lies above the commuting-charge Page curve. For example, at the midpoint ($N_A = N/2$), the gap is 0.124 nats (17.8% of the average of the two Page curves at $N_A = N/2$) when $N = 4$ and 0.0797 nats (10.5%) when $N = 8$. In this microcanonical case, therefore, the subspace constrained by noncommuting charges has more entanglement, on average.

We posit the following possible explanations for this phenomenon in our setting. First, the subspace's dimensionality upper-bounds the entanglement entropy: $S_{\text{E}} \leq \log D_A$ [Eq. (4.1)]. The bound tends to approximate random states' entropies. Hence one might expect a higher Page curve of whichever model has the larger subspace. Indeed, the noncommuting-charge subspace is of dimensionality 32, when $N = 4$, exceeding the commuting-charge dimensionality of 24. When $N = 8$, the noncommuting-charge dimensionality is 3584, again exceeding its commuting-charge analog, 2520. Our analytical results below

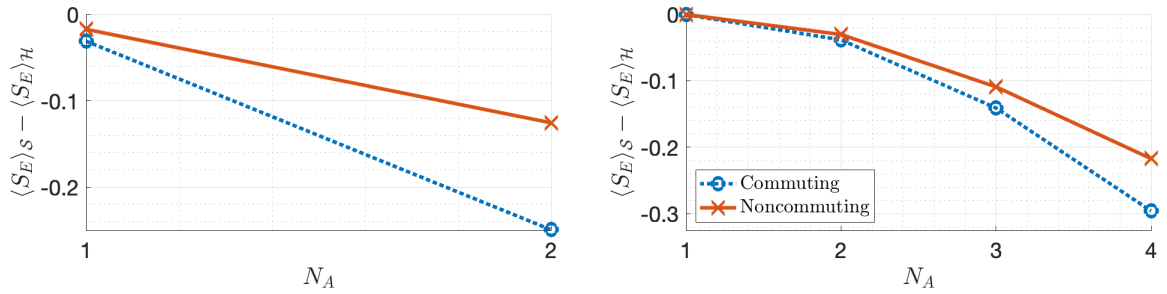

(a) Global-system size $N = 4$

(b) Global-system size $N = 8$

Figure 4.2: **Page curves constructed from microcanonical subspaces.** $\langle S_{\mathrm{E}} \rangle_{\mathcal{S}}$ denotes any Page curve restricted by charges; and $\langle S_E \rangle_{\mathcal{H}}$, the unrestricted Page curve. The red x's form the noncommuting-charge model's Page curve, and the circular blue markers form the commuting-charge model's Page curve. The connecting lines guide the eye. We calculated the top panel's ($N = 4$) Page curves from 10^4 samples each and the bottom panel's ($N = 8$) Page curves from 10^3 samples each. The x-axis ends at $N_A = N/2$ for conciseness; the Page curves are symmetric according to numerics. The error bars are present but are too small to see.

agree at large N: the noncommuting-charge curve lies above the commuting-charge curve if approximated with the state-counting term, which depends essentially on subspace dimensionality.

We expect this dimensionality argument to explain our results only partially, the Page curves do not saturate the upper bound (4.1). Hence we posit that, when the compared subspaces have similar dimensionalities, their minimally entangled bases may help determine the Page curves' relative locations. The commuting-charge model's microcanonical subspace, $\mathcal{C}_0$, has a tensor-product basis. The reason is, every global charge C_α^{tot} commutes with all the subsystem charges $C_{\alpha'}^{(A)}$ and $C_{\alpha''}^{(B)}$. In contrast, in the noncommuting-charge model, each global charge Q_α^{tot} fails to commute with some subsystem charges $Q_{\alpha'}^{(A)}$ and $Q_{\alpha''}^{(B)}$. Hence the microcanonical subspace $\mathcal{N}_0$ has no tensor-product basis. Therefore, the minimally entangled basis has more entanglement in the noncommuting-charge model. Hence one might expect a higher Page curve there. Additionally, in App. C.3, we show that sequentially introducing charges restricts the Page curve subadditively if the charges fail to commute, and superadditively if the charges commute, at finite N.

We now analytically calculate the difference between the noncommuting-charge and commuting-charge Page curves in these microcanonical subspaces at large N. Recall that

the interference term [Eq. (4.4)] is exponentially small in $N_B - N_A$ [103]. Consequently, the state-counting term approximates the Page curve when $N_B - N_A \gg 1$ [2]. We calculate state-counting terms in App. C.1, using large-N expansions. We assume that $N_A, N_B = \mathcal{O}(N)$; the subsystems' sizes are near their average values. Both subspaces' Page curves have the leading, $\mathcal{O}(N^0)$ term

$$L \coloneqq N_A \log d - \frac{3}{2} \log \frac{N}{N_B} + \frac{3N_A}{2N} \,. \tag{4.9}$$

The noncommuting-charge Page curve is

$$L + \frac{3N_A}{4N^2} + \frac{N_A^2}{2N^2 N_B} + \mathcal{O}\left(N^{-\frac{3}{2}}\right) , \tag{4.10}$$

and the commuting-charge Page curve is [3]

$$L + \frac{3N_A}{4N^2} - \frac{N_A^2}{2N^2 N_B} + \mathcal{O}\left(N^{-\frac{3}{2}}\right) . \tag{4.11}$$

The noncommuting-charge Page curve is greater by an amount $\frac{N_A^2}{N^2 N_B}$, at leading order. The difference decreases as N grows. This decline is consistent with the correspondence principle [63]—as systems grow large, they grow classical. Noncommutation is nonclassical, so its effects on observable phenomena should diminish as $N \to \infty$ [13]. More precisely, the charge densities Q_α^{tot}/N have commutators that vanish in the thermodynamic limit [108, 13]: $[Q_\alpha^{\text{tot}}/N,\ Q_{\alpha'}^{\text{tot}}/N] \to 0$, for all α and α', as $N \to \infty$. However, the Page-curve difference shrinks relatively slowly—as $1/N$, rather than exponentially—as N grows.

To be clear, we have posited explanations for the difference we observed in the model's Page curve. However, we do not prove that one of these reasons is the cause of the difference in the entanglement entropy.

4.5 Approximate-microcanonical-subspace comparison

Having compared our two models using microcanonical subspaces, we progress to approximate microcanonical subspaces, generalizations that accommodate charge noncommutation [13, 46, 45]. Instead of having well-defined values in an approximate microcanonical

[2] Computational restrictions prevent $N_B - N_A$ from growing very large in the numerics. Therefore, we refrain from plotting our analytics in Fig. 4.2.

[3] In both expressions, the $\mathcal{O}\left(N^{-\frac{3}{2}}\right)$ term may vanish, so the next nonzero term may be $\mathcal{O}\left(N^{-2}\right)$.

subspace, the charges have fairly well-defined values: measuring any $Q_\alpha^{\rm tot}$ has a high probability of yielding an outcome close to the expected value. This section outlines how to construct analogous approximate microcanonical subspaces in the noncommuting-charge and commuting-charge models. We then compare the models' Page curves numerically. The noncommuting-charge Page curve is always higher, as in the microcanonical-subspace comparison.

One can construct as follows approximate microcanonical subspaces in the noncommuting-charge model. Define the a-qubit magnetization $Z_a^{\rm tot} := \sum_{j=1}^N Z_a$, which has eigenvalues $2m$. Define the a-type spin-squared operator $(\vec{S}_a^{\rm tot})^2 := \sum_{a=1}^3 (Q_a^{\rm tot})^2$, which has eigenvalues $s(s+1)$ (we set $\hbar = 1$). $(\vec{S}_a^{\rm tot})^2$ shares with $Z_a^{\rm tot}$ eigenspaces $\mathcal{Q}$ labeled by the quantum numbers (s, m). Thus, $(\vec{S}_a^{\rm tot})^2 \otimes \mathbb{1}_b^{\rm tot}$ shares with $Q_3^{\rm tot}$ eigenspaces $\mathcal{Q}$ labeled by the quantum numbers (s, m). Some such eigenspaces are approximate microcanonical subspaces, we find by direct calculation. For each (s, m) value, we calculate the probability distributions $p_\alpha^{\mathcal{Q}}(\mu)$. Each distribution exhibits one peak, as required by the definition of "approximate microcanonical subspace," for certain (s, m) (App. C.4). Having identified approximate microcanonical subspaces defined by noncommuting charges, we construct analogs $\mathcal{C}$ defined by commuting charges. Appendix C.4 details the process. We identify six pairs of parallel (commuting-charge and noncommuting-charge) approximate microcanonical subspaces, labeled by $s = m = 1, N/2$, for $N = 4, 8$, as well as by $s = m = N/2$, for $N = 2, 6$.

We estimate each approximate microcanonical subspace's Page curve numerically. In every comparison, the noncommuting-charge ($\mathcal{Q}$) Page curve lies above its commuting-charge ($\mathcal{C}$) partner. An illustrative example is parameterized by $N = 8$ and $s = m = 1$. We compare the two curves at the midpoint $N_A = N/2$. Recall that $\langle S_{\rm E} \rangle_{\mathcal{S}}$ denotes a Page curve for the subspace $\mathcal{S}$. When $N_A = 4$, $\langle S_{\rm E} \rangle_{\mathcal{Q}} - \langle S_E \rangle_{\mathcal{C}} = 0.027$ nats, which is 7.11% of the two Page curves' average. The percent difference varies across the approximate-microcanonical-subspace pairs from 0.272% to 7.11%. Hence charges' noncommutation increases the average entanglement entropy in approximate microcanonical subspaces as in the microcanonical comparison.

4.6 Summary & Outlook

We have demonstrated that constrained charges' noncommutation promotes average entanglement. Numerical and analytical calculations support this conclusion in microcanonical and approximate microcanonical subspaces. In the microcanonical comparison, the Page-curve gap stems from the discrepancy between the subspaces' dimensionalities.

This work reveals how one hallmark of quantum theory—operators' failure to commute—influences another—entanglement. Due to entanglement's role in thermalization, our results are suggestive of how charges' noncommutation affects quantum many-body thermalization (as discussed more below).

Our conclusions rest on two models that resemble each other closely but differ in whether their charges commute. Our models can now be used to explore effects of charges' noncommutation on other quantum phenomena. Possibilities include chaos [109, 66], as analyzed with out-of-time-ordered correlators [110, 111, 112, 113] and random unitary circuits [114, 115]; bounds on quantum-simulation errors [116]; and quantum-machine-learning algorithms' performances [117].

After publishing rerence [3] we came across other works that concern non-Abelian symmetries' effects on entanglement entropy, but focus less on what charges' noncommutation changes and not on normal Page curves. For example, a non-Abelian symmetry raises the entanglement in Wess–Zumino–Witten models, $(1+1)$-dimensional conformal field theories with Lie-group symmetries [118, 119]. Second, holographic calculations highlight another correction that non-Abelian symmetries introduce into entanglement entropy [120, 121]. This correction appears to be negative. However, [120, 121] concern symmetry-resolved Page curves, in contrast with the conventional Page curves of [3]. A symmetry-resolved Page curve models the entanglement, averaged over time, of a system whose charges move only within A and within B, not between the subsystems. Conventional Page curves model less-restricted thermalization. Third, algebraic-quantum-field-theory calculations agree that non-Abelian symmetries should raise Page curves [122].

These works suggest several research opportunities. The entanglement entropy's increase merits checking with other comparable models à la Fig. 4.1. Additionally, one might adjust the Page-curve calculations following Marvian's revelation that local charge-conserving unitaries constrain global U's tightly [59]. Under locality constraints, the Haar distribution may model chaotic dynamics inaccurately.

Additionally, our results raise a puzzle. We find that charges' noncommutation promotes entanglement, which accompanies thermalization. This result links noncommuting charges to enhanced thermalization. In contrast, charges' noncommutation was found to restrict thermalizing behaviours in several ways detailed in Section 2.4.1. These results invite a more general understanding of when non-Abelian symmetries enhance or suppress entanglement and thermalization.

Apart from the foregoing theoretical opportunities, the difference between commuting-charge and noncommuting-charge entanglement entropies may be observed experimentally. For example, at the Page curves' midpoints ($N_A = N/2$), the difference is 0.124 nats in the

microcanonical setting for $N = 4$. A precision of ≈ 0.05 nats should, therefore, suffice to observe the difference. Such a precision has been achieved with trapped ions [123, 124, 125] and ultracold atoms [22, 126, 127]. Fortunately, noncommuting-charge thermodynamics has been shown to be observable on these platforms [2, 46].

Chapter 5

Noncommuting charges induce a critical phase in monitored quantum circuits

This chapter is based on reference [4] and overlaps with its text.

5.1 Introduction

In the preceding chapter, we found that the noncommutation of charges can lead to increased entanglement. This finding warrants further examination for two primary reasons. Entanglement is necessary to explain how closed quantum systems thermalize locally. In this sense, we say entanglement accompanies thermalization. However, numerous studies have suggested that noncommuting charges should impede thermalization (see Section 2.4.1). While the findings in Chapter 4 do not technically contradict these studies due to differences in the set-up, this discrepancy prompts a deeper inquiry. Secondly, our results were derived from a single model, raising the question of their generality. It is important to explore more diverse settings to understand the broader implications of noncommuting charges on entanglement dynamics. Another setting is in monitored quantum circuits.

Monitored quantum circuits are random unitary circuits augmented with mid-circuit projective measurements [114, 128, 129]. A typical monitored quantum circuit acts on a

chain of L qubits. The circuit contains layers of unitary gates applied between nearest-neighbour qubits. We say two-qubit gates acting on qubits 0-1, 2-3, etc., act on even-bonds, and others, on odd bonds. These layers alternate between the unitaries applied on the even and odd bonds, creating a so-called "brick-work" circuit as shown in Fig. 5.1. A unitary gate can also be applied between the first and Lth qubit during the even-bond layers to introduce periodic boundary conditions. Between each layer of unitaries, single-site projective measurements are performed with probability p on each qubit. Since the unitaries are random, the choice of measurement basis is arbitrary. A hallmark of monitored circuit is that they exhibit measurement-induced phase transitions due to the competition between entangling unitaries and disentangling measurements. These transitions have received significant attention recently (see the reviews [114, 128, 129] for a survey of the results). A measurement-induced phase transition is a transition between phases with distinct entanglement scalings: volume-lawindex (scaling as L in 1D) and area-law (constant, L^0, in 1D) [99, 100].

In principle, random circuits reduce quantum dynamics to their most fundamental aspects: unitarity and locality. This simplification allows for the examination of generic, model-independent properties of quantum systems. As a result, random circuits have emerged as a valuable tool for isolating specific properties to analyze their influence on entanglement dynamics. Monitored circuits, in particular, have been enhanced by incorporating commuting charge conservation [130, 131, 132, 133, 134, 135], targeted measurements of specific operators (such as the generators of the toric-code stabilizer) [136, 137], and the substitution of qubits with free fermions [138, 139, 140, 141, 142, 143]. Introducing a single charge, represented as a U(1) symmetry, did not significantly alter the entanglement dynamics; both volume-law and area-law entanglement persisted. The phase transition between two entanglement regimes occurred at a smaller value of p (at $p \approx 1/10$ instead of $p \approx 1/6$). To further understand the impact of noncommuting charges on entanglement, we explore monitored quantum circuits that incorporate such charges.

Having numerically constructed monitored circuits with noncommuting charges, it's sensible to extend our study to the influence of these charges on other phase transitions. The entanglement phase transition can equivalently be seen as a purification transition between a mixed phase and a pure phase [144]. When the measurement rate p is low, the chaotic dynamics scramble information about the initial state. Local measurements cannot extract that information in this mixed phase. An initially mixed state becomes pure, conditionally on measurement outcomes, in a time $t_{\mathrm{P}} \sim \exp(L)$, with L the number of qubits. In contrast, at large p, the measurements can distinguish different initial states efficiently. In this pure phase, an initially mixed state purifies quickly, often at an L-independent rate [99]. Furthermore, U(1)-symmetric monitored circuits exhibit a second

type of phase transition—a charge-sharpening transition [132] between a charge-fuzzy phase and a charge-sharp phase. In the charge-fuzzy phase, it takes much longer to learn the global charge from local measurements than in the charge-sharp phase. This is what distinguishes the two phases.

In this work, we explore monitored-random-circuit dynamics of one-dimensional qubit chains with SU(2) symmetry. Equivalently, the circuits conserve three noncommuting charges: the total spin angular momentum's components. Our main first result is the identification of a transition from a volume-law entangled phase to a critical phase. We have three pieces of evidence that support this result. First, we explore the purification dynamics of a spin chain initially entangled with an ancilla spin. We identify a purification transition between a mixed phase, in which the ancilla purifies over an exponential-in-L time, and a critical phase with scale-invariant purification and entanglement growth. Above a critical measurement rate (at $p > p_c$), we observe an extended-in-p critical phase in which the purification time scales diffusively: $t_P \sim L^2$. Second, we examine the entanglement dynamics undergone by an initially unentangled state. The purification transition doubles as an entanglement transition between volume-law entanglement scaling, at $p < p_c$, and subextensive (logarithmic or small-power-law) scaling, at $p > p_c$. The critical entanglement dynamics $p > p_c$—even in the measurement-only limit ($p = 1$)—due to the local measurements' noncommuting nature. Finally, we study the mutual information between sites on opposite ends of the chain. Since the chain has periodic boundary conditions, it is like a ring, so these qubits are $L/2$ sites apart. As one approaches a critical *point*, the mutual information begins to peak and drops back down as one passes the point. However, the mutual information will grow and stay large in the critical phase. We observe such behaviour.

Observing the purification/entanglement transition experimentally would require many instances of the same set of measurement outcomes. Such instances occur with vanishing likelihood in the thermodynamic limit. This challenge is the postselection problem. To evade this difficulty, we explore a "spin-sharpening/learnability" transition. Denote by s the total spin quantum number. We examine whether the dynamics collapse an initial superposition of states in different s sectors. Unlike in the U(1)-symmetric problem, the sectors generally cannot be shared by the (extensive) charges: our system's three charges, failing to commute, share only one sector. We identify a spin-sharpening transition at a measurement rate $p = p_\#$, which is numerically indistinguishable from the entanglement-transition rate: $p_\# \approx p_c$. In the "spin-sharp" phase ($p > p_\#$), an observer can, in principle, determine the system's s in a time scale $t \sim L^2$, with a probability tending to unity as $L \to \infty$. In contrast, in the "spin-fuzzy" phase ($p < p_\#$), the time scale is $t \sim L^3$. This "learning" perspective might be used to probe the transition experimentally.

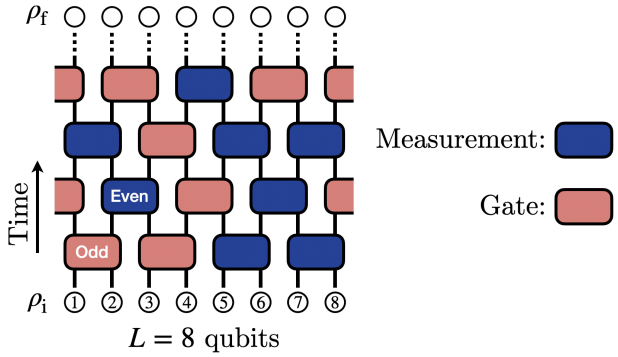

Figure 5.1: **SU(2)-symmetric monitored quantum circuits.** L qubits (circles) are prepared in the state ρ_i. Each "brick" in the brickwork circuit is an SU(2)-symmetric unitary gate with a probability $1-p$ and is a two-qubit projective measurement with a probability p. The circuit acts for some time (some number of layers) before the final state, ρ_f, is read out. One brick illustrates which bonds have even (odd) indices.

The rest of this paper is organized as follows. In Section 5.2, we introduce SU(2)-symmetric monitored quantum circuits. We present the numerics revealing the critical phase in Section 5.3 and the spin-sharpening transition in Section 5.4. Section 5.5 finishes with opportunities established by this work.

5.2 SU(2)-symmetric monitored circuits

Consider a brickwork circuit acting on a 1D chain of qubits, as depicted in Fig. 5.1. The number L of spins is even for convenience. Denote by $\sigma_j^{(x,y,z)}$ the Pauli matrices acting on qubit j. The total spin components $S^{(x,y,z)} = \frac{1}{2}\sum_{j=1}^{L}\sigma_j^{(x,y,z)}$ generate the algebra associated with a global SU(2) symmetry. We set $\hbar$ to 1. The spin-squared operator $\vec{S}^2$ has eigenvalues $s(s+1)$ labelled by the total spin quantum number s. We denote the eigenvalues of $S^{(z)}$ by m, the two-qubit singlet state by $|s_0\rangle$, and the two-qubit eigenvalue-m triplets by $|t_m\rangle$.

Each brick is, with a probability $1-p$, a gate, or, with a probability p, a projective measurement. The gates are chosen randomly from SU(2). The most general such gate acting on spins j and $j+1$, has the form[1]

$$\cos(\phi)\mathbb{1} - i\sin(\phi)\ \mathrm{SWAP}_{j,j+1}, \tag{5.1}$$

[1]This is found by solving for the unitary U which satisfies $\left[U, \sigma_j^{(\alpha)} + \sigma_{j+1}^{(\alpha)}\right] = 0 \forall \alpha$.

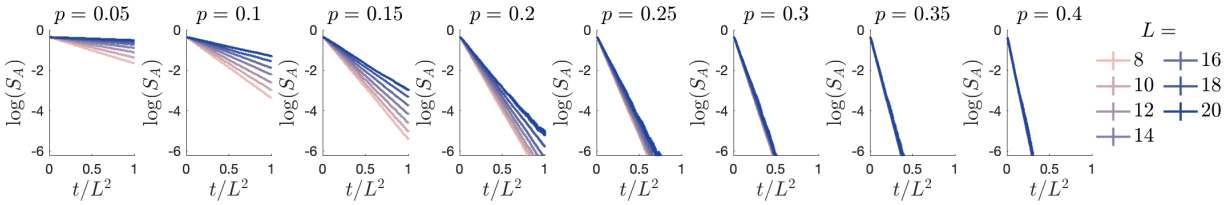

Figure 5.2: **The purification time reveals a z=2 phase.** The entropy S_A quantifies the ancilla qubit's entanglement with the system. We plot $\log(S_A)$ for clarity, as S_A decays exponentially. t/L^2 runs along the x-axis to demonstrate the existence of a phase in which the system purifies over a time scale $t_{\mathrm{P}} \sim L^2$. The curves' collapsing at $p > 0.35$ evidences this phase. We used 30 000 samples when $L = 8$ to 16; 10 000 samples when $L = 18$; and 1 500 samples when $L = 20$. The y-axis's lower limit is $\log(10^{-3}) \approx -6.91$. Additional numerics for $p = 0.6, 0.8$, and 1.0 are included in Appendix D.1.

up to an irrelevant overall phase.SWAP$_{j,k}$ swaps the states of the spins j and k. We draw each gate's parameter ϕ independently from the uniform distribution on $[0, 2\pi)$. Each measurement projects a two-qubit state onto the singlet ($s = 0$) or triplet ($s = 1$) subspace. Crucially, two measurements fail to commute when acting on overlapping spin pairs. One time step consists of a brick layer on even-index bonds and a layer on odd-index bonds. In the even-index-bond layers, a brick connects the first and L^{th} qubits, effecting periodic boundary conditions.

5.3 Critical phase

We present three pieces of evidence supporting the existence of a critical phase: first, a purification transition leading to scale-invariant behavior (Section 5.3.1); second, an entanglement transition from extensive to subextensive scaling (Section 5.3.2); and third, the growth of correlations with p (Section 5.3.3).

5.3.1 Purification time

We determine the purification time as follows [145]. Denote by $|s, m, \lambda_0\rangle$ and $|s, m, \lambda_1\rangle$ two orthogonal states from the same (s, m) sector. The last index distinguishes degenerate states. We entangle an ancilla qubit with the system's L qubits, forming the $(L+1)$-qubit state

$$|\tilde{\psi}_{\mathrm{i}}\rangle = \tfrac{1}{\sqrt{2}} \left(|0\rangle_A |s, m, \lambda_0\rangle + |1\rangle_A |s, m, \lambda_1\rangle \right). \tag{5.2}$$

The subscript A distinguishes the ancilla from the system qubits. A does not undergo gates or measurements.

We choose two system states that have $s = 1$ and $m = 0$. In $|s = 1, m = 0, \lambda_0\rangle$, qubits 1 and 2 are in the triplet $|\mathrm{t}_0\rangle$; and the remaining pairs of qubits, in singlets $|\mathrm{s}_0\rangle$. In $|s = 1, m = 0, \lambda_1\rangle$, qubits 3 and 4 are in $|\mathrm{t}_0\rangle$, instead. These two system states are orthogonal, in the same $\vec{S}^2$ sector, and in the same $S^{(z)}$ sector. However, one can distinguish the states by measuring qubits 1 and 2. Such local distinguishability is undesirable. Therefore, after preparing $|\tilde{\psi}_\mathrm{i}\rangle$, we scramble the system: the system undergoes a unitary-only ($p = 0$) SU(2)-symmetric circuit for L^2 time steps. (The t_P identified later in this subsection motivates the L^2.) The scrambling encodes quantum information about the ancilla roughly uniformly in many-body entanglement. This process prepares $|\psi_\mathrm{i}\rangle$.

$|\psi_\mathrm{i}\rangle$ undergoes $t = L^2$ time steps under monitored-random-circuit dynamics with $p \geq 0$. Denote by $\rho_A \coloneqq \mathrm{Tr}_{\bar{A}}(|\psi_\mathrm{f}\rangle\langle\psi_\mathrm{f}|)$ the final state of A. We calculate the final entanglement entropy between A and the system:

$$S_A \coloneqq S(\rho_A) \coloneqq -\mathrm{Tr}[\rho_A \log(\rho_A)]. \tag{5.3}$$

(All logarithms are base-e.) We anticipate that the measurements will purify the system at an exponential-in-t rate: $S_A \sim e^{-t/t_\mathrm{P}(L)}$. Therefore, we plot $\log(S_A)$ in Fig. 5.2. Along the x-axes runs t/L^2. At each $p > p_\mathrm{c} \approx 0.35$, the different-$L$ curves collapse. Hence this phase purifies according to $S_A \sim \mathrm{e}^{-t/L^2}$ and so has a dynamical critical exponent z=2. This z-value characterizes diffusive scaling [146] and suggestively evokes ferromagnetic spin waves' dynamics [147, Ch. 33]. At lower measurement rates, $p \ll p_\mathrm{c}$, we observe a mixed phase. Figure 5.3 shows the purification time plotted against L, at several p values. At $p = 0.05$, $t_\mathrm{P} \sim e^L$.

5.3.2 Entanglement dynamics

To characterize the critical phase further, we explore an initially pure state's late-time bipartite entanglement entropy, S_f. The purification transition manifests as a qualitative change in the L-dependence of S_f at $p = p_\mathrm{c}$.

We initialize the system in a short-range-entangled state $|\psi_\mathrm{i}\rangle$, a tensor product of a triplet $|\mathrm{t}_0\rangle$ and $\frac{L-2}{2}$ singlets $|\mathrm{s}_0\rangle$. This choice's details are unimportant. However, we choose this state so that $|\psi_\mathrm{i}\rangle$ is in the same s sector at all system sizes L. The state undergoes monitored-circuit dynamics for L^2 time steps. This time suffices for the entanglement entropy to reach a steady value, regardless of the measurement rate, p. Figure D.2 in

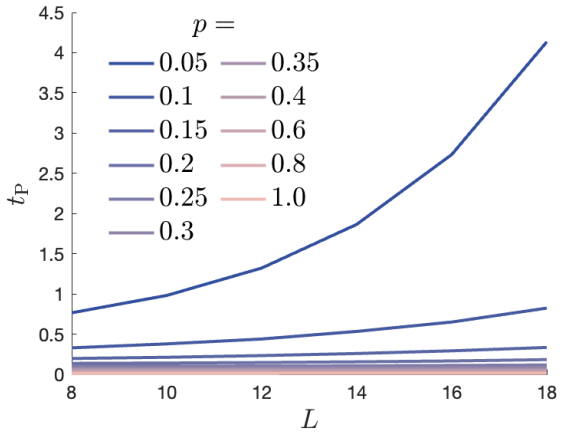

Figure 5.3: **Qualitative comparison of the purification time's growth with L at different p values.** For $p < p_c$, the purification time diverges rapidly with system size in a manner consistent with exponential.

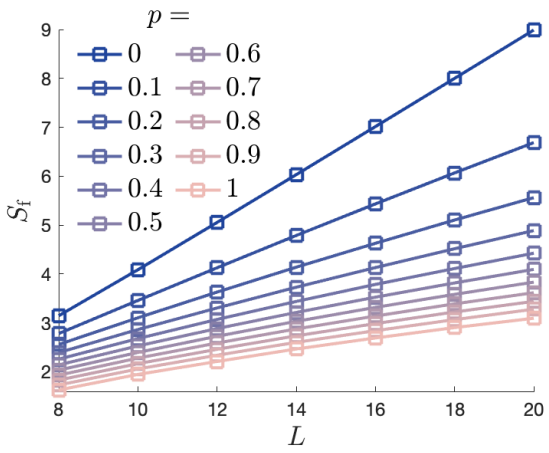

Figure 5.4: **The entanglement dynamics evidence no area-law phase.** The bipartite entanglement entropy reaches the long-time value S_{f}. At $p = 0$, S_{f} is linear in L. As p increases, S_{f} gradually becomes logarithmic or power-law with a small exponent. When $L = 10$ to 16, we use 30 000 samples; when $L = 18$ and 20, we use 10 000.

Appendix D.1 illustrates this point at the extreme values $p = 0, 1$. We measure the bipartite entanglement entropy, $S_{\rm f}$, between two equal-size halves of the chain.

Figure 5.4 shows the dependence of $S_{\rm f}$ on L at different measurement rates p. At $p = 0$, we observe the volume-law phase common to monitored circuits: $S_{\rm f} \sim L$. At larger p values,[2] the entanglement scaling is less consistent with a linear fit. Better fits are logarithmic and small-power-law ($S_{\rm f} \sim \sqrt{L}$). Figure 5.5 presents three fittings [L, $\log(L)$, and $\sqrt{L}$] at each of three measurement rates ($p = 0$, $p = 1$, and $p \approx p_{\rm c}$). At $p = 0.35 \approx p_{\rm c}$, it is unclear which fit is most accurate. However, the two nonlinear fits are visibly best. The $p = 1$ fits resemble the $p = 0.35$ ones. One cannot definitively distinguish these behaviors at the accessible system sizes.

A skeptic may say that the lack of area-law phase comes from the measurements being on pairs of sites and not from the non-Abelian symmetry. However, monitored quantum circuits with two-site measurements have been studied and do have an area-law [136].

5.3.3 Mutual information

We added to our characterization of the critical phase by studying mutual information. To introduce the mutual information, we consider a quantum system in a state $|\psi\rangle$. Let $\mathcal{A}$ and $\mathcal{B}$ denote subsystems. The reduced state of $\mathcal{A}$ is $\rho_{\mathcal{A}} \coloneqq {\rm tr}_{\bar{\mathcal{A}}}(|\psi\rangle\langle\psi|)$. The reduced states of $\mathcal{B}$ and $\mathcal{AB}$ are defined analogously. The mutual information between $\mathcal{A}$ and $\mathcal{B}$ is

$$I(\mathcal{A} : \mathcal{B}) \coloneqq S(\rho_{\mathcal{A}}) + S(\rho_{\mathcal{B}}) - S(\rho_{\mathcal{AB}}). \tag{5.4}$$

The mutual information upper-bounds equal-time correlators between local operators acting nontrivially on A alone and on B alone [148]. We denote by $I^{(1)}_{j,k}$ the mutual information between sites j and k.

We denote by $I^{(2)}_{j,k}$ the mutual information between the pair $(j, j+1)$ and the pair $(k, k+1)$. If p is a critcal point, we expect the mutual information versus to grow as it approaches p, peak, and then rapidly decrease. However, as we see in Fig. 5.6a, the mutual information continues to grow with p. This reinforces our result that the system is in a critical phase.

$I^{(2)}_{j,k}$ decays with the distance $|j - k|$ at all $p > 0$. For particular sites j and k, $I^{(2)}_{j,k}$ may depend on p nonmonotonically. However, the asymptotic decay rate monotonically

[2] According to [144], the entanglement phase transition is equivalent to the purification transition. Our system's purification transition happens at $p_{\rm c} \approx 0.35$, according to the previous subsection. This section's numerics are consistent with an entanglement transition at $p \approx 0.35$, since the transition's exact location is somewhere slightly above $p = 0.25$.

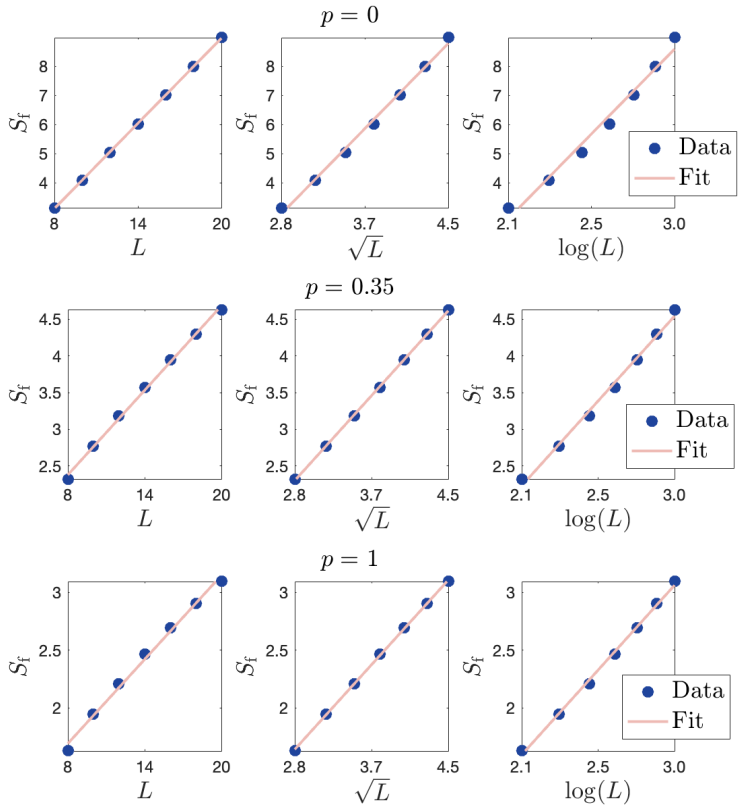

Figure 5.5: **Long-time bipartite entanglement entropy vs. system size.** At $p = 0$, $S_\mathrm{f} \sim L$, signaling a volume law. At $p = 1$, the entropy scales logarithmically or as a small power law: $S_\mathrm{f} \sim \log(L)$, or $S_\mathrm{f} \sim \sqrt{L}$.

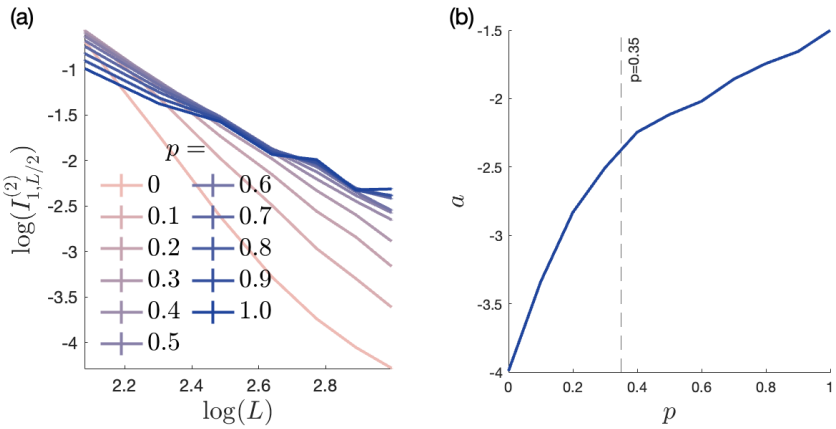

Figure 5.6: **Mutual information at antipodal sites.** We call sites 1 and $L/2$ antipodal. (a) $\log\left(I^{(2)}_{1,L/2}\right)$ is plotted against $\log(L)$ at several L values. Using the fit function $\log\left(I^{(2)}_{1,L/2}\right) = a\log(L) + b$, we identify the critical exponent a in $I^{(2)}_{1,L/2} \sim L^a$. (b) Plotting a against p, we find that $I^{(2)}_{1,L/2}$ decays as a power law in both phases, where a seems to be drifting.

decreases as p decreases. To explore this decay rate, we examine the mutual information between antipodal pairs of sites: $I^{(2)}_{1,L/2}$ (Fig. 5.6a). Given the limitations on system size, we cannot convincingly determine the asymptotic decay's functional form. A power-law decay fits the data reasonably well (Fig. 5.6b). The fitted power a gradually decreases with p. Furthermore, a changes qualitatively around $p_c = 0.35$—from changing quickly with p, at $p < p_c$, to drifting slowly near -2, at $p > p_c$. Given the small range of system sizes available, exponential decay fits the data reasonably well, too; we cannot rule out this behavior. Yet, given the other critical scaling behavior at $p > p_c$, we expect that power-law decay to be more natural in this regime. The data also prohibit confident distinction between (i) one power at $p > p_c$, with drifts in the fitted exponent, due to finite-size corrections, and (ii) continuously evolving power laws (as would arise in, say, a Luttinger liquid).

5.4 Spin-sharpening transition

Having explored the purification dynamics within an s sector, we explore the purification of a superposition spread across s sectors. We again entangle the chain with an

ancilla qubit. This time, the ancilla is in $|0\rangle$, and the chain has a spin quantum number s_0, in superposition with the ancilla's being in $|1\rangle$ and the chain's having s_1. The dynamics may purify the ancilla in a given measurement trajectory. In this case, the chain's state has collapsed onto the s_0 (or s_1) sector. Consequently, the measurement outcomes' probability of being compatible with the system's having s_1 (or s_0) vanishes. An observer with knowledge of the circuit can learn the spin quantum number by monitoring measurement outcomes (though doing so may require the ability to classically simulate the circuit with post-selected measurement outcomes). To be clear, the circuit looks exactly like the one in Fig. 5.1 but with a different initial state. The initial state consists of $L+1$ qubits, L of which evolve as shown in Fig. 5.1 and 1, which is untouched until the end of the circuit. At the end, the ancilla's entanglement entropy is measured.

Comparing spin sharpening with U(1)-charge sharpening is illuminating. One can estimate as follows the total charge of qubits undergoing a U(1)-symmetric hybrid circuit: running the circuit, one obtains ptL measurement outcomes (0s and 1s), on average. Consider averaging the outcomes, multiplying by L, and rounding to the nearest integer. If $t \sim L$, this procedure estimates the charge accurately [149]. If the dynamics are SU(2)-symmetric on average (as in Section 5.2), sequential measurements fail to commute. Hence later measurements render partially irrelevant the information obtained from earlier measurements. An observer cannot obviously learn s ever. Nevertheless, we numerically identify a measurement-induced transition at a measurement rate $p_\#$. We call this transition a spin-sharpening transition. It separates regimes in which an observer can ($p > p_\#$) and cannot ($p < p_\#$) identify s from the measurement outcomes, with a probability tending to unity as the $L \to \infty$.

We diagnose the spin-sharpening transition using a similar procedure to the one in Section 5.3.1. The difference is that, unlike in Eq. (5.2), we construct $|\tilde{\psi}_{\rm i}\rangle$ from distinct $\vec{S}^2$ eigenspaces:

$$|\tilde{\psi}_{\rm i}\rangle = \tfrac{1}{\sqrt{2}} \left(|0\rangle_A |s_0, m, \lambda_0\rangle + |1\rangle_A |s_1, m, \lambda_1\rangle \right). \tag{5.5}$$

We choose $m = 0$, $s_0 = 1$, and $s_1 = 0$ for convenience: one can construct such a $|\tilde{\psi}_{\rm i}\rangle$ by tensoring together singlets and an $m = 0$ triplet, regardless of L. After preparing $|\tilde{\psi}_{\rm i}\rangle$, we scramble the system under a p=0 circuit for L^2 time steps, as in Section 5.3.1. This procedure prepares a state $|\psi_{\rm i}\rangle$. Then, we evolve the system under monitored-circuit dynamics with a fixed p. Anticipating z=2 dynamical scaling in the spin-sharp phase, we evolve the system for L^2 time steps. If the ancilla purifies after this short time, we say that the spin has sharpened. We denote the final state by $|\psi_{\rm f}\rangle$.

Figure 5.7a shows the ancilla's final entanglement entropy, S_A, plotted against p. Different curves correspond to different system sizes L. The curves cross at $p_\# \approx 0.28$, suggesting

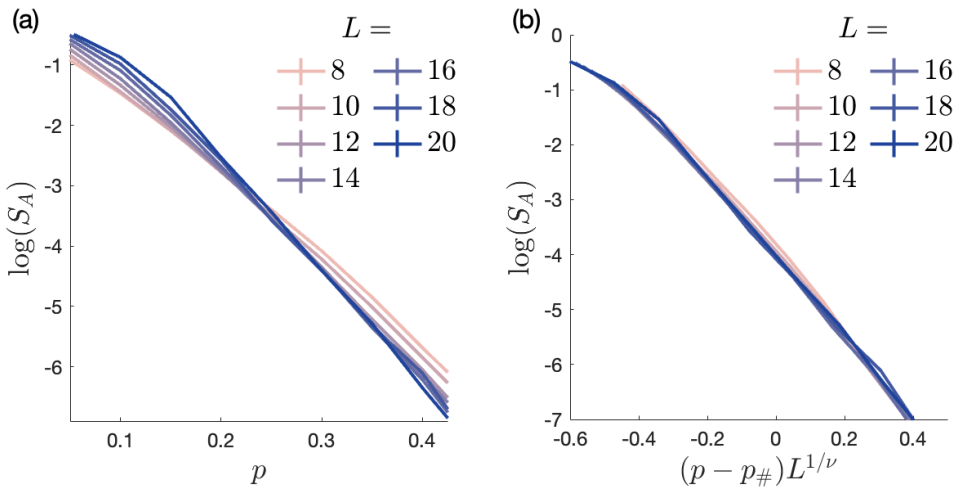

Figure 5.7: **Evidence of spin-sharpening transition.** The entropy S_A quantifies the ancilla qubit's entanglement with the system. Different curves correspond to different system sizes L. (a) The curves' crossing at $p \approx 0.28$ indicates a phase transition. (b) We identify a finite-size collapse using $\nu = 3.0$ and $p_\# = 0.28$.

that a spin-sharpening transition occurs at $p_\#$. Furthermore, Fig. 5.7b displays a finite-size collapse. We used the scaling form $\log(S_A) = (p - p_\#)L^{1/\nu}$, the correlation-length exponent $\nu = 3.0$, and $p_\# = 0.28$. Using $\nu = 3.0$, we observe a suitable collapse. ν values within ± 1.2 of 3.0 yield reasonable collapses, too.

Figure 5.8 reveals the phases' spin-sharpening time scales: $\sim L^2$ in the spin-sharp phase and $\sim L^3$ in the spin-fuzzy phase. A simple argument supports the latter [150]: $|\psi_{\mathrm{i}}\rangle$ corresponds to an eigenvalue $s(s+1) \in \{1, 2\}$ of $\vec{S}^2 = \sum_{j,k} \vec{\sigma}_j \cdot \vec{\sigma}_k$. The system contains $\sim L^2$ pairs (j, k). One might expect all pairs to contribute roughly equally to $\langle \vec{S}^2 \rangle$, by ergodicity, in the spin-fuzzy phase. Hence $\langle \vec{\sigma}_j \cdot \vec{\sigma}_k \rangle \sim s(s+1)/L^2$. To identify $s(s+1)$, we therefore must measure L^2 correlators $\langle \vec{\sigma}_j \cdot \vec{\sigma}_k \rangle$. Measuring one correlator with an imprecision $\sim 1/L$ requires $\sim L^2$ measurements. We hence need $\sim L^4$ measurements total. Since (const.)L measurements occur per time step, the spin should sharpen in a time $\sim L^3$.

Our identification of a spin-sharpening transition at $p_\#$ is subject to at least two caveats. First, the crossing point drifts to larger p as L increases (perhaps coalescing with the purification transition at p_c as $L \to \infty$). Second, the scaling ansatz we chose for the data collapse in Fig. 5.7b may not be valid. The ansatz implies that the time scale for a size-L system to sharpen increases more quickly than L^2 for $p < p_\#$ and more slowly than L^2 for $p > p_\#$. However, our data for $p > p_\#$ (see Fig. D.3 in Appendix D.1) is compatible with a

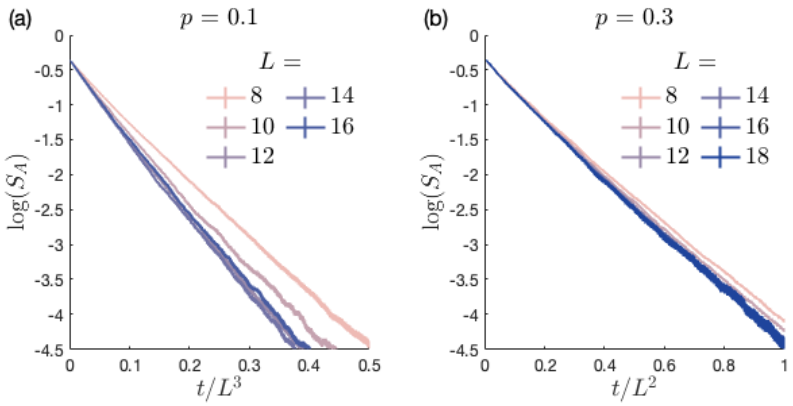

Figure 5.8: **The spin-sharpening time scale is $\sim L^3$ in the fuzzy phase and $\sim L^2$ in the sharp phase.** The entropy S_A quantifies the ancilla qubit's entanglement with the system. Different curves correspond to different system sizes L. (a) t/L^3 runs along the x-axis to demonstrate that the spin can sharpen over a time scale $\sim L^3$. This time scale characterizes the spin-fuzzy phase ($p < p_\#$). Simulating an L=18 circuit over L^3 time steps is not computationally feasible. Thus no $L = 18$ curve is present. (b) t/L^2 runs along the x-axis to demonstrate that the spin can sharpen over a time scale $\sim L^2$. This time scale characterizes the spin-sharp phase ($p > p_\#$). We used 30 000 samples when $L = 8$ to 16; and 10 000 samples when $L = 18$.

sharpening time scale $\sim L^2$ deep in the critical phase. If the sharpening time indeed scales as L^2 throughout the critical phase, the crossing in Fig. 5.7a must be a finite-size artifact. Precisely identifying $p_\#$ and the sharpening transition's nature is outside the scope of this work, due to the paucity of L values accessible in exact computations. We defer a detailed analysis of the spin-sharpening time scales to future work.

Finally, the spin-sharpening transition suggests a means of observing a measurement-induced transition experimentally that mitigates the postselection-problem [149, 151, 152, 153]: identify whether an observer can learn s from measurement outcomes in a given time interval. This learning would require "decoders" for estimating s from the outcomes. The decoders' accuracy, as a function of the measurement rate, would need to be tested. In principle, one can learn s most accurately via brute-force decoding [149]. One would, upon running the circuit and obtaining the measurement outcomes, simulate the circuit, postselected on the observed outcomes and operating on a state in the s_0 sector. Next, the simulation would be repeated with an initial state in the s_1 sector. From each simulation, the probability that s_0 (or s_1) had engendered the observed outcomes could be inferred.

However, this approach generically costs exponential-in-L time (even if a quantum computer performs the simulation, due to the postselection). Special classes of monitored dynamics [149, 151, 152, 153] may allow for approximate decoders that can be implemented efficiently on classical or quantum computers without postselection. In this case, the transition's nature will depend on both the circuit and the decoder and may differ, in location or universality class, from the spin-sharpening transition observed under optimal decoding. We leave for future work the problem of designing efficient decoders for spin-sharpening transitions.

5.5 Summary & Outlook

We studied the dynamics of monitored random circuits with SU(2) symmetry, i.e., with three noncommuting charges: the total spin angular momentum's components. First, we numerically discovered a purification transition between a mixed phase (at $p < p_c \approx 0.35$) and a critical phase (at $p > p_c$). In the critical phase, the purification time scales as $t_P \sim L^2$. The purification transition doubles as an entanglement transition, which separates volume-law (at $p < p_c$) and subextensive (logarithmic or small-power-law, at $p > p_c$) entanglement scalings. Even in the measurement-only limit (at $p = 1$), the symmetry's non-Abelian nature enables nontrivial entanglement scaling. Furthermore, we found the systems mutual information continues to grow past p_c. All of this together is clear evidence of a critical phase.

Additionally, we observed a spin-sharpening transition across which there is a parametric change in the time at which one can (in principle) learn the system's total spin by monitoring measurements. The time scale is $t \sim L^2$ in the "spin-sharp" phase and $t \sim L^3$ in the "spin-fuzzy" phase.

Our results open opportunities for future work. One is to understand the purification/entanglement and sharpening transitions analytically. Second, our system offers a playground for numerically exploring the recent result that non-Abelian symmetries constrain local unitary circuits more than Abelian symmetries do and so may constrain chaos more [59, 60, 61, 62]. Third, efficient classical and quantum spin-sharpening decoders merit exploration. Finally, consider again the postselection problem. Measuring the final state of the qubits will always require multiple runs of the experiment. However, to observe a measurement-induced phase transition, one also requires that the measurement outcomes be the same in multiple runs. The likelihood of this happening is exponentially small in the number of measurements. This is the postselection problem. However, one might leverage spin sharpening to avoid this problem (Section 5.1). This is because the spin sharpening tradition seems to coincide with the entanglement transition in the SU(2) case. Thus, one can distinguish the two phases by asking—How efficiently could the experimenter, in one trial, determine the global charge from local measurement? The thermodynamics of noncommuting charges have already been observed experimentally with trapped ions [46]. Superconducting qubits, quantum dots, and spinful fermionic atoms are natural candidates, too [45, 2].

Chapter 6

Noncommuting charges remove non-thermalizing local observables

This chapter is based on reference [5] and overlaps with its text.

6.1 Introduction

Since publishing the previous chapter of my thesis, the conceptual puzzle we highlighted–noncommuting charges seem to promote and hinder thermalization simultaneously–has become a topic of broad interest [47, 55, 154, 155, 156, 157, 158, 159, 160]. This paradox serves as the driving force for this final chapter. While prior studies have indirectly suggested a dual role for noncommuting charges in thermalization, this chapter intends to confront the question more directly.

What would it mean for noncommuting charges to hinder thermalization? Quantum systems thermalize according to the ETH (Section 2.3), i.e., by having the expectation value of local observables $\langle O_i(t)\rangle$ stop changing in time and settle on the thermal expectation value. We posit then that if noncommuting charges hinder thermalization, they must stop such a process from occurring —i.e., they must lead to $\langle O_i(t)\rangle$ experiencing non-thermalizing dynamics. Thus, to help resolve this puzzle, we connect noncommuting charges and conditions that lead to violations of the ETH. Buča et al. [161] proposed a set of conditions wherein if an operator A satisfies $[H, A] = \lambda A$ with $\lambda \in \mathbb{R}$ and $\lambda \neq 0$, then any local operator $\mathcal{O}_i$ overlapping with A (i.e., $\mathrm{tr}[\mathcal{O}_i A] \neq 0$) will not thermalize, displaying non-thermalizing dynamics in violation of the ETH [161]. These operators, A,

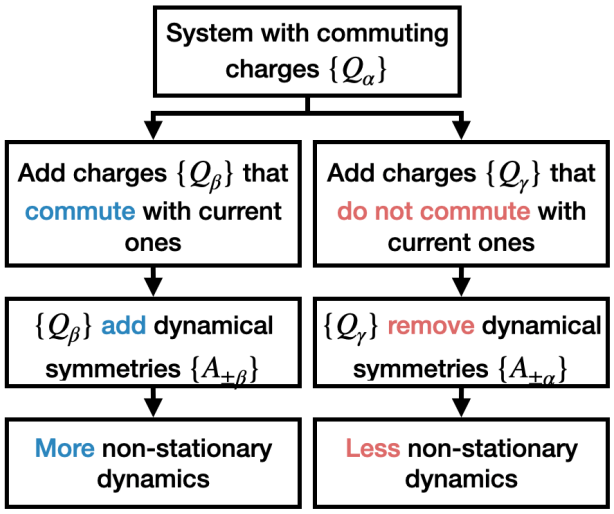

Figure 6.1: **Introducing charges into systems with existing dynamical symmetries.** A system with commuting charges $\{Q_\alpha\}$ possesses paired dynamical symmetries $\{A_{\pm\alpha}\}$. Modifying the system's Hamiltonian to conserve noncommuting charges $\{Q_\beta\}$ relative to $\{Q_\alpha\}$ will result in the loss of some or all dynamical symmetries $\{A_{\pm\alpha}\}$. Conversely, a different modification that introduces new commuting charges will bring associated dynamical symmetries. These new charges have no algebraic relationship with the initial charges, suggesting an increase in the system's dynamical symmetries.

are referred to as dynamical symmetries' [161, 162, 163, 164] or spectrum generating algebras' [165].[1] Dynamical symmetries represent a departure from the conventional definition of 'symmetry' as an invariance under a transformation. Therefore, Noether's theorem does not directly establish the link between dynamical symmetries and charges. These symmetries prevent a quantum many-body system from reaching a stationary state, affecting both open [161, 168, 169] and closed [162] quantum systems. Dynamical symmetries can be responsible for the non-thermalizing dynamics observed in systems such as quantum time crystals [162], OTO crystals [170], and quantum attractors [171].

Our first result is a correlation between charges and dynamical symmetries. We establish that a corresponding charge exists for each pair of dynamical symmetries, and we detail the method for deriving this charge from the dynamical symmetries. Additionally, we confirm that this reciprocal relationship extends to a wide range of charges and Hamiltonians. This correlation illustrates that even a single charge can cause a violation of the

[1]The terms 'dynamical symmetry' and 'spectrum generating algebra' encompass a range of related concepts [166, 167]. In this paper, we specifically refer to the condition previously stated.

ETH. Using this framework, we show that introducing a new charge to a system can enhance or disrupt its non-thermalizing dynamics. Specifically, if the new charge commutes with the existing ones, it will preserve the current dynamical symmetries and introduce new ones. Conversely, if the new charge does not commute, it will reduce the number of dynamical symmetries. Figure 6.1 encapsulates these findings. Our analyses reveal a fundamental tension between noncommuting charges and dynamical symmetries and highlight that introducing additional conservation laws can drive a system toward thermalization.

Dynamical symmetries are also linked to quantum scars, a class of eigenstates that do not thermalize [172, 173, 174, 175]. Ref.[176] describes creating Hamiltonians with quantum scars by altering a non-Abelian symmetric Hamiltonian with a dynamical symmetry-based term. Our research contrasts this by examining how noncommuting and commuting charges affect various systems' dynamical symmetries and establishing a related correspondence. Unlike the quantum scar focus, our analysis targets local observables and can naturally extend beyond Hamiltonians to Lindbladians since noncommuting charges and dynamical symmetries are relevant in both closed and open systems [65, 161, 168, 169]. Future connections are explored in the Outlook (Chapter 7).

The rest of this chapter is structured as follows: Section 6.2 reviews the ETH, dynamical symmetries, and noncommuting charges. Section 6.3 introduces our first main result, detailing the correspondence between dynamical symmetries and charges. Section 6.4 discusses our second result, which shows how introducing a new charge to a system affects its non-thermalizing dynamics, contingent on the commutation with existing charges, illustrated through various examples. We summarize our results in 6.5.

6.2 Dynamical symmetries

We previously introduced the ETH in Section 2.3. Systems with dynamical symmetries violate the ETH [161, 163]. Dynamical symmetries can, for example, lead Heisenberg XXZ spin-chains to behave as quantum time crystals [162] and spin lace systems to behave as quantum many-body attractors [171]. We denote a dynamical symmetry by a non-Hermitian operator A, such that

$$[H, A] = \lambda A, \tag{6.1}$$

where λ is a real and non-zero constant. We assume that A is extensive, by restricting it to have the form $A = \sum_{j=1}^{N} \tilde{A}^{(j)}$, where $\tilde{A}^{(j)}$ is an operator that acts non-trivially on 1 site and as the identity on all other sites. Furthermore, for every dynamical symmetry A, there exists another $A^\dagger$, $\left[H, A^\dagger\right] = -\lambda A^\dagger$. Thus, dynamical symmetries always come in

pairs. A system can have multiple pairs of dynamical symmetries. In that case, we add subscripts as follows $[H, A_\beta] = \lambda_\beta A_\beta$. Furthermore, we define $A_{+\beta} := A_\beta$ and $A_{-\beta} := A_\beta^\dagger$. The expectation value of an observable $\mathcal{O}$ that overlaps with one dynamical symmetry, $\mathrm{tr}[A\mathcal{O}] \neq 0$, will continue to change over time.

6.3 Correspondence between charges and dynamical symmetries

In this section, we present a correspondence between the existence of charges and dynamical symmetries. This correspondence is in the form of two theorems. One theorem identifies a charge from pairs of dynamical symmetries. The other theorem identifies a pair of dynamical symmetries from charges. We first prove this correspondence (Section 6.3.1) before illustrating it using the Hubbard model (Section 6.3.2).

6.3.1 Correspondence

We introduced the necessary background in Lie Algebra theory in Section 3.2.2. As outlined there, we denote by $\mathfrak{g}$ a finite-dimensional semisimple complex Lie algebra. From this point onward, we denote by $\mathfrak{h}$ a Cartan subalgebra of a $\mathfrak{g}$. Furthermore, for this chapter, we use the notation $X_{\pm\beta}$ to denote the root vectors. This chapter's results apply to all sets of charges $\{Q_\alpha\}$ that can be partitioned into subsets such that each subset generates a $\mathfrak{g}$ or a $\mathfrak{h}$. Note that this includes all sets $\{Q_\alpha\}$ that generate a $\mathfrak{g}$ and all sets $\{Q_\alpha\}$ that generate a $\mathfrak{h}$, even if they may not generate a full $\mathfrak{g}$. This is a wide class that includes, for example, everything in the Standard Model of physics and the charges of the Hubbard, Ising, and Heisenberg models.

We highlight additional features of root vectors which are important to this work. For all root vectors $[X_{+\beta}, X_{-\beta}] \in \mathfrak{h}$ (Proposition 7.17 of Ref. [177]). $X_{\pm\beta}$ can always be chosen such that $X_{+\beta} = X_{-\beta}^\dagger$ (p. 273 of Ref. [178]). It follows then that

$$([X_\beta, X_{-\beta}])^\dagger = [X_\beta, X_{-\beta}] \tag{6.2}$$

and that

$$[X_{+\beta}, [\mathcal{H}, X_{-\beta}]] = ([X_{-\beta}, [\mathcal{H}, X_{+\beta}]])^\dagger \tag{6.3}$$

where $\mathcal{H}$ is any Hermitian operator.

Theorem 2. *For every pair of dynamical symmetries $A_{\pm\beta}$ that a Hamiltonian has, there exists a charge $Q_\beta = [A_{+\beta}, A_{-\beta}]$.*

Proof. For Q_β to be a charge, it must be conserved by the Hamiltonian, a Hermitian operator, and extensive. Using the Jacobi identity, Eq. (6.2), and Eq. (6.3), we find that

$$[H, [A_{+\beta}, A_{-\beta}]] = [A_{+\beta}, [H, A_{-\beta}]] - [A_{-\beta}, [H, A_{+\beta}]] \tag{6.4}$$
$$= -\lambda_\beta \left([A_{+\beta}, A_{-\beta}] + [A_{-\beta}, A_{+\beta}]\right) \tag{6.5}$$
$$= 0. \tag{6.6}$$

Thus, the Hamiltonian conserves Q_β. For Q_β to be a charge, it must also be Hermitian, which it is

$$Q_\beta^\dagger = \left(A_\beta A_\beta^\dagger - A_\beta^\dagger A_\beta\right)^\dagger \tag{6.7}$$
$$= \left(A_\beta A_\beta^\dagger - A_\beta^\dagger A_\beta\right) = Q_\beta. \tag{6.8}$$

Finally, recall that we are studying dynamical symmetries, which are $k = 1$ local, meaning they are sums over operators acting on single sites of the lattice. Thus, all $Q_\beta = [A_{+\beta}, A_{-\beta}]$ will also be 1-local and are charges by our definition. □

We say a set of dynamical symmetries 'produces' a set of charges $\{Q_\beta\}$ when the span of $\{Q_\beta\}$ equals the span of the set of charges found using Theorem 2.

Theorem 3. *For every set of charges $\{Q_\alpha\}$ that form a $\mathfrak{h}$ of $\mathfrak{g}$, there exists a Hamiltonian H conserving those charges such that the root vectors that complete the Lie algebra are dynamical symmetries of H.*

Proof. Consider a Hamiltonian of the form $H = H_\mathfrak{g} + \sum_\alpha c_\alpha Q_\alpha$, where $H_\mathfrak{g}$ is a Hamiltonian that commutes with all charges that generate $\mathfrak{g}$ and c_α are constants. The charges that generate $\mathfrak{g}$ form a basis for the algebra [2]. Since the root vectors can be written in this basis, $[H_\mathfrak{g}, X_{\pm\beta}] = 0$. For any charge and root vector $[Q_\alpha, X_{\pm\beta}] = \beta(\alpha) X_{\pm\beta}$. It follows then that $X_{\pm\beta}$ are dynamical symmetries:

$$[H, X_{\pm\beta}] = \sum_\alpha c_\alpha [Q_\alpha, X_{\pm\beta}] = \Big(\sum_\alpha c_\alpha \beta(\alpha)\Big) X_{\pm\beta}. \tag{6.9}$$

□

We say a set of charges 'produces' a set of dynamical symmetries $\{A_{\pm\beta}\}$, when $\{A_{\pm\beta}\}$ equals one set of dynamical symmetries that can be found using Theorem 3.

Theorem 3 is for a set of charges that form a $\mathfrak{h}$ of $\mathfrak{g}$. Any set of charges that generate a $\mathfrak{g}$ can be partitioned into $\frac{c}{r}$ sets of mutually commuting charges [2], where c is the dimension of the algebra and r is the rank. Thus, through the repeated application of Thm. 3, this theorem can be used to study charges that generate $\mathfrak{g}$.

6.3.2 Illustration using the Hubbard model

A simple setting to illustrate this correspondence is the Hubbard model. We choose this model for various reasons. First, it has been shown to demonstrate non-thermalizing behaviour emerging from dynamical symmetries and the forms of the charges and dynamical symmetries are known [161]. Additionally, its two commuting charges form separate $\mathfrak{h}$'s, illustrating the effect commuting charges have on dynamical symmetries. Finally, it is a physically important model—the prototypical model of strongly correlated materials.

Consider a chain of N fermions. Denote by $c_\sigma^{(j)\dagger}$ and $c_\sigma^{(j)}$ the creation and annihilation operators for a fermion of spin σ at lattice site j, $\sigma \in \{\uparrow, \downarrow\}$. Denote by $n_\sigma^{(j)} := c_\sigma^{(j)\dagger} c_\sigma^{(j)}$ the number operator for fermions of spin σ at lattice site j. The 1D Hubbard model's Hamiltonian can be written as [179]

$$H = \sum_{j=1}^{N-1} \sum_{\sigma=\uparrow,\downarrow} -t \left(c_\sigma^{(j)\dagger} c_\sigma^{(j+1)} + c_\sigma^{(j+1)\dagger} c_\sigma^{(j)} \right) + U n_\uparrow^{(j)} n_\downarrow^{(j)} - \mu \left(n_\uparrow^{(j)} + n_\downarrow^{(j)} \right) + \frac{B}{2} \left(n_\uparrow^{(j)} - n_\downarrow^{(j)} \right), \tag{6.10}$$

where t is the hopping amplitude, U is the on-site Coulomb interaction, μ is the chemical potential, and B is the strength of a constant external magnetic field. The first term is proportional to the kinetic energy of electrons hopping between neighbouring sites. The second term describes the Coulomb repulsion between two electrons on the same site. The third term adjusts the total number of electrons in the system. The fourth term splits the energy levels of the up-spin and down-spin electrons.

The Hubbard model has two pairs of dynamical symmetries [161]. The first pair are

$$S_{+z}^{\text{tot}} = \sum_{j=1}^{L} c_\uparrow^{(j)\dagger} c_\downarrow^{(j)} \quad \text{and} \quad S_{-z}^{\text{tot}} = \sum_{j=1}^{L} c_\downarrow^{(j)\dagger} c_\uparrow^{(j)}, \tag{6.11}$$

and the second pair are

$$\eta^{\text{tot}}_{+z} = \sum_{j=1}^{N} (-1)^j c^{(j)\dagger}_{\uparrow} c^{(j)\dagger}_{\downarrow} \quad \text{and} \quad \eta^{\text{tot}}_{-z} = \sum_{j=1}^{L} (-1)^j c^{(j)}_{\downarrow} c^{(j)}_{\uparrow}. \tag{6.12}$$

Using theorem 2, we identify two charges:

$$\left[S^{\text{tot}}_{+z}, S^{\text{tot}}_{-z}\right] = S^{\text{tot}}_{z} = \sum_{j=1}^{L} \left(n^{(j)}_{\uparrow} - n^{(j)}_{\downarrow}\right), \text{ and} \tag{6.13}$$

$$\left[\eta^{\text{tot}}_{+z}, \eta^{\text{tot}}_{-z}\right] = \eta^{\text{tot}}_{z} = \sum_{j=1}^{L} (n^{(j)}_{\uparrow} + n^{(j)}_{\downarrow} - 1). \tag{6.14}$$

These charges are the two known charges of the system. S^{tot}_z is the total spin along the z-axis and η^{tot}_z is a component of the pseduo-spin [180]. The pseudo-spin symmetry reflects the symmetry of the Hubbard model with respect to η-pairing states. η-pairing states are many-body states where electrons pair up with opposite spins and opposite momenta. The conservation of pseudo-spin quantities suggests that the Hubbard model possesses an inherent symmetry that protects these paired states, making them stable and energetically favourable under certain conditions.

Starting from the charges, we can also identify the dynamical symmetries using theorem 3. When $B = 0$ and $\mu = 0$, the Hubbard Hamiltonian contains two sets of charges that generate $\mathfrak{su}(2)$ [181]. For $B \neq 0$ and $\mu \neq 0$, the Hubbard model has two sets of charges that generate Cartan subalgebras of $\mathfrak{su}(2)$. Each charge, S^{tot}_z and η^{tot}_z, is an element in one of these algebras. We can use these Cartan subalgebras to complete a Cartan-Weyl basis for $\mathfrak{su}(2)$. Doing so, we find two sets of generators $\{S^{\text{tot}}_z, S^{\text{tot}}_{+z}, S^{\text{tot}}_{-z}\}$ and $\{\eta^{\text{tot}}_z, \eta^{\text{tot}}_{+z}, \eta^{\text{tot}}_{-z}\}$. This demonstrates how Cartan-Weyl bases can be used to identify the dynamical symmetries from the charges.

6.4 Noncommuting charges' effect on dynamical symmetries

In this section, we consider the following setting. We begin with a system that has a set of charges $\{Q_\alpha\}$ that, according to theorem 3, produce dynamical symmetries $\{A_{\pm\alpha'}\}$. This system experiences non-thermalizing dynamics in all observables $\mathcal{O}$ that overlap with

any elements in $\{A_{\pm\alpha'}\}$. We then introduce one or more charges into the system. This introduction of charge(s) can either add to or disrupt its existing non-thermalizing dynamics. The Hubbard model illustrates that in systems with commuting charges, the dynamical symmetries of each charge can coexist. This section will present another example with commuting charges and two examples with noncommuting charges. A summary of this section's results is presented in Fig. 6.1.

First, to be mathematically rigorous, we formalize our procedure for introducing charges in Section 6.4.1. Our procedure highlights why there is a difference in the commuting and noncommuting charge cases. In Section 6.4.2, we illustrate this procedure using charges that generates a Cartan subalgebra of $\mathfrak{su}(2)$ and to charges that generate $\mathfrak{su}(2)$. We do the same analysis in Section 6.4.3 for the $\mathfrak{su}(3)$ algebra. These sections further demonstrate the difference in introducing commuting and noncommuting charges. We conclude by presenting Hamiltonians in Section 6.4.4 that can be used to explore the distinction between commuting and noncommuting charges. This connection links our findings with experimental tests and related research on quantum scars.

6.4.1 Procedure

Consider a system with a set of charges $\{Q_\alpha\}$ that can be partitioned into subsets such that each subset generates a $\mathfrak{h}$ or a $\mathfrak{g}$. In the earlier Hubbard model example, we had two subsets that each generate a $\mathfrak{h}$ (S_z^{tot} and η_z^{tot}). We want a procedure to identify a system's dynamical symmetries from these charges. Below is a procedure for doing so for one of the subsets.

1. Partition the system's charges into $\frac{n}{r}$ sets of mutually commuting charges, where n is the number of generators in a basis for $\mathfrak{h}$ or $\mathfrak{g}$.
2. Select any one of $\mathfrak{h}$'s identified in step 1.
3. Construct a Cartan-Weyl basis by adding to $\mathfrak{h}$ $\frac{c-r}{2}$ pairs of root vectors, $X_{\pm\beta}$.
4. According to Theorem 3, these pairs of root vectors are dynamical symmetries. We add them to our list of the system's potential dynamical symmetries, $A_{\pm\beta} := X_{\pm\beta}$. The values of λ_β can be determined in two ways. One is that they are equal to the roots of $\mathfrak{g}$ relative to $\mathfrak{h}$ for a given charge $Q'_\alpha \in \mathfrak{h}'$. Thus, one can solve for $\beta(h)$ and set λ_β equal to that. Alternatively, one can explicitly solve for $[H, A_\beta] = \lambda_\beta A_\beta$. The specific $\mathfrak{g}$ will determine which is simpler to do.

5. Select a different one of the sets of charges identified in step 1, if one exists. Verify whether including the new charges removes any of the dynamical symmetries found earlier.

6. Repeat steps 3 to 5 until no further Cartan subalgebras remain.

One can then repeat this procedure for different $\mathfrak{h}$ or a $\mathfrak{g}$.

The procedure can naturally be reversed using Theorem 2, where one identifies a charge from each pair of dynamical symmetries. The reverse procedure uses $\frac{c}{r}(c-r)$ dynamical symmetries to identify $\frac{c}{2r}(c-r)$ charges. This is because the charges identified in the reverse procedure are generally not linearly independent. The linear independence of charges Q_α generating a Lie algebra $\mathfrak{g}$ can be assessed by computing the Killing forms between all pairs of Q_α. The Killing form, introduction in Sec. 3.2.2 is

$$(x, y) := \mathrm{tr}(\mathrm{ad}x \cdot \mathrm{ad}y) \tag{6.15}$$

where ad$x$ is the image of x under the adjoint representation of $\mathfrak{g}$.

These charges are linearly independent if all the Killing forms are 0 [2]. However, from a linearly dependent set of charges, one can easily form a linearly independent set by summing over different charges.

In our framework, charges can commute in two ways. First, they may be components of distinct algebras, as exemplified by the Hubbard model. Alternatively, they can belong to the same Cartan subalgebra, denoted by $\mathfrak{h}$, which will be illustrated with the $\mathfrak{su}(3)$ example. In this scenario, the procedure adds dynamical symmetries for the charges at Step 4. It is important to note that root vectors are associated with specific charges, as indicated in Eq. (3.3). We could deconstruct this step by sequentially adding the dynamical symmetries for each of the charges within $\mathfrak{h}$. Doing so would highlight that introducing a new charge preserves the dynamical symmetries established by the preceding charges.

Charges noncommutation enters the picture in step 5. If the charges generate a $\mathfrak{g}$, there is the possibility that the full set of charges does not commute. The Cartan-Weyl basis is a basis for $\mathfrak{g}$. The charges also form a basis for $\mathfrak{g}$. Thus, the elements of the Cartan-Weyl basis can be written in the basis of the charges, i.e., the dynamical symmetries can be written as a linear combination of charges. Thus, if the Hamiltonian commutes with more noncommuting charges, it will commute with more dynamical symmetries. This is why introducing noncommuting charges leads to removing existing dynamical symmetries.

6.4.2 Illustration using $\mathfrak{su}(2)$

First, we consider charges represented by $\mathfrak{su}(2)$. $\{\sigma_x, \sigma_y, \sigma_z\}$ are the usual Pauli operators. Consider again a system of N sites. We denote by $\sigma_\alpha^{(j)}$ a Pauli operator acting on the jth site. We define the operators $S_\alpha^{\text{tot}} \coloneqq \sum_{j=1}^N \sigma_\alpha^{(j)}$. If we were studying the full algebra, we would have three charges that are the components of the spin-$\frac{1}{2}$ angular momentum.

First, we will consider having a single Cartan subalgebra and return to the full algebra later. The system has $c = 3$ and $r = 1$. Thus, its maximal Abelian subalgebra will have one element. To be concrete, we choose this element to be S_z^{tot}. Next, we complete the Cartan-Weyl basis by identifying the root vectors of the algebra, which are

$$S_{\pm z}^{\text{tot}} = \sum_{j=1}^{N} \mathbb{1}^{\otimes(j-1)} \otimes S_{\pm z}^{(j)} \otimes \mathbb{1}^{\otimes(N-j)} \equiv \sum_{j=1}^{N} S_{\pm z}^{(j)} \tag{6.16}$$

where $S_{\pm z} = \frac{1}{2}(\sigma_x \pm i\sigma_y)$. Starting from the system's charge, we identified two dynamical symmetries. Like with the Hubbard model, it is straightforward to reverse this procedure. Doing so, we check that $[S_{+z}, S_{-z}] = S_z$, and thus $\left[S_{+z}^{\text{tot}}, S_{-z}^{\text{tot}}\right] = S_z^{\text{tot}}$.

The system described above has one charge and one pair of dynamical symmetries. We now aim to introduce another charge that does not commute with the existing one, such as S_x^{tot}. However, a Hamiltonian that conserves two $\mathfrak{su}(2)$ charges will necessarily conserve all three [2]. Thus, we introduce two additional charges into the system, thereby applying the procedure from Sec. 6.4.1 for $\mathfrak{su}(2)$. The first round of steps 1 to 4 for finding the dynamical symmetries of the full $\mathfrak{su}(2)$ is equivalent to finding the dynamical symmetries of one Cartan subalgebra of $\mathfrak{su}(2)$. To complete $\mathfrak{su}(2)$, we include S_x^{tot} and S_y^{tot} as charges.

Say we did not check whether these new charges remove earlier dynamical symmetries in step 5. We would then choose one of these two charges and repeat steps 1 to 4. Doing so we would find the dynamical symmetries $S_{\pm\alpha}^{\text{tot}} = \sum_{j=1}^N S_{\pm\alpha}^{(j)}$ for $\alpha = x$ and y, where $S_{\pm x} = \frac{1}{2}(\sigma_z \mp i\sigma_y)$ and $S_{\pm y} = \frac{1}{2}(\sigma_z \pm i\sigma_x)$. It is straightforward to check that $\left[S_{+x}^{\text{tot}}, S_{-x}^{\text{tot}}\right] = S_x^{\text{tot}}$ and $\left[S_{+y}^{\text{tot}}, S_{-y}^{\text{tot}}\right] = S_y^{\text{tot}}$. If we did these steps for both additional charges, we would have identified $\frac{c}{r}(c - r) = 6$ dynamical symmetries. However, we find a different story when we check whether the additional charge removes any of the previous dynamical symmetries (see step 5). Introducing the charges means that the Hamiltonian now commutes with $S_{\pm x}^{\text{tot}}$ and $S_{\pm y}^{\text{tot}}$, and thus also commutes with $S_{\pm z}^{\text{tot}}$. Together, the three conservation laws eliminate all six dynamical symmetries we listed above. When the system had one charge of $\mathfrak{su}(2)$, it had two dynamical symmetries. Now that the system has three charges of $\mathfrak{su}(2)$ it has no dynamical symmetries. This example contrasts with the Hubbard model, where

the dynamical symmetries of $S^{\text{tot}}_{\pm z}$ could coexist with that of another charge that commutes with $S^{\text{tot}}_{\pm z}$.

6.4.3 Illustration using $\mathfrak{su}(3)$

To demonstrate the second way charges can commute in our construction—from being part of the same Cartan subalgebra—we turn to $\mathfrak{su}(3)$. $\mathfrak{su}(3)$ has dimension $c = 8$ and rank $r = 2$. Thus, our system has eight charges that we can partition $\frac{c}{r} = 4$ sets of mutually commuting charges. These sets generate Cartan subalgebras. The eight charges of $\mathfrak{su}(3)$ can be represented by the Gell–Mann matrices [82], τ_i for $i = 1$ to 8.

We begin with one Cartan sublagebra of $\mathfrak{su}(3)$. For example, take the Cartan subalgebra with τ_3 and τ_8. In the three-dimensional representation of $\mathfrak{su}(3)$, these operators can be represented with

$$\tau_3 = \begin{bmatrix} 1 & 0 & 0 \\ 0 & -1 & 0 \\ 0 & 0 & 0 \end{bmatrix} \quad \text{and} \quad \tau_8 = \frac{1}{\sqrt{3}} \begin{bmatrix} 1 & 0 & 0 \\ 0 & 1 & 0 \\ 0 & 0 & -2 \end{bmatrix}. \tag{6.17}$$

As before, our charges will be sums over these operators on each site, $Q_1 = \sum_{j=1}^{N} \tau_3^{(j)}$ and $Q_2 = \sum_{j=1}^{N} \tau_9^{(j)}$. Using this Cartan subalgebra, we construct a Cartan-Weyl basis. This requires identifying $\frac{c-r}{2} = 3$ pairs of root vectors. We define the following operators, $A_{+1} \coloneqq \tau_1 + i\tau_2$, $A_{+2} \coloneqq \tau_4 + i\tau_5$, and $A_{+3} \coloneqq \tau_6 + i\tau_7$. These operators and their Hermitian conjugates are the root vectors. As we did in the previous example, we can construct the dynamical symmetries by taking sums over the operators on each site in our chain, $A^{\text{tot}}_{\pm\beta} := \sum_{j=1}^{N} A^{(j)}_{\pm\beta}$. Thus, we have again found the dynamical symmetries from the charges.

We could reverse this procedure to find the charges generated by these dynamical symmetries. We do this explicitly to point out an effect not observed in the $\mathfrak{su}(2)$ cases.

We identify the operators,

$$Q_1 = c_1[A_{+1}, A_{-1}] = \frac{1}{\sqrt{2}} \begin{bmatrix} 1 & 0 & 0 \\ 0 & -1 & 0 \\ 0 & 0 & 0 \end{bmatrix}, \tag{6.18}$$

$$Q_{\tilde{2}} = c_2[A_{+2}, A_{-2}] = \frac{1}{\sqrt{2}} \begin{bmatrix} 1 & 0 & 0 \\ 0 & 0 & 0 \\ 0 & 0 & -1 \end{bmatrix}, \text{ and} \tag{6.19}$$

$$Q_{\tilde{3}} = c_3[A_{+3}, A_{-3}] = \frac{1}{\sqrt{2}} \begin{bmatrix} 0 & 0 & 0 \\ 0 & 1 & 0 \\ 0 & 0 & -1 \end{bmatrix}. \tag{6.20}$$

Note that they are not linearly independent since not all of the Killing forms between all pairs are zero. The Killing form, Eq. (6.15) reduces to $2n\mathrm{tr}(XY)$ for $\mathfrak{su}(n)$. We have then that $(Q_1, Q_{\tilde{2}}) = 3, (Q_1, Q_{\tilde{3}}) = -3$, and $(Q_{\tilde{2}}, Q_{\tilde{3}}) = 3$. A Cartan subalgebra basis will require two charges. Thus, we sum over two of these three operators. We are free to do so in different ways. The choice that recovers the original two operators we began the procedure with is summing over charges $Q_{\tilde{2}}$ and $Q_{\tilde{3}}$: $Q_2 = \frac{1}{\sqrt{3}}(Q_{\tilde{2}} + Q_{\tilde{3}})$.

The system described above has two charges and three pairs of dynamical symmetries. We now want to introduce other charges that do not commute with the existing ones, i.e., more of the charges that generate $\mathfrak{su}(3)$. However, recall the dynamical symmetries for τ_3 and τ_8 are linear combinations of the other six Gell–Mann matrices. If the Hamiltonian now commutes with any elements from other Cartan subalgebras of $\mathfrak{su}(3)$, it will stop some combination of A_1, A_2, and A_3 from being dynamical symmetries. If the Hamiltonian commutes with all of $\mathfrak{su}(3)$'s charges, it will nullify the system's dynamical symmetries. When the system had two commuting charges, it had six dynamical symmetries. Now that it has eight noncommuting charges, it has no dynamical symmetries.

6.4.4 Hamiltonians

Although the primary aim of this study is not to construct Hamiltonians, we include some examples to connect our findings with physically viable systems and establish a link with research on quantum scars [176]. We start with the $\mathfrak{su}(2)$ case, illustrating how various Hamiltonians can transition from a single charge forming a Cartan subalgebra of $\mathfrak{su}(2)$ (U(1) symmetry) to three charges constituting the full algebra (SU(2) symmetry).

An example of this is the Heisenberg model under an external field.

$$H_2 = \frac{B}{2}\Big(\sum_{j=1}^{N}\sigma_z^{(j)}\Big) + \frac{J}{2}\Big(\sum_{\langle j,k\rangle}\sum_{\langle\langle j,k\rangle\rangle}\sigma_x^{(j)}\sigma_x^{(k)} + \sigma_y^{(j)}\sigma_y^{(k)} + \sigma_z^{(j)}\sigma_z^{(k)}\Big), \tag{6.21}$$

where $\langle j,k\rangle$ indicates the sum over nearest neighbours, $\langle\langle j,k\rangle\rangle$ indicates the sum is over next-nearest neighbours, B is the strength of an external magnetic field, and J is a coupling constant. For $B \neq 0$, the system has one charge corresponding to a Cartan subalgebra of $\mathfrak{su}(2)$ and one pair of dynamical symmetries. By setting $B = 0$, we introduce two additional noncommuting charges into the system, thereby removing the dynamical symmetries. We included the next-nearest neighbour interaction to break integrability. Alternatively, we could construct our Hamiltonian using genuine three-body interactions that are SU(2)-symmetric, such as

$$\begin{aligned}&\sigma_x^{(j)}\sigma_y^{(j+1)}\sigma_z^{(j+2)} + \sigma_y^{(j)}\sigma_z^{(j+1)}\sigma_x^{(j+2)} + \sigma_z^{(j)}\sigma_x^{(j+1)}\sigma_y^{(j+2)}\\ -&\sigma_z^{(j)}\sigma_y^{(j+1)}\sigma_x^{(j+2)} - \sigma_x^{(j)}\sigma_z^{(j+1)}\sigma_y^{(j+2)} - \sigma_y^{(j)}\sigma_x^{(j+1)}\sigma_z^{(j+2)},\end{aligned} \tag{6.22}$$

and then break the symmetry with an external field.

We can similarly study Hamiltonians for the $\mathfrak{su}(3)$ example. These Hamiltonians are less familiar but can be derived using the procedure in Ref.[2],

$$H_3 = \frac{J}{2}\Big(\sum_{\alpha}\sum_{\langle j,k\rangle}\sum_{\langle\langle j,k\rangle\rangle}\tau_\alpha^{(j)}\tau_\alpha^{(k)}\Big) + \frac{B_1}{2}\Big(\sum_j \tau_3^{(j)}\Big) + \frac{B_2}{2}\Big(\sum_j \tau_8^{(j)}\Big). \tag{6.23}$$

Setting B_1 and B_2 to zero allows the noncommuting charges to give way to dynamical symmetries. These Hamiltonians align with the procedure presented in Ref. [176], where the introduction of an external field breaks the non-Abelian symmetry and facilitates the emergence of quantum scars. Notably, the transitions in the Hamiltonian that give rise to quantum scars also lead to non-thermalizing local observables. This connection between quantum scars and non-thermalizing observables presents an avenue for future research.

6.5 Summary & Outlook

This work addresses the unresolved question of whether noncommuting charges aid or hinder thermalization [3, 46, 47, 154, 155, 156, 157, 158, 4, 159, 55, 1, 160]. We found

that noncommuting charges reduce the set of local observables that achieve thermalization under the ETH, leading these systems toward thermal equilibrium. This result underscores the role of noncommuting charges in promoting thermalization.

Our findings reveal that noncommuting charges remove the non-thermalizing dynamics that emerge from dynamical symmetries. While dynamical symmetries are sufficient conditions to produce non-thermalizing dynamics, they are not necessary. A natural next step is to investigate the impact of noncommuting and commuting charges on the non-thermalizing dynamics in Hamiltonians without dynamical symmetries. For example, we could alter the Heisenberg Hamiltonian to break its non-Abelian symmetry without using an external field. This could be done by adding a coupling term like $(\sigma_x^{(j)}\sigma_y^{(j+1)} - \sigma_y^{(j)}\sigma_x^{(j+1)})$, which also retains the U(1) symmetry. If noncommuting charges diminish non-thermalizing dynamics under these conditions, their role in promoting thermalization would be further substantiated. If not, this would suggest that the thermalization-promoting ability of noncommuting charges is limited to certain systems.

Non-Abelian symmetries have now been shown to suppress three forms of non-thermalizing behaviour: quantum scars [176], many-body localization (MBL) [73, 182], and the phenomena observed in this study. There are two reasons to seek a link between these findings. In Section 6.4.4, we showed that the perturbation causing quantum scars also leads to non-thermalizing dynamics in local observables. Although a direct link between quantum scars and observables violating the ETH has not been established, similarities in the Hamiltonians suggest a potential connection. Second, both the studies of quantum scars and MBL highlight the elimination of low-entangled states. Reference [182] shows that, in contrast to typical systems where MBL occurs, SU(2) symmetry mandates eigenstates with entanglement exceeding area law. Meanwhile, Reference [176] finds that breaking SU(2) symmetry removes states with subthermal entanglement entropy. Both of these works align with recent research that indicates non-Abelian symmetries can increase entanglement entropy [3]. Exploring a common underlying mechanism that connects these phenomena presents another promising avenue for future research.

The central theme of this discussion is unravelling the intricate influence of noncommuting charges on thermalization. On the one hand, several studies indicate that noncommuting charges obstruct thermalization, evidenced by deviations from the thermal state [47], slower entropy production [14], more constrained dynamics compared to systems with commuting charges [59], and difficulties in characterizing the thermal state [12, 13, 42, 43]. On the other hand, there is evidence suggesting they facilitate thermalization, as seen in increased average entanglement [3, 4], the elimination of many-body localization and quantum scars [73, 182, 176], and the findings of this study. This apparent contradiction highlights a complex and nuanced relationship between noncommuting charges and

thermalization, underscoring the need for more in-depth research to elucidate their role fully.

Chapter 7

Conclusions

Excerpts from this chapter are based on reference [1] and overlap with its text.

We conclude with a summary of the thesis's results. In our Perspective article [1], we highlighted five major research opportunities in noncommuting charges. This thesis has significantly advanced two of these five and contributed to another two. We briefly review these five opportunities (Section 7.1) and then connect our results to them (Section 7.2).

7.1 Research opportunities

Opportunity one: The predictions merit experimental testing. The first test of noncommuting-charge thermodynamics was performed with trapped ions [46]. Other potential platforms include superconducting qubits, quantum dots, ultracold atoms, quantum optics, and optomechanics [45, 2, 14].

Opportunity two: Existing results present a conceptual puzzle. Evidence suggests that noncommuting charges hinder thermalization to an extent: they invalidate derivations of the thermal state's form [12, 13], decrease thermodynamic-entropy production [14], clash with the ETH [47], and uniquely restrict the global unitaries implementable via local interactions [62]. Other evidence, however, suggests that noncommuting charges enhance thermalization: they destabilize MBL [73], increase average entanglement entropy [3, 4], and stop local observables from thermalizing [5]. These results do not conflict with each other, stemming from different setups. Yet the results clash conceptually. Reconciling them presents another opportunity. For example, one possible resolution is that noncommuting

charges hinder thermalization in some cases and promote it in others. If that is the case, resolving the puzzle would entail delineating these regimes.

Opportunity three: To what extent can classical mechanics reproduce noncommuting-charge thermodynamics? Observables' noncommutation underlies quintessentially quantum phenomena including uncertainty relations, measurement disturbance, and the Einstein–Podolsky–Rosen paradox. Yet classical mechanics features quantities that fail to commute with each other—for example, rotations about different axes. How nonclassical is noncommuting-charge thermodynamics (achievable only outside of classical physics), beyond being merely quantum (achievable within quantum physics)?

Opportunity four: Every chaotic or thermodynamic phenomenon merits re-examination. To what extent does it change under dynamics that conserve noncommuting charges? Example phenomena include diffusion coefficients, transport relations, thermalization times, monitored circuits [4], out-of-time-ordered correlators [183], operator spreading [130], frame potentials [184], and quantum-complexity growth [185].

Opportunity five: Noncommuting-charge thermodynamics merits bridging to similar topics in neighbouring fields. Non-Abelian gauge theories, non-Abelian hydrodynamics, generalize Gibbs ensemble studies, and dynamical phase transitions overlap with noncommuting thermodynamic charges. To what extent can these areas inform each other?

7.2 Summary of results

In Chapter 3, we outlined a method for constructing Hamiltonians that facilitate the local transportation of noncommuting charges while preserving global charge conservation. These Hamiltonians have the capacity to link multiple subsystems and may be either integrable or nonintegrable. Our findings bridged the conceptual gap between noncommuting thermodynamic charges in quantum information theory and practical applications in condensed matter, atomic, molecular, and optical (AMO) physics. The theoretical framework developed here paves the way for empirical validation through our proposed experimental setups. This work, thus, enabled the first major research opportunity.

Chapter 4 established that noncommuting charges can enhance the average entanglement, as supported by both numerical simulations and analytical calculations within microcanonical and approximate microcanonical subspaces. This work introduced the second research opportunity. This chapter's conclusions rest on two models closely resembling each other but differ in whether their charges commute. Our models can now be used to explore the effects of charges' noncommutation on other quantum phenomena. Possibilities

include chaos [109, 66], as analyzed with out-of-time-ordered correlators [110, 111, 112, 113] and random unitary circuits [114, 115]; bounds on quantum-simulation errors [116]; and quantum-machine-learning algorithms' performances [117]. Therefore, this chapter also contributes significantly to the fourth research opportunity.

In Chapter 5, we introduced noncommuting charges into monitored random circuits. Our study led to the identification of a critical phase transition. First, we numerically discovered a purification transition between a mixed phase (at $p < p_c \approx 0.35$) and a critical phase (at $p > p_c$). In the critical phase, the purification time scales as $t_P \sim L^2$. The purification transition doubles as an entanglement transition, which separates volume-law (at $p < p_c$) and subextensive (logarithmic or small-power-law, at $p > p_c$) entanglement scalings. Even in the measurement-only limit (at $p = 1$), the symmetry's non-Abelian nature enables greater than area-law entanglement scaling. Furthermore, we found the system's mutual information continues to grow past p_c. Our analysis extended noncommuting-charge thermodynamics to adjacent fields, supporting the fourth research opportunity.

Chapter 6 demonstrates that noncommuting charges remove the non-thermalizing dynamics that energy from dynamical symmetries. This is another form of non-thermal behaviour which is ruled out by noncommuting charges. This work was motivated by and directly contributed to the first research opportunity.

References

[1] Shayan Majidy, William F Braasch Jr, Aleksander Lasek, Twesh Upadhyaya, Amir Kalev, and Nicole Yunger Halpern. Noncommuting conserved charges in quantum thermodynamics and beyond. *Nature Reviews Physics*, 5(11):689–698, 2023.

[2] Nicole Yunger Halpern and Shayan Majidy. How to build Hamiltonians that transport noncommuting charges in quantum thermodynamics. *npj Quantum Information*, 8(1):10, 2022.

[3] Shayan Majidy, Aleksander Lasek, David A Huse, and Nicole Yunger Halpern. Non-abelian symmetry can increase entanglement entropy. *Physical Review B*, 107(4):045102, 2023.

[4] Shayan Majidy, Utkarsh Agrawal, Sarang Gopalakrishnan, Andrew C Potter, Romain Vasseur, and Nicole Yunger Halpern. Critical phase and spin sharpening in su (2)-symmetric monitored quantum circuits. *Physical Review B*, 108(5):054307, 2023.

[5] Shayan Majidy. Noncommuting charges' effect on the thermalization of local observables. *arXiv preprint arXiv:2403.13046*, 2024.

[6] Shayan-Shawn Majidy, Hemant Katiyar, Galit Anikeeva, Jonathan Halliwell, and Raymond Laflamme. Exploration of an augmented set of Leggett-Garg inequalities using a noninvasive continuous-in-time velocity measurement. *Physical Review A*, 100(4):042325, 2019.

[7] Shayan Majidy, Jonathan J Halliwell, and Raymond Laflamme. Detecting violations of macrorealism when the original Leggett-Garg inequalities are satisfied. *Physical Review A*, 103(6):062212, 2021.

[8] Shayan Majidy. A unification of the coding theory and OAQEC perspectives on hybrid codes. *International Journal of Theoretical Physics*, 62(8):177, 2023.

[9] Shayan Majidy, Christopher Wilson, and Raymond Laflamme. *Building Quantum Computers: A Practical Introduction*. Cambridge University Press, 2024.

[10] Shayan Majidy. Addressing misconceptions in university physics: A review and experiences from quantum physics educators. *arXiv preprint arXiv:2405.20923*, 2024.

[11] Robert Gilmore. *Lie groups, Lie algebras, and some of their applications*. Courier Corporation, 2012.

[12] Nicole Yunger Halpern. Beyond heat baths II: framework for generalized thermodynamic resource theories. *Journal of Physics A: Mathematical and Theoretical*, 51(9):094001, 2018.

[13] Nicole Yunger Halpern, Philippe Faist, Jonathan Oppenheim, and Andreas Winter. Microcanonical and resource-theoretic derivations of the thermal state of a quantum system with noncommuting charges. *Nat. Commun.*, 7:12051, Jul 2016.

[14] Gonzalo Manzano, Juan MR Parrondo, and Gabriel T Landi. Non-abelian quantum transport and thermosqueezing effects. *PRX Quantum*, 3(1):010304, 2022.

[15] Debashis Sen. The uncertainty relations in quantum mechanics. *Current Science*, pages 203–218, 2014.

[16] Patrick J Coles, Mario Berta, Marco Tomamichel, and Stephanie Wehner. Entropic uncertainty relations and their applications. *Reviews of Modern Physics*, 89(1):015002, 2017.

[17] Ernesto Benítez Rodríguez and Luis Arévalo Aguilar. A survey of the concept of disturbance in quantum mechanics. *Entropy*, 21(2):142, Feb 2019.

[18] Christopher J Fewster and Rainer Verch. Quantum fields and local measurements. *Communications in Mathematical physics*, 378:851–889, 2020.

[19] Alain Aspect. Bell's inequality test: more ideal than ever. *Nature*, 398(6724):189–190, 1999.

[20] Clive Emary, Neill Lambert, and Franco Nori. Leggett–garg inequalities. *Reports on Progress in Physics*, 77(1):016001, 2013.

[21] Shayan-Shawn Majidy. Violation of an augmented set of leggett-garg inequalities and the implementation of a continuous in time velocity measurement. Master's thesis, University of Waterloo, 2019.

[22] Adam M Kaufman, M Eric Tai, Alexander Lukin, Matthew Rispoli, Robert Schittko, Philipp M Preiss, and Markus Greiner. Quantum thermalization through entanglement in an isolated many-body system. *Science*, 353(6301):794–800, 2016.

[23] C. Neill, P. Roushan, M. Fang, Y. Chen, M. Kolodrubetz, Z. Chen, A. Megrant, R. Barends, B. Campbell, B. Chiaro, A. Dunsworth, E. Jeffrey, J. Kelly, J. Mutus, P. J. J. O'Malley, C. Quintana, D. Sank, A. Vainsencher, J. Wenner, T. C. White, A. Polkovnikov, and J. M. Martinis. Ergodic dynamics and thermalization in an isolated quantum system. *Nature Physics*, 12:1037, Jul 2016.

[24] Govinda Clos, Diego Porras, Ulrich Warring, and Tobias Schaetz. Time-resolved observation of thermalization in an isolated quantum system. *Phys. Rev. Lett.*, 117:170401, Oct 2016.

[25] Zhao-Yu Zhou, Guo-Xian Su, Jad C. Halimeh, Robert Ott, Hui Sun, Philipp Hauke, Bing Yang, Zhen-Sheng Yuan, Jürgen Berges, and Jian-Wei Pan. Thermalization dynamics of a gauge theory on a quantum simulator. *Science*, 377(6603):311–314, 2022.

[26] Mark Srednicki. Chaos and quantum thermalization. *Physical Review E*, 50(2):888, 1994.

[27] Josh M Deutsch. Quantum statistical mechanics in a closed system. *Physical Review A*, 43(4):2046, 1991.

[28] Edwin T Jaynes. Information Theory and Statistical Mechanics II. *Physical Review*, 108(2):171, 1957.

[29] Marcos Rigol, Vanja Dunjko, Vladimir Yurovsky, and Maxim Olshanii. Relaxation in a completely integrable many-body quantum system: an ab initio study of the dynamics of the highly excited states of 1d lattice hard-core bosons. *Physical Review Letters*, 98(5):050405, 2007.

[30] Marcos Rigol. Breakdown of thermalization in finite one-dimensional systems. *Physical Review Letters*, 103(10):100403, 2009.

[31] Tim Langen, Sebastian Erne, Remi Geiger, Bernhard Rauer, Thomas Schweigler, Maximilian Kuhnert, Wolfgang Rohringer, Igor E Mazets, Thomas Gasenzer, and Jörg Schmiedmayer. Experimental observation of a generalized Gibbs ensemble. *Science*, 348(6231):207–211, 2015.

[32] Lev Vidmar and Marcos Rigol. Generalized Gibbs ensemble in integrable lattice models. *Journal of Statistical Mechanics: Theory and Experiment*, 2016(6):064007, 2016.

[33] Roger Balian and NL Balazs. Equiprobability, inference, and entropy in quantum theory. *Annals of Physics*, 179(1):97–144, 1987.

[34] H. B. Callen. *Thermodynamics and an Introduction to Thermostatistics*. John Wiley & Sons, New York, 2 edition, 1985.

[35] L. D. Landau and E. M. Lifshitz. *Statistical Physics: Part 1*. Butterworth-Heinemann, 1980.

[36] Matteo Lostaglio. The resource theory of quantum thermodynamics. Master's thesis, Imperial College London, 2014.

[37] Michael A Nielsen and Isaac Chuang. Quantum computation and quantum information, 2002.

[38] Eric Chitambar and Gilad Gour. Quantum resource theories. *Reviews of Modern Physics*, 91(2):025001, 2019.

[39] Matteo Lostaglio. An introductory review of the resource theory approach to thermodynamics. *Reports on Progress in Physics*, 82(11):114001, oct 2019.

[40] Nicole Yunger Halpern and Joseph M Renes. Beyond heat baths: Generalized resource theories for small-scale thermodynamics. *Physical Review E*, 93(2):022126, 2016.

[41] Fernando Brandão, Michał Horodecki, Nelly Ng, Jonathan Oppenheim, and Stephanie Wehner. The second laws of quantum thermodynamics. *Proceedings of the National Academy of Science*, 112(11):3275–3279, 2015.

[42] Yelena Guryanova, Sandu Popescu, Anthony J. Short, Ralph Silva, and Paul Skrzypczyk. Thermodynamics of quantum systems with multiple conserved quantities. *Nat. Commun.*, 7:12049, Jul 2016.

[43] Matteo Lostaglio, David Jennings, and Terry Rudolph. Thermodynamic resource theories, non-commutativity and maximum entropy principles. *New J. Phys.*, 19(4):043008, 2017.

[44] Erick Hinds Mingo, Yelena Guryanova, Philippe Faist, and David Jennings. Quantum thermodynamics with multiple conserved quantities. In *Thermodynamics in the Quantum Regime*, pages 751–771. Springer, 2018.

[45] Nicole Yunger Halpern, Michael E. Beverland, and Amir Kalev. Noncommuting conserved charges in quantum many-body thermalization. *Phys. Rev. E*, 101:042117, Apr 2020.

[46] Florian Kranzl, Aleksander Lasek, Manoj K Joshi, Amir Kalev, Rainer Blatt, Christian F Roos, and Nicole Yunger Halpern. Experimental observation of thermalisation with noncommuting charges. *arXiv:2202.04652*, 2022.

[47] Chaitanya Murthy, Arman Babakhani, Fernando Iniguez, Mark Srednicki, and Nicole Yunger Halpern. Non-abelian eigenstate thermalization hypothesis. *Phys. Rev. Lett.*, 130:140402, Apr 2023.

[48] Marcos Rigol, Vanja Dunjko, and Maxim Olshanii. Thermalization and its mechanism for generic isolated quantum systems. *Nature*, 452(7189):854–858, 2008.

[49] Vincent Bouchard. Ma ph 464 - group theory in physics: Lecture notes. https://sites.ualberta.ca/ vbouchar/MAPH464/front.html, 2020. University of Alberta.

[50] Gilad Gour and Robert W Spekkens. The resource theory of quantum reference frames: manipulations and monotones. *New Journal of Physics*, 10(3):033023, mar 2008.

[51] Thiago R. de Oliveira, Christos Charalambous, Daniel Jonathan, Maciej Lewenstein, and Arnau Riera. Equilibration time scales in closed many-body quantum systems. *New Journal of Physics*, 20(3):033032, mar 2018.

[52] Shantanav Chakraborty, Kyle Luh, and Jérémie Roland. How fast do quantum walks mix? *Phys. Rev. Lett.*, 124:050501, Feb 2020.

[53] Gonzalo Manzano. Squeezed thermal reservoir as a generalized equilibrium reservoir. *Phys. Rev. E*, 98(4):042123, 2018.

[54] Sareh Shahidani. Thermodynamic forces and flows between a thermal bath and a squeezed thermal bath: Application to optomechanical systems. *Physical Review A*, 105(6):063516, 2022.

[55] Twesh Upadhyaya, William F Braasch Jr, Gabriel T Landi, and Nicole Yunger Halpern. What happens to entropy production when conserved quantities fail to commute with each other. *arXiv preprint arXiv:2305.15480*, 2023.

[56] David P. DiVincenzo. Two-bit gates are universal for quantum computation. *Physical Review A*, 51(2):1015–1022, February 1995. Publisher: American Physical Society.

[57] Seth Lloyd. Almost Any Quantum Logic Gate is Universal. *Physical Review Letters*, 75(2):346–349, July 1995. Publisher: American Physical Society.

[58] David Elieser Deutsch, Adriano Barenco, and Artur Ekert. Universality in quantum computation. *Proceedings of the Royal Society of London. Series A: Mathematical and Physical Sciences*, 449(1937):669–677, January 1997. Publisher: Royal Society.

[59] Iman Marvian. Restrictions on realizable unitary operations imposed by symmetry and locality. *Nature Physics*, 18(3):283–289, 2022.

[60] Iman Marvian, Hanqing Liu, and Austin Hulse. Qudit circuits with SU(d) symmetry: Locality imposes additional conservation laws. *arXiv:2105.12877*, may 2021.

[61] Iman Marvian, Hanqing Liu, and Austin Hulse. Rotationally-Invariant Circuits: Universality with the exchange interaction and two ancilla qubits. *arXiv:2202.01963*, 2022.

[62] Iman Marvian. (Non-)Universality in symmetric quantum circuits: Why Abelian symmetries are special. *arXiv e-prints*, page arXiv:2302.12466, February 2023.

[63] Ramamurti Shankar. *Principles of quantum mechanics*. Springer Science & Business Media, 2012.

[64] Jae Dong Noh. Eigenstate thermalization hypothesis in two-dimensional xxz model with or without su (2) symmetry. *arXiv preprint arXiv:2210.14589*, 2022.

[65] Zh. Zhang, J. Tindall, J. Mur-Petit, D. Jaksch, and B. Buča. Stationary state degeneracy of open quantum systems with non-abelian symmetries. *Journal of Physics A*, 53(21):215304, may 2020.

[66] Luca D'Alessio, Yariv Kafri, Anatoli Polkovnikov, and Marcos Rigol. From quantum chaos and eigenstate thermalization to statistical mechanics and thermodynamics. *Adv. Phys.*, 65(3):239–362, 2016.

[67] Norbert Rosenzweig and Charles E. Porter. "repulsion of energy levels" in complex atomic spectra. *Phys. Rev.*, 120:1698–1714, Dec 1960.

[68] Olivier Giraud, Nicolas Macé, Éric Vernier, and Fabien Alet. Probing symmetries of quantum many-body systems through gap ratio statistics. *Physical Review X*, 12(1):011006, 2022.

[69] Dmitry A Abanin, Ehud Altman, Immanuel Bloch, and Maksym Serbyn. Colloquium: Many-body localization, thermalization, and entanglement. *Reviews of Modern Physics*, 91(2):021001, 2019.

[70] Sarang Gopalakrishnan and David A Huse. Instability of many-body localized systems as a phase transition in a nonstandard thermodynamic limit. *Physical Review B*, 99(13):134305, 2019.

[71] DM Basko, IL Aleiner, and BL Altshuler. Possible experimental manifestations of the many-body localization. *Physical Review B*, 76(5):052203, 2007.

[72] Ming Gong, Gentil D de Moraes Neto, Chen Zha, Yulin Wu, Hao Rong, Yangsen Ye, Shaowei Li, Qingling Zhu, Shiyu Wang, Youwei Zhao, et al. Experimental characterization of the quantum many-body localization transition. *Physical Review Research*, 3(3):033043, 2021.

[73] Andrew C Potter and Romain Vasseur. Symmetry constraints on many-body localization. *Physical Review B*, 94(22):224206, 2016.

[74] Sai Vinjanampathy and Janet Anders. Quantum thermodynamics. *Contemporary Physics*, 57(4):545–579, 2016.

[75] Ashok Das and Susumu Okubo. *Lie groups and Lie algebras for physicists*. World Scientific, 2014.

[76] Francesco Iachello. *Lie algebras and applications*, volume 12. Springer, 2006.

[77] James E Humphreys. *Introduction to Lie algebras and representation theory*, volume 9. Springer Science & Business Media, 2012.

[78] Rodney J Baxter. *Exactly solved models in statistical mechanics*. Elsevier, 2016.

[79] Kouhei Fukai, Yuji Nozawa, Koji Kawahara, and Tatsuhiko N Ikeda. Noncommutative generalized Gibbs ensemble in isolated integrable quantum systems. *Phys. Rev. Res.*, 2(3):033403, 2020.

[80] Christian Gogolin and Jens Eisert. Equilibration, thermalisation, and the emergence of statistical mechanics in closed quantum systems. *Rep. Prog. Phys.*, 79(5):056001, 2016.

[81] Murray Gell-Mann. Symmetries of baryons and mesons. In *Murray Gell-Mann: Selected Papers*, pages 128–145. World Scientific, 2010.

[82] Robert N. Cahn. *Semi-Simple Lie Algebras and Their Representations*. Dover, 2006.

[83] Mark Byrd. Differential geometry on su (3) with applications to three state systems. *J. Math. Phys.*, 39(11):6125–6136, 1998.

[84] Hai-Tao Quan, Yu-xi Liu, Chang-Pu Sun, and Franco Nori. Quantum thermodynamic cycles and quantum heat engines. *Phys. Rev. E*, 76(3):031105, 2007.

[85] J. Q. You and Franco Nori. Atomic physics and quantum optics using superconducting circuits. *Nature*, 474(7353):589–597, 2011.

[86] Jens Koch, M Yu Terri, Jay Gambetta, Andrew A Houck, DI Schuster, J Majer, Alexandre Blais, Michel H Devoret, Steven M Girvin, and Robert J Schoelkopf. Charge-insensitive qubit design derived from the cooper pair box. *Phys. Rev. A*, 76(4):042319, 2007.

[87] Romeo Bianchetti, Stefan Filipp, Matthias Baur, Johannes M Fink, Christian Lang, Lars Steffen, Maxime Boissonneault, Alexandre Blais, and Andreas Wallraff. Control and tomography of a three level superconducting artificial atom. *Phys. Rev. Lett.*, 105(22):223601, 2010.

[88] Alexis Morvan, VV Ramasesh, MS Blok, JM Kreikebaum, K O'Brien, L Chen, BK Mitchell, RK Naik, DI Santiago, and I Siddiqi. Qutrit randomized benchmarking. *Phys. Rev. Lett.*, 126(21):210504, 2021.

[89] Machiel S Blok, VV Ramasesh, Thomas Schuster, K O'Brien, JM Kreikebaum, D Dahlen, A Morvan, Beni Yoshida, Norman Y Yao, and Irfan Siddiqi. Quantum information scrambling on a superconducting qutrit processor. *Phys. Rev. X*, 11(2):021010, 2021.

[90] KS Kumar, Antti Vepsäläinen, S Danilin, and GS Paraoanu. Stimulated raman adiabatic passage in a three-level superconducting circuit. *Nat. Commun.*, 7(1):1–6, 2016.

[91] HK Xu, C Song, WY Liu, GM Xue, FF Su, Hui Deng, Ye Tian, DN Zheng, Siyuan Han, You-Peng Zhong, et al. Coherent population transfer between uncoupled or weakly coupled states in ladder-type superconducting qutrits. *Nat. Commun.*, 7(1):1–6, 2016.

[92] Xinsheng Tan, Dan-Wei Zhang, Qiang Liu, Guangming Xue, Hai-Feng Yu, Yan-Qing Zhu, Hui Yan, Shi-Liang Zhu, and Yang Yu. Topological maxwell metal bands in a superconducting qutrit. *Phys. Rev. Lett.*, 120(13):130503, 2018.

[93] Antti Vepsäläinen, Sergey Danilin, and Gheorghe Sorin Paraoanu. Superadiabatic population transfer in a three-level superconducting circuit. *Sci. Adv.*, 5(2):eaau5999, 2019.

[94] He-Liang Huang, Dachao Wu, Daojin Fan, and Xiaobo Zhu. Superconducting quantum computing: a review. *Sci. China Inf. Sci.*, 63(8):1–32, 2020.

[95] Morten Kjaergaard, Mollie E Schwartz, Jochen Braumüller, Philip Krantz, Joel I-J Wang, Simon Gustavsson, and William D Oliver. Superconducting qubits: Current state of play. *Annu. Rev. Condens. Matter Phys,*, 11:369–395, 2020.

[96] Mark Van Raamsdonk. Building up space–time with quantum entanglement. *International Journal of Modern Physics D*, 19(14):2429–2435, 2010.

[97] Brian Swingle. Spacetime from entanglement. *Annual Review of Condensed Matter Physics*, 9:345–358, 2018.

[98] ChunJun Cao, Sean M Carroll, and Spyridon Michalakis. Space from Hilbert space: recovering geometry from bulk entanglement. *Physical Review D*, 95(2):024031, 2017.

[99] Brian Skinner, Jonathan Ruhman, and Adam Nahum. Measurement-induced phase transitions in the dynamics of entanglement. *Physical Review X*, 9(3):031009, 2019.

[100] Yaodong Li, Xiao Chen, and Matthew PA Fisher. Measurement-driven entanglement transition in hybrid quantum circuits. *Physical Review B*, 100(13):134306, 2019.

[101] Rolando Somma, Gerardo Ortiz, Howard Barnum, Emanuel Knill, and Lorenza Viola. Nature and measure of entanglement in quantum phase transitions. *Physical Review A*, 70(4):042311, 2004.

[102] Scott D Geraedts, Nicolas Regnault, and Rahul M Nandkishore. Characterizing the many-body localization transition using the entanglement spectrum. *New Journal of Physics*, 19(11):113021, 2017.

[103] Don N Page. Average entropy of a subsystem. *Physical Review Letters*, 71(9):1291, 1993.

[104] Alexander Altland, David A Huse, and Tobias Micklitz. Maximum entropy quantum state distributions. *arXiv:2203.12580*, 2022.

[105] Felipe Monteiro, Masaki Tezuka, Alexander Altland, David A Huse, and Tobias Micklitz. Quantum ergodicity in the many-body localization problem. *Physical Review Letters*, 127(3):030601, 2021.

[106] PennyLane. Understanding the Haar measure, 2021.

[107] Nathaniel Johnston. QETLAB: A MATLAB toolbox for quantum entanglement, version 0.9, Jan 2016.

[108] Yoshiko Ogata. Approximating macroscopic observables in quantum spin systems with commuting matrices. *Journal of Functional Analysis*, 264(9):2005–2033, 2013.

[109] Hans-Jürgen Stöckmann. Quantum chaos: an introduction, 2000.

[110] Koji Hashimoto, Keiju Murata, and Ryosuke Yoshii. Out-of-time-order correlators in quantum mechanics. *Journal of High Energy Physics*, 2017(10):1–31, 2017.

[111] Efim B Rozenbaum, Sriram Ganeshan, and Victor Galitski. Lyapunov exponent and out-of-time-ordered correlator's growth rate in a chaotic system. *Physical Review Letters*, 118(8):086801, 2017.

[112] Ignacio García-Mata, Marcos Saraceno, Rodolfo A Jalabert, Augusto J Roncaglia, and Diego A Wisniacki. Chaos signatures in the short and long time behavior of the out-of-time ordered correlator. *Physical Review Letters*, 121(21):210601, 2018.

[113] José Raúl González Alonso, Nathan Shammah, Shahnawaz Ahmed, Franco Nori, and Justin Dressel. Diagnosing quantum chaos with out-of-time-ordered-correlator quasiprobability in the kicked-top model. *arXiv:2201.08175*, 2022.

[114] Matthew PA Fisher, Vedika Khemani, Adam Nahum, and Sagar Vijay. Random quantum circuits. *Annual Review of Condensed Matter Physics*, 14:335–373, 2022.

[115] Austin Hulse, Hanqing Liu, and Iman Marvian. Qudit circuits with su (d) symmetry: Locality imposes additional conservation laws. *arXiv:2105.12877*, 2021.

[116] Iulia Buluta and Franco Nori. Quantum simulators. *Science*, 326(5949):108–111, 2009.

[117] Jacob Biamonte, Peter Wittek, Nicola Pancotti, Patrick Rebentrost, Nathan Wiebe, and Seth Lloyd. Quantum machine learning. *Nature*, 549(7671):195–202, 2017.

[118] Pasquale Calabrese, Jérôme Dubail, and Sara Murciano. Symmetry-resolved entanglement entropy in wess-zumino-witten models. *Journal of High Energy Physics*, 2021(10):1–32, 2021.

[119] Moshe Goldstein and Eran Sela. Symmetry-resolved entanglement in many-body systems. *Physical Review Letters*, 120(20):200602, 2018.

[120] Suting Zhao, Christian Northe, and René Meyer. Symmetry-resolved entanglement in AdS3/CFT2 coupled to U(1) chern-simons theory. *Journal of High Energy Physics*, 2021(7):1–38, 2021.

[121] Suting Zhao, Christian Northe, Konstantin Weisenberger, and René Meyer. Charged moments in w3 higher spin holography. *Journal of High Energy Physics*, 2022(5):166, 2022.

[122] Eugenio Bianchi and Pietro Dona. Typical entanglement entropy in the presence of a center: Page curve and its variance. *Physical Review D*, 100(10):105010, 2019.

[123] Norbert M Linke, Sonika Johri, Caroline Figgatt, Kevin A Landsman, Anne Y Matsuura, and Christopher Monroe. Measuring the rényi entropy of a two-site fermi-Hubbard model on a trapped ion quantum computer. *Physical Review A*, 98(5):052334, 2018.

[124] Rajibul Islam, Ruichao Ma, Philipp M Preiss, M Eric Tai, Alexander Lukin, Matthew Rispoli, and Markus Greiner. Measuring entanglement entropy in a quantum many-body system. *Nature*, 528(7580):77–83, 2015.

[125] Tiff Brydges, Andreas Elben, Petar Jurcevic, Benoît Vermersch, Christine Maier, Ben P Lanyon, Peter Zoller, Rainer Blatt, and Christian F Roos. Probing rényi entanglement entropy via randomized measurements. *Science*, 364(6437):260–263, 2019.

[126] Alexander Lukin, Matthew Rispoli, Robert Schittko, M Eric Tai, Adam M Kaufman, Soonwon Choi, Vedika Khemani, Julian Léonard, and Markus Greiner. Probing entanglement in a many-body–localized system. *Science*, 364(6437):256–260, 2019.

[127] Julian Léonard, Matthew Rispoli, Alexander Lukin, Robert Schittko, Sooshin Kim, Joyce Kwan, Dries Sels, Eugene Demler, and Markus Greiner. Signatures of bath-induced quantum avalanches in a many-body–localized system. *arXiv:2012.15270*, 2020.

[128] Brian Skinner. Lecture notes: Introduction to random unitary circuits and the measurement-induced entanglement phase transition. *arXiv preprint arXiv:2307.02986*, 2023.

[129] Andrew C Potter and Romain Vasseur. Entanglement dynamics in hybrid quantum circuits. In *Entanglement in Spin Chains: From Theory to Quantum Technology Applications*, pages 211–249. Springer, 2022.

[130] Vedika Khemani, Ashvin Vishwanath, and David A Huse. Operator spreading and the emergence of dissipative hydrodynamics under unitary evolution with conservation laws. *Physical Review X*, 8(3):031057, 2018.

[131] Tibor Rakovszky, Frank Pollmann, and CW Von Keyserlingk. Diffusive hydrodynamics of out-of-time-ordered correlators with charge conservation. *Physical Review X*, 8(3):031058, 2018.

[132] Utkarsh Agrawal, Aidan Zabalo, Kun Chen, Justin H Wilson, Andrew C Potter, JH Pixley, Sarang Gopalakrishnan, and Romain Vasseur. Entanglement and charge-sharpening transitions in u (1) symmetric monitored quantum circuits. *Physical Review X*, 12(4):041002, 2022.

[133] Shengqi Sang and Timothy H Hsieh. Measurement-protected quantum phases. *Physical Review Research*, 3(2):023200, 2021.

[134] Yaodong Li and Matthew Fisher. Robust decoding in monitored dynamics of open quantum systems with z_2 symmetry. *arXiv preprint arXiv:2108.04274*, 2021.

[135] Ali Lavasani, Yahya Alavirad, and Maissam Barkeshli. Measurement-induced topological entanglement transitions in symmetric random quantum circuits. *Nature Physics*, 17(3):342–347, 2021.

[136] Matteo Ippoliti, Michael J Gullans, Sarang Gopalakrishnan, David A Huse, and Vedika Khemani. Entanglement phase transitions in measurement-only dynamics. *Physical Review X*, 11(1):011030, 2021.

[137] Ali Lavasani, Yahya Alavirad, and Maissam Barkeshli. Topological order and criticality in (2+ 1) d monitored random quantum circuits. *Physical Review Letters*, 127(23):235701, 2021.

[138] Amos Chan, Rahul M. Nandkishore, Michael Pretko, and Graeme Smith. Unitary-projective entanglement dynamics. *Phys. Rev. B*, 99:224307, Jun 2019.

[139] Xiangyu Cao, Antoine Tilloy, and Andrea De Luca. Entanglement in a fermion chain under continuous monitoring. *SciPost Physics*, 7(2):024, 2019.

[140] Adam Nahum, Sthitadhi Roy, Brian Skinner, and Jonathan Ruhman. Measurement and entanglement phase transitions in all-to-all quantum circuits, on quantum trees, and in Landau-Ginsburg theory. *PRX Quantum*, 2(1):010352, 2021.

[141] Xiao Chen, Yaodong Li, Matthew PA Fisher, and Andrew Lucas. Emergent conformal symmetry in nonunitary random dynamics of free fermions. *Physical Review Research*, 2(3):033017, 2020.

[142] Ori Alberton, Michael Buchhold, and Sebastian Diehl. Entanglement transition in a monitored free-fermion chain: From extended criticality to area law. *Physical Review Letters*, 126(17):170602, 2021.

[143] Adam Nahum and Brian Skinner. Entanglement and dynamics of diffusion-annihilation processes with majorana defects. *Physical Review Research*, 2(2):023288, 2020.

[144] Michael J Gullans and David A Huse. Dynamical purification phase transition induced by quantum measurements. *Physical Review X*, 10(4):041020, 2020.

[145] Michael J Gullans and David A Huse. Scalable probes of measurement-induced criticality. *Physical Review Letters*, 125(7):070606, 2020.

[146] Robert Cordery, Sanjoy Sarker, and Jan Tobochnik. Physics of the dynamical critical exponent in one dimension. *Physical Review B*, 24(9):5402, 1981.

[147] Neil W Ashcroft and N David Mermin. *Solid state physics*. Cengage Learning, 2022.

[148] Michael M Wolf, Frank Verstraete, Matthew B Hastings, and J Ignacio Cirac. Area laws in quantum systems: mutual information and correlations. *Physical Review Letters*, 100(7):070502, 2008.

[149] Fergus Barratt, Utkarsh Agrawal, Andrew C Potter, Sarang Gopalakrishnan, and Romain Vasseur. Transitions in the learnability of global charges from local measurements. *Physical Review Letters*, 129(20):200602, 2022.

[150] David Huse. Personal communication.

[151] Crystal Noel, Pradeep Niroula, Daiwei Zhu, Andrew Risinger, Laird Egan, Debopriyo Biswas, Marko Cetina, Alexey V Gorshkov, Michael J Gullans, David A Huse, et al. Measurement-induced quantum phases realized in a trapped-ion quantum computer. *Nature Physics*, 18(7):760–764, 2022.

[152] Jesse C Hoke, Matteo Ippoliti, Dmitry Abanin, Rajeev Acharya, Markus Ansmann, Frank Arute, Kunal Arya, Abraham Asfaw, Juan Atalaya, Joseph C Bardin, et al. Quantum information phases in space-time: measurement-induced entanglement and teleportation on a noisy quantum processor. *arXiv preprint arXiv:2303.04792*, 2023.

[153] Jin Ming Koh, Shi-Ning Sun, Mario Motta, and Austin J Minnich. Experimental realization of a measurement-induced entanglement phase transition on a superconducting quantum processor. *arXiv preprint arXiv:2203.04338*, 2022.

[154] Jae Dong Noh. Eigenstate thermalization hypothesis in two-dimensional x x z model with or without su (2) symmetry. *Physical Review E*, 107(1):014130, 2023.

[155] Julian Siegl and John Schliemann. Imperfect many-body localization in exchange-disordered isotropic spin chains. *New Journal of Physics*, 25(12):123002, 2023.

[156] Filiberto Ares, Sara Murciano, Eric Vernier, and Pasquale Calabrese. Lack of symmetry restoration after a quantum quench: an entanglement asymmetry study. *SciPost Physics*, 15(3):089, 2023.

[157] Jorge Tabanera-Bravo, Juan MR Parrondo, Massimiliano Esposito, and Felipe Barra. Thermalization and dephasing in collisional reservoirs. *Physical Review Letters*, 130(20):200402, 2023.

[158] Iman Marvian. Theory of quantum circuits with abelian symmetries. *arXiv preprint arXiv:2302.12466*, 2023.

[159] Bhupen Dabholkar and Fabien Alet. Ergodic and non-ergodic properties of disordered su (3) chains. *arXiv preprint arXiv:2403.00442*, 2024.

[160] Luis Pedro García-Pintos, Kishor Bharti, Jacob Bringewatt, Hossein Dehghani, Adam Ehrenberg, Nicole Yunger Halpern, and Alexey V Gorshkov. Estimation of Hamiltonian parameters from thermal states. *arXiv preprint arXiv:2401.10343*, 2024.

[161] Berislav Buča, Joseph Tindall, and Dieter Jaksch. Non-stationary coherent quantum many-body dynamics through dissipation. *Nature Communications*, 10(1):1730, 2019.

[162] Marko Medenjak, Berislav Buča, and Dieter Jaksch. Isolated heisenberg magnet as a quantum time crystal. *Phys. Rev. B*, 102:041117, Jul 2020.

[163] Marko Medenjak, Tomaž Prosen, and Lenart Zadnik. Rigorous bounds on dynamical response functions and time-translation symmetry breaking. *SciPost Physics*, 9(1):003, 2020.

[164] Koki Chinzei and Tatsuhiko N Ikeda. Time crystals protected by floquet dynamical symmetry in Hubbard models. *Physical Review Letters*, 125(6):060601, 2020.

[165] Sanjay Moudgalya, Nicolas Regnault, and B Andrei Bernevig. η-pairing in Hubbard models: From spectrum generating algebras to quantum many-body scars. *Physical Review B*, 102(8):085140, 2020.

[166] Arno Bohm, Yuval Ne'eman, and Asim Orhan Barut. *Dynamical Groups And Spectrum Generating Algebras*, volume 2. World Scientific, 1988.

[167] Bruno Gruber and Takaharu Otsuka. *Symmetries in science VII: spectrum-generating algebras and dynamic symmetries in physics*. Springer Science & Business Media, 2012.

[168] Joseph Tindall, C Sánchez Muñoz, Berislav Buča, and Dieter Jaksch. Quantum synchronisation enabled by dynamical symmetries and dissipation. *New Journal of Physics*, 22(1):013026, 2020.

[169] Berislav Buča and Dieter Jaksch. Dissipation induced nonstationarity in a quantum gas. *Physical Review Letters*, 123(26):260401, 2019.

[170] Berislav Buča. Out-of-time-ordered crystals and fragmentation. *Physical Review Letters*, 128(10):100601, 2022.

[171] Berislav Buca, Archak Purkayastha, Giacomo Guarnieri, Mark T Mitchison, Dieter Jaksch, and John Goold. Quantum many-body attractors. *arXiv preprint arXiv:2008.11166*, 2020.

[172] Eric J Heller. Bound-state eigenfunctions of classically chaotic Hamiltonian systems: scars of periodic orbits. *Physical Review Letters*, 53(16):1515, 1984.

[173] Christopher J Turner, Alexios A Michailidis, Dmitry A Abanin, Maksym Serbyn, and Zlatko Papić. Weak ergodicity breaking from quantum many-body scars. *Nature Physics*, 14(7):745–749, 2018.

[174] Maksym Serbyn, Dmitry A Abanin, and Zlatko Papić. Quantum many-body scars and weak breaking of ergodicity. *Nature Physics*, 17(6):675–685, 2021.

[175] Sanjay Moudgalya, B Andrei Bernevig, and Nicolas Regnault. Quantum many-body scars and Hilbert space fragmentation: a review of exact results. *Reports on Progress in Physics*, 85(8):086501, 2022.

[176] Nicholas O'Dea, Fiona Burnell, Anushya Chandran, and Vedika Khemani. From tunnels to towers: Quantum scars from lie algebras and q-deformed lie algebras. *Physical Review Research*, 2(4):043305, 2020.

[177] Brian C Hall. *Lie groups, Lie algebras, and representations*. Springer, 2013.

[178] Rutwig Campoamor-Stursberg and Michel Rausch De Traubenberg. *Group theory in physics: a practitioner's guide*. World Scientific, 2019.

[179] Hal Tasaki. The Hubbard model-an introduction and selected rigorous results. *Journal of Physics: Condensed Matter*, 10(20):4353, 1998.

[180] Shoucheng Zhang. Pseudospin symmetry and new collective modes of the hubbard model. *Physical Review Letters*, 65(1):120, 1990.

[181] Dorota Jakubczyk and Paweł Jakubczyk. On the su (2)× su (2) symmetry in the Hubbard model. *Open Physics*, 10(4):906–912, 2012.

[182] Ivan V Protopopov, Wen Wei Ho, and Dmitry A Abanin. Effect of su (2) symmetry on many-body localization and thermalization. *Physical Review B*, 96(4):041122, 2017.

[183] Brian Swingle. Unscrambling the physics of out-of-time-order correlators. *Nat. Phys.*, 14(10):988–990, 2018.

[184] Daniel A. Roberts and Beni Yoshida. Chaos and complexity by design. *Journal of High Energy Physics*, 2017(4):121, Apr 2017.

[185] Adam R. Brown and Leonard Susskind. Second law of quantum complexity. *Phys. Rev. D*, 97:086015, Apr 2018.

[186] Albert Einstein, Boris Podolsky, and Nathan Rosen. Can quantum-mechanical description of physical reality be considered complete? *Physical Review*, 47(10):777, 1935.

[187] Terry Rudolph and Shashank Soyuz Virmani. The two-qubit singlet/triplet measurement is universal for quantum computing given only maximally-mixed initial states. *Nature Communications*, 14(1):7800, 2023.

[188] Michael H Freedman, Matthew B Hastings, and Modjtaba Shokrian Zini. Symmetry protected quantum computation. *Quantum*, 5:554, 2021.

[189] Stefan Trotzky, Yu-Ao Chen, Andreas Flesch, Ian P McCulloch, Ulrich Schollwöck, Jens Eisert, and Immanuel Bloch. Probing the relaxation towards equilibrium in an isolated strongly correlated one-dimensional bose gas. *Nat. Phys.*, 8(4):325–330, 2012.

[190] Tim Langen, Remi Geiger, Maximilian Kuhnert, Bernhard Rauer, and Joerg Schmiedmayer. Local emergence of thermal correlations in an isolated quantum many-body system. *Nat. Phys.*, 9(10):640–643, 2013.

[191] Yijun Tang, Wil Kao, Kuan-Yu Li, Sangwon Seo, Krishnanand Mallayya, Marcos Rigol, Sarang Gopalakrishnan, and Benjamin L Lev. Thermalization near integrability in a dipolar quantum newton's cradle. *Phys. Rev. X*, 8(2):021030, 2018.

[192] Kevin A Landsman, Caroline Figgatt, Thomas Schuster, Norbert M Linke, Beni Yoshida, Norm Y Yao, and Christopher Monroe. Verified quantum information scrambling. *Nature*, 567(7746):61–65, 2019.

[193] Franz Mandl. *Statistical Physics*. Wiley, 1971.

[194] Chen Ning Yang. η pairing and off-diagonal long-range order in a Hubbard model. *Physical Review Letters*, 63(19):2144, 1989.

[195] ML Metha, JM Normand, and V Gupta. A property of the structure constants of finite dimensional compact simple lie algebras. *Commun. Math. Phys.*, 90(1):69–78, 1983.

[196] Richard P Stanley. Enumerative combinatorics volume 1 second edition. *Cambridge studies in advanced mathematics*, 2011.

[197] Eliahu Cohen, Tobias Hansen, and Nissan Itzhaki. From entanglement witness to generalized catalan numbers. *Scientific Reports*, 6(1):1–10, 2016.

[198] William Fulton and Joe Harris. *Representation Theory: A First Course*. Springer, New York, New York, 2004.

Appendices

Appendix A

Appendices for "Review of noncommuting charges"

A.1 Schur's lemma implies degeneracy of Hamiltonians that have non-Abelian symmetries

Consider a quantum system associated with a Hilbert space $\mathcal{H}$. Let $H^{\rm tot}$ denote the Hamiltonian, which has a symmetry associated with a Lie group $\mathcal{G}$. Let k label the irreducible representations (irreps) of $\mathcal{G}$. For example, $\mathcal{G} = {\rm SU}(2)$ has irreps labeled by $s = 0, 1/2, 1, \ldots$ A corollary of Schur's lemma states that [50, p. 9]

$$\mathcal{H} = \bigoplus_k \mathcal{H}_k \otimes \mathcal{M}_k \tag{A.1}$$

$\mathcal{H}_k$ denotes a representation space. The multiplicity space $\mathcal{M}_k$ has a dimensionality equal to irrep k's dimension.

Correspondingly, $H^{\rm tot}$ decomposes as [198, Sec. 3.2.3]

$$H^{\rm tot} = \bigoplus_k E_k \mathbb{1}_k. \tag{A.2}$$

E_k denotes an eigenenergy. $\mathbb{1}_k$ denotes the identity operator acting on the multiplicity space $\mathcal{M}_k$. If $\mathcal{G}$ is non-Abelian, then some of the irreps k have dimensionalities > 1. Consequently, some $\mathbb{1}_k$'s act on multidimensional subspaces $\mathcal{M}_k$. Those $\mathcal{M}_k$'s are degenerate eigenspaces of $H^{\rm tot}$.

Appendix B

Appendices for "Bridging to experiments and many-body physics"

B.1 The Killing form induces a metric on every simple Lie algebra.

Here, we prove a claim made in Sec. II.A of the main text: The Killing form induces a metric on every simple Lie algebra. The proof relies on background material reviewed in Sec. II.B of the main text.

First, we need to prove that every inner product defines a metric. An inner product on a vector space V over the field $\mathbb{F}$ is a function $\langle \cdot, \cdot \rangle : V \times V \to \mathbb{F}$ that satisfies the following three properties for all $u, v, w \in V$ and $\alpha \in \mathbb{F}$: (1) conjugate symmetry $\langle u, v \rangle = \overline{\langle v, u \rangle}$, (2) linearity in the first argument $\langle \alpha u + v, w \rangle = \alpha \langle u, w \rangle + \langle v, w \rangle$, and (3) positive-definiteness $\langle v, v \rangle \geq 0$ with equality if and only if $v = 0$.

Given an inner product $\langle \cdot, \cdot \rangle$, we can define a metric (or distance function) $d : V \times V \to \mathbb{R}$ as follows:

$$d(u, v) = \sqrt{\langle u - v, u - v \rangle} \tag{B.1}$$

We need to prove that d satisfies the four properties of a metric. The first is non-negativity

$$d(u, v) \geq 0.$$

This follows from the positive-definiteness of the inner product. The second is the identity of indiscernible,

$$d(u, v) = 0 \iff u = v.$$

This also follows from the positive-definiteness of the inner product since $\langle u-v, u-v\rangle = 0$ if and only if $u = v$. The third is symmetry,

$$d(u, v) = d(v, u).$$

This follows from the symmetry property of the inner product $d(u, v) = \sqrt{\langle u - v, u - v\rangle} = \sqrt{\langle v - u, v - u\rangle} = d(v, u)$. The last is the triangle inequality

$$d(u, w) \leq d(u, v) + d(v, w).$$

To prove this property holds, we use the Cauchy-Schwarz inequality:

$$|\langle u|v\rangle|^2 \leq \langle u|u\rangle \cdot \langle v|v\rangle \,. \tag{B.2}$$

To prove the triangle inequality we first substitute $u - w = (u - v) + (v - w)$ in the expression for $d(u, w)^2$,

$$\begin{aligned} d(u, w)^2 &= \langle u - w, u - w\rangle & \text{(B.3)}\\ &= \langle (u - v) + (v - w), (u - v) + (v - w). & \text{(B.4)} \end{aligned}$$

We use the inner product's linearity to expand and the conjugate symmetry property to simplify the expression,

$$\begin{aligned} d(u, w)^2 &= \langle u - v, u - v\rangle + \langle u - v, v - w\rangle + \langle v - w, u - v\rangle + \langle v - w, v - w\rangle & \text{(B.5)}\\ &= \langle u - v, u - v\rangle + 2\,\mathrm{Re}\{\langle u - v, v - w\rangle\} + \langle v - w, v - w\rangle & \text{(B.6)} \end{aligned}$$

Note that $2\,\mathrm{Re}\{\langle u - v, v - w\rangle\} \leq 2|\langle u - v, v - w\rangle|$. We then apply the Cauchy-Schwarz inequality on the right-hand side:

$$2|\langle u - v, v - w\rangle| \leq 2\sqrt{\langle u - v, u - v\rangle}\sqrt{\langle v - w, v - w\rangle}. \tag{B.7}$$

We have

$$d(u, w)^2 \leq \langle u - v, u - v\rangle + \langle v - w, v - w\rangle + 2\sqrt{\langle u - v, u - v\rangle}\sqrt{\langle v - w, v - w\rangle} \tag{B.8}$$

The right-hand side is a perfect square ($a^2 + b^2 + 2ab = (a + b)^2$),

$$d(u, w)^2 \leq (\langle u - v, u - v\rangle + \langle v - w, v - w\rangle)^2 d(u, w) \quad \leq \langle u - v, u - v\rangle + \langle v - w, v - w\rangle d(u, w) \leq d(u, v) \tag{B.9}$$

Which concludes our proof.

Since d satisfies all the properties of a metric, we have shown that every inner product defines a metric. Therefore, proving that the Killing form induces an inner product suffices. On a simple Lie algebra, all symmetric bilinear forms equal each other to within a multiplicative constant [77]. The Killing form is one symmetric bilinear form; another is $\mathrm{Tr}(Q_\alpha Q_\beta)$. Hence $(Q_\alpha, Q_\beta) \propto \mathrm{Tr}(Q_\alpha Q_\beta) = \mathrm{Tr}\big(Q_\alpha^\dagger Q_\beta\big)$. The final equality follows from the charges' Hermiticity. The final expression is the Hilbert-Schmidt inner product. Hence the Killing form induces an inner product.

B.2 General Hamiltonian that transports $\mathfrak{su}(2)$ elements locally while conserving them globally

Section II.B of the main text illustrated how to construct Hamiltonians that transport $\mathfrak{su}(2)$ elements locally while conserving them globally. The illustration was not maximally general; we restricted a unitary U more than required, for pedagogy. We generalize the construction here. For clarity of presentation, we derive the charges' forms first (Supplementary Note B.2.1) and the ladder operators' forms second (Supplementary Note B.2.2). We then construct the two-body Hamiltonian $H^{(j,j')}$ and a three-body Hamiltonian (Supplementary Note B.2.3).

B.2.1 Preferred basis of charges for $\mathfrak{su}(2)$

The conventional Cartan-Weyl basis contains the Hermitian operator

$$Q_1 = \sigma_z. \tag{B.10}$$

To identify the next Cartan-Weyl basis, we invoke a general unitary $U \in \mathrm{SU}(2)$. In the Euler parameterization,

$$U = e^{i\sigma_z \phi_1/2} e^{i\sigma_y \phi_2/2} e^{i\sigma_z \phi_3/2}, \tag{B.11}$$

wherein $\phi_1 \in [0, 2\pi)$, $\phi_2 \in [0, \pi]$, and $\phi_3 \in [0, 2\pi)$. We restrict this general unitary to a U_i that maps Q_2 to a Killing-orthogonal charge $Q_2 = U_\mathrm{i}^\dagger Q_1 U_\mathrm{i}$. For $X, Y \in (D)$, the Killing form evaluates to $(X, Y) = \mathrm{Tr}(XY)$ [77]. Hence the Killing form between the charges is

$$0 = \left(U_\mathrm{i}^\dagger Q_1 U_\mathrm{i},\, Q_1\right) = \mathrm{Tr}\left(U_\mathrm{i}^\dagger Q_1 U_\mathrm{i} Q_1\right) = 2\cos\left(\phi_2^{(\mathrm{i})}\right). \tag{B.12}$$

The superscript (i), here and below, labels a parameter as belonging to $U_{\rm i}$. The equation, with $\phi_2^{(\rm i)} \in [0, \pi]$, implies that $\phi_2^{(\rm i)} = \pi/2$. The unitary and charge assume the forms

$$U_{\rm i} = e^{i\sigma_z \phi_1^{(\rm i)}/2} e^{i\sigma_y \pi/4} e^{i\sigma_z \phi_3^{(\rm i)}/2} \quad \text{and} \quad Q_2 = \cos\left(\phi_3^{(\rm i)}\right)\sigma_x + \sin\left(\phi_3^{(\rm i)}\right)\sigma_y. \tag{B.13}$$

Having identified the second charge, we identify the final one. We transform Q_1 with a unitary $U_{\rm ii} \in {\rm SU}(2)$ such that $Q_3 = U_{\rm ii}^\dagger Q_1 U_{\rm ii}$ is Killing-orthogonal to the first two charges. The first orthogonality constraint has the form of Eq. (B.12), except that a (ii) replaces the superscript (i). The second orthogonality constraint is

$$0 = {\rm Tr}\left(U_{\rm ii}^\dagger Q_1 U_{\rm ii},\, Q_2\right) = {\rm Tr}\left(U_{\rm ii}^\dagger Q_1 U_{\rm ii} Q_2\right) = 2\cos\left(\phi_3^{(\rm i)} - \phi_3^{(\rm ii)}\right). \tag{B.14}$$

Hence $\phi_3^{(\rm ii)} = \phi_3^{(\rm i)} + \pi\left(n^{(\rm ii)} - \frac{1}{2}\right)$, wherein $n^{(\rm ii)} \in \mathbb{Z}$. Hence $U_{\rm ii}$ and Q_3 have the forms

$$U_{\rm ii} = e^{i\sigma_z \phi_1^{(\rm ii)}/2} e^{i\sigma_y \pi/4} e^{i\sigma_z [\phi_3^{(\rm i)} + \pi(n - \frac{1}{2})]/2} \quad \text{and} \tag{B.15}$$

$$Q_3 = (-1)^{n^{(\rm ii)}} \left[\sin\left(\phi_3^{(\rm i)}\right)\sigma_x - \cos\left(\phi_3^{(\rm i)}\right)\sigma_y\right]. \tag{B.16}$$

Equations (B.16), (B.13), and (B.10) specify the preferred basis of charges for $\mathfrak{su}(2)$.

B.2.2 General ladder operators for $\mathfrak{su}(2)$

The conventional Cartan-Weyl basis contains operators that raise and lower σ_z:

$$L_{\pm 1} = \sigma_{\pm z} = \frac{1}{2}(\sigma_x \pm i\sigma_y). \tag{B.17}$$

Conjugation with $U_{\rm i}$ yields the ladder operators for Q_2, and conjugation with $U_{\rm ii}$ yields the ladder operators for Q_3:

$$L_{\pm 2} = U_{\rm i}^\dagger L_{\pm 1} U_{\rm i} = \frac{-e^{\mp i\phi_1^{(\rm i)}}}{2}[\sigma_z \pm i(\sin\{\phi_3^{(\rm i)}\}\sigma_x - \cos\{\phi_3^{(\rm i)}\}\sigma_y)], \quad \text{and} \tag{B.18}$$

$$L_{\pm 3} = U_{\rm ii}^\dagger L_{\pm 1} U_{\rm ii} = \frac{-e^{\mp i\phi_1^{(\rm ii)}}}{2}\left\{\sigma_z \mp i(-1)^{n^{(\rm ii)}}\left[\cos\left(\phi_3^{(\rm i)}\right)\sigma_x + \sin\left(\phi_3^{(\rm i)}\right)\sigma_y\right]\right\}. \tag{B.19}$$

B.2.3 Two-body and three-body Hamiltonians for $\mathfrak{su}(2)$

To form $H^{(j,j')}$, we substitute for the ladder operators from Eqs. (B.17) and (B.18) into Eq. (12). We require that $H^{(j,j')}$ conserve each global charge, imposing Eq. (14). This equation holds, algebra reveals, if and only if the hopping frequencies $J_\alpha^{(j,j')}$ equal each other. The Hamiltonian simplifies to Eq. (15). The final expression does not depend on our choice of $\phi_k^{(\mathrm{i})}$, $\phi_k^{(\mathrm{ii})}$, or $n^{(\mathrm{i})}$.

Let us construct a Hamiltonian $H^{(j,j',j'')}$ that transfers $\mathfrak{su}(2)$ charges between three sites—j, j', and j''—while conserving the charges globally. We multiply three two-body Hamiltonians together cyclically:

$$H^{(j,j',j'')} \propto H^{(j,j')} H^{(j',j'')} H^{(j'',j)} \tag{B.20}$$

We substitute in from Eq. (13), the $H^{(j,j')}$ expression in which the hopping frequencies have not yet been restricted. The frequencies can assume different values, when $[H^{(j,j',j'')}, Q_\alpha^{\mathrm{tot}}] = 0$, than when $[H^{(j,j')}, Q_\alpha^{\mathrm{tot}}] = 0$. Imposing the first commutator equation yields four sets of solutions for the J_α's, when $J_\alpha \neq 0$ for all α:

1. $J_1 = J_2 = J_3$, $J_4 = J_5 = J_6$, and $J_7 = J_8 = J_9$.
2. $J_1 = J_2 = -J_3$, $J_4 = J_5 = -J_6$, and $J_7 = J_8 = -J_9$.
3. $J_1 = J_2 = \frac{-J_3}{2}$, $J_4 = J_5 = \frac{-J_6}{2}$, and $J_7 = J_8 = \frac{-J_9}{2}$.
4. $\frac{J_2}{J_1} = \frac{J_5}{J_4} = \frac{J_8}{J_7}$, $J_1 + J_2 = -J_3$, $J_4 + J_5 = -J_6$, and $J_7 + J_8 = -J_9$.

We have omitted superscripts for conciseness. The four solutions lead to distinct Hamiltonians.[1]

For concreteness, we detail the first set of solutions, item 1. We collect three of the frequencies to simplify notation: $J^{j,j',j''} = J_1^{(j,j')} J_4^{(j',j'')} J_7^{(j',j'')}$. Substituting the J_α's into the Hamiltonian (B.20) yields

$$\begin{aligned} H^{(j,j',j'')} \propto J^{(j,j',j'')} \Big\{ & 3\mathbb{1}\mathbb{1}\mathbb{1} - 2\left(H^{(j,j')} - H^{(j'',j)} + H^{(j',j'')}\right) \\ & + i[(\sigma_x\sigma_y\sigma_z + \sigma_y\sigma_z\sigma_x + \sigma_z\sigma_x\sigma_y) - (\sigma_z\sigma_y\sigma_x + \sigma_x\sigma_z\sigma_y + \sigma_y\sigma_x\sigma_z)\}. \end{aligned} \tag{B.21}$$

[1] However, each solution contains a little redundancy: Consider picking one of the four solutions, then cycling the indices in $(1,2,3)$ identically to the indices in $(4,5,6)$ and to the indices in $(7,8,9)$. The resulting J_α's specify a Hamiltonian identical to the original.

We have omitted some superscripts to simplify notation. The first term is trivial, terms 2-4 are two-body, and each of terms 1-4 conserves each $Q_\alpha^{\rm tot}$. Subtracting these terms off yields the solely three-body Hamiltonian, Eq. (18). We have absorbed the i into the coefficient such that $J^{j,j',j''} \in \mathbb{R}$.

B.3 Simple form to which a two-body Hamiltonian may collapse

In the $\mathfrak{su}(2)$ example, $H^{(j,j')}$ collapsed to the simple form (16). The $\mathfrak{su}(3)$ $H^{(j,j')}$ collapses to an analogous form, we shown in Sec. II.D. This form generalizes to

$$\sum_{\alpha=1}^{c} Q_\alpha^{(j)} Q_\alpha^{(j')}. \tag{B.22}$$

This expression generally conserves noncommuting charges globally, and transport the charges locally, as proved below. However, the expression's equality with a two-body Hamiltonian that clearly, overtly transports local charges from site to site is proved only in the $\mathfrak{su}(2)$ and $\mathfrak{su}(3)$ examples.

Proposition 2. *Consider any Lie algebra whose structure constants have the antisymmetry property*

$$f_{\alpha\beta}^{\gamma} = -f_{\gamma\beta}^{\alpha}. \tag{B.23}$$

A two-body Hamiltonian of the form (B.22) *conserves the algebra's elements globally.*

Every compact semisimple Lie algebra has such structure constants [195].

Proof. First, we substitute from Eq. (B.22) into the conservation law. Then, we invoke the commutator's linearity and the arguments' tensor-product forms:

$$0 = \left[H^{(j,j')}, Q_\alpha^{\rm tot} \right] = \left[\sum_{\beta=1}^{c} Q_\beta^{(j)} Q_\beta^{(j')}, Q_\alpha^{(j)} \otimes \mathbb{1}^{(j')} + \mathbb{1}^{(j)} \otimes Q_\alpha^{(j')} \right] \tag{B.24}$$

$$= \sum_{\beta=1}^{c} \left(\left[Q_\beta^{(j)} Q_\beta^{(j')}, Q_\alpha^{(j)} \otimes \mathbb{1}^{(j')} \right] + \left[Q_\beta^{(j)} Q_\beta^{(j')}, \mathbb{1}^{(j)} \otimes Q_\alpha^{(j')} \right] \right) \tag{B.25}$$

$$= \sum_{\beta=1}^{c} \left(\left[Q_\beta^{(j)}, Q_\alpha^{(j)} \right] Q_\beta^{(j')} + Q_\beta^{(j)} \left[Q_\beta^{(j')}, Q_\alpha^{(j')} \right] \right). \tag{B.26}$$

Let $f^{\gamma}_{\alpha\beta}$ denote the Lie algebra's structure constants. The f's dictate how a Lie bracket decomposes as a linear combination of the algebra's elements:

$$[Q_\alpha,\, Q_\beta] = \sum_{\gamma=1}^{c} f^{\gamma}_{\alpha\beta} Q_\gamma. \tag{B.27}$$

We substitute into Eq. (B.26), then pull the sums and constants out front:

$$0 = \sum_{\beta=1}^{c} \left[\left(\sum_{\gamma=1}^{c} f^{\gamma}_{\beta\alpha} Q^{(j)}_{\gamma} \right) Q^{(j')}_{\beta} + Q^{(j)}_{\beta} \left(\sum_{\gamma=1}^{c} f^{\gamma}_{\beta\alpha} Q^{(j')}_{\gamma} \right) \right] = \sum_{\beta,\gamma=1}^{c} f^{\gamma}_{\beta\alpha} \left(Q^{(j)}_{\gamma} Q^{(j')}_{\beta} + Q^{(j)}_{\beta} Q^{(j')}_{\gamma} \right). \tag{B.28}$$

The final equation holds if $f^{\gamma}_{\beta\alpha} = -f^{\beta}_{\gamma\alpha}$. Consider relabeling the index α as β and vice versa. Equation (B.23) results. □

Having proved that the simple operator (B.22) conserves noncommuting charges globally, we prove that it transports charges locally.

Proposition 3. *The simple two-body Hamiltonian* (B.22) *transports the charges* Q_α *locally.*

Proof. Charge Q_α is transported locally if it satisfies Eq. (3), having a nonzero commutator

$$\left[H^{(j,j')}, Q^{(j)}_{\alpha} \right] = \left[\sum_{\beta=1}^{c} Q^{(j)}_{\beta} Q^{(j')}_{\beta}, Q^{(j)}_{\alpha} \right] = \sum_{\beta=1}^{c} \left[Q^{(j)}_{\beta}, Q^{(j)}_{\alpha} \right] Q^{(j')}_{\beta} = \sum_{\beta,\gamma=1}^{c} f^{\gamma}_{\beta\alpha}\, Q^{(j)}_{\gamma} Q^{(j')}_{\beta}. \tag{B.29}$$

The final expression vanishes if Q_α commutes with all the other charges Q_γ in the preferred basis. If a Lie algebra has a basis of which one element commutes with the others, the algebra is Abelian, by definition [77]. We assume that the algebra $\mathcal{A}$ is non-Abelian (Sec. II.A of the main text). Therefore, the right-hand side of (B.29) is nonzero, and the Hamiltonian transports the charges locally. □

B.4 Proof of Proposition 1

Proposition 1 states that the algebra $\mathcal{A}$ has an integer ratio c/r, wherein c denotes the algebra's dimension and r denotes the rank.

Proof. For every finite-dimensional complex Lie algebra, there exists a corresponding connected Lie group that is unique to within finite coverings. The Lie algebra has the same dimension and rank as each of the corresponding Lie groups. Thus, if Proposition 1 holds for all semisimple Lie groups, it holds for all semisimple Lie algebras. We prove the group claim.

Every Lie group has a maximal torus $\mathbb{T}^r$, which is the group generated by a Cartan subalgebra of the Lie algebra. The torus' dimensionality equals the group's rank, r. A torus is an r-fold Cartesian product of $\mathbb{S}^1$ manifolds [equivalently, of the group U(1)]. Quotienting out the torus' action from the Lie group yields a finite-dimensional coset space. Every finite-dimensional coset space's dimensionality is a positive integer $n \in \mathbb{Z}_{>0}$. Thus, the semisimple Lie group's dimension is $c = rn$. □

B.5 Mathematical details: Construction of a two-body Hamiltonian that transports $\mathfrak{su}(3)$ elements locally while conserving them globally

Section II.D illustrated the Hamiltonian-construction prescription with $\mathfrak{su}(3)$. We flesh out the explanation here. Appendix B.5.1 reviews the conventional Cartan-Weyl basis for $\mathfrak{su}(3)$. Appendix B.5.2 identifies the preferred basis of charges for $\mathfrak{su}(3)$. Appendix B.5.3 presents the ladder operators from which we construct a Hamiltonian.

B.5.1 Conventional Cartan-Weyl basis for $\mathfrak{su}(3)$

$\mathfrak{su}(3)$ has dimension $c = 8$ and rank $r = 2$. The conventional Cartan-subalgebra generators are denoted by $t_z = \tau_3/2$ and $y = \tau_8/\sqrt{3}$, wherein τ_3 and τ_8 denote Gell-mann matrices [82]. These generators, in the three-dimensional representation of $\mathfrak{su}(3)$, manifest as

$$T_z = \frac{1}{2}\begin{bmatrix} 1 & 0 & 0 \\ 0 & -1 & 0 \\ 0 & 0 & 0 \end{bmatrix} \quad \text{and} \quad Y = \frac{1}{3}\begin{bmatrix} 1 & 0 & 0 \\ 0 & 1 & 0 \\ 0 & 0 & -2 \end{bmatrix}. \tag{B.30}$$

t_z and y are orthogonal relative to the Killing form. They (more precisely, rescaled versions of them) belong in our preferred basis of charges: $Q_1 \propto t_z$, and $Q_2 \propto y$.

These charges are raised and lowered by $c - r = 8 - 2 = 6$ ladder operators, $t_\pm = (\tau_1 \pm i\tau_2)/2$, $v_\pm = (\tau_4 \pm i\tau_5)/2$, and $u_\pm = (\tau_6 \pm i\tau_7)/2$. In the three-dimensional representation of $\mathfrak{su}(3)$, the ladder operators manifest as

$$T_+ = \frac{1}{2}\begin{bmatrix} 0 & 1 & 0 \\ 0 & 0 & 0 \\ 0 & 0 & 0 \end{bmatrix}, \quad T_- = \frac{1}{2}\begin{bmatrix} 0 & 0 & 0 \\ 1 & 0 & 0 \\ 0 & 0 & 0 \end{bmatrix}, \quad V_+ = \frac{1}{2}\begin{bmatrix} 0 & 0 & 1 \\ 0 & 0 & 0 \\ 0 & 0 & 0 \end{bmatrix}, \quad V_- = \frac{1}{2}\begin{bmatrix} 0 & 0 & 0 \\ 0 & 0 & 0 \\ 1 & 0 & 0 \end{bmatrix}, \tag{B.31}$$

$$U_+ = \frac{1}{2}\begin{bmatrix} 0 & 0 & 0 \\ 0 & 0 & 1 \\ 0 & 0 & 0 \end{bmatrix}, \quad \text{and} \quad U_- = \frac{1}{2}\begin{bmatrix} 0 & 0 & 0 \\ 0 & 0 & 0 \\ 0 & 1 & 0 \end{bmatrix}. \tag{B.32}$$

The ladder operators participate in the following commutation relations with the charges:

$$[t_z, t_\pm] = \pm t_\pm, \quad [y, t_\pm] = 0, \tag{B.33}$$

$$[t_z, v_\pm] = \pm\frac{1}{2} v_\pm, \quad [y, v_\pm] = \pm v_\pm \tag{B.34}$$

$$[t_z, u_\pm] = \mp\frac{1}{2} u_\pm, \quad \text{and} \quad [y, u_\pm] = \pm u_\pm. \tag{B.35}$$

These relations imply that (i) $t_\pm$ raises and lowers t_z, whereas (ii) $v_\pm$ raises or lowers both t_z and y, as does $u_\pm$. We can prove this physical significance easily: Let $L_\pm$ denote a ladder operator (a $t_\pm$, a $v_\pm$, or a $u_\pm$) that raises/lowers a charge Q. Let $|\psi\rangle$ denote a Q eigenstate associated with the eigenvalue q: $Q|\psi\rangle = q|\psi\rangle$. Consider operating on the state with the ladder operator: $L_\pm|\psi\rangle$. Suppose, for notational convenience, that, (i) if L_+ operates, q is not the greatest Q eigenvalue and (ii) if L_- operates, q is not the least Q eigenvalue. The resulting state is a Q eigenstate associated with the eigenvalue $q \pm a$, wherein $a = 1$ or $1/2$. To prove this claim, we operate on the new state with the charge: $Q(L_\pm|\psi\rangle)$. Invoking the appropriate commutation relation [Eqs. (B.33)-(B.35)] yields

$$QL_\pm|\psi\rangle = (L_\pm Q \pm L_\pm)|\psi\rangle = L_\pm(Q \pm a\mathbb{1})|\psi\rangle = L_\pm(q \pm a)|\psi\rangle = (q \pm a)L_\pm|\psi\rangle\,. \tag{B.36}$$

By Eqs. (B.33)-(B.36), $t_\pm$ raises/lowers the t_z charge by one quantum and preserves y. $u_\pm$ lowers/raises t_z by half a quantum and raises/lowers y by one quantum. $v_\pm$ raises/lowers each of t_z and y by one quantum.

Having reviewed the conventional Cartan-Weyl basis for $\mathfrak{su}(3)$, we dispense with the conventional notation (t_z, $t_\pm$, etc.). We revert to the notation introduced in the main text (Q_α and $L_{\pm\alpha}$).

B.5.2 Preferred basis of charges for $\mathfrak{su}(3)$

The first two charges appear in Eqs. (20). We construct two new charges from Q_1, Q_2, and a unitary $U \in \mathrm{SU}(2)$. The general form of such a U, appears, in the Euler parameterization, in Eq. (21). We constrain U with the Killing-orthogonality conditions (9), obtaining a unitary U_{i}. The transformed charges have the forms $Q_3 = U_{\mathrm{i}}^\dagger Q_1 U_{\mathrm{i}}$ and $Q_4 = U_{\mathrm{i}}^\dagger Q_2 U_{\mathrm{i}}$. The new charges are Killing-orthogonal to each other by unitarity: $0 = \mathrm{Tr}\left(\left[U_{\mathrm{i}}^\dagger Q_1 U_{\mathrm{i}}\right]\left[U_{\mathrm{i}}^\dagger Q_2 U_{\mathrm{i}}\right]\right) = \mathrm{Tr}\left(Q_1 Q_2\right) = 0$. Killing-orthogonality to the old charges, Eq. (20), with the form of the $\mathfrak{su}(D)$ Killing form [77], implies

$$0 = \mathrm{Tr}\left(\left[U_{\mathrm{i}}^\dagger Q_1 U_{\mathrm{i}}\right] Q_2\right) = -\cos(\phi_2)/3, \tag{B.37}$$

$$0 = \mathrm{Tr}\left(\left[U_{\mathrm{i}}^\dagger Q_1 U_{\mathrm{i}}\right] Q_1\right) = -\frac{1}{2\sqrt{3}}\cos(\phi_3 + \phi_5), \tag{B.38}$$

$$0 = \mathrm{Tr}\left(\left[U_{\mathrm{i}}^\dagger Q_2 U_{\mathrm{i}}\right] Q_2\right) = \frac{1}{2}\left[\cos(\phi_4) + \frac{1}{3}\right], \text{ and} \tag{B.39}$$

$$0 = \mathrm{Tr}\left(\left[U_{\mathrm{i}}^\dagger Q_2 U_{\mathrm{i}}\right] Q_1\right) = -\cos(\phi_6)/3. \tag{B.40}$$

Since $\phi_2, \phi_4, \phi_6 \in [0, \pi]$ and $\phi_3, \phi_5 \in [0, 2\pi)$, $\phi_2 = \frac{\pi}{2}$, $\phi_4 = \mathrm{acos}(-1/3)$, $\phi_6 = \frac{\pi}{2}$ and $\phi_5 = \pi(n - 1/2) - \phi_3$, for $n \in \{1, 2, 3, 4\}$.

Transforming Q_1 and Q_2 with a $U_{\mathrm{ii}} \in \mathrm{SU}(3)$ yields the charges Q_5 and Q_6, and transforming Q_1 and Q_2 with a $U_{\mathrm{iii}} \in \mathrm{SU}(3)$ yields Q_7 and Q_8. These last four charges are Killing-orthogonal to Q_1 and Q_2, like Q_3 and Q_4. So U_{ii} and U_{iii} share the form of U_{i}. However, parameters $a^{(\mathrm{ii})}$ and $b^{(\mathrm{ii})}$, or $a^{(\mathrm{iii})}$ and $b^{(\mathrm{iii})}$, replace the $a^{(\mathrm{i})}$ and $b^{(\mathrm{i})}$. The later unitaries' parameters are more constrained than the U_{i} parameters. Similarly, Q_5 through Q_8 share the forms of Q_3 and Q_1, apart from their more-constrained parameters.

Evaluating the restrictions on all the charges simultaneously will prove useful. First, the conditions for Q_5 to be orthogonal to Q_3 and Q_4 are

$$0 = \mathrm{Tr}(Q_5 Q_3) \propto (-1)^{n^{(\mathrm{i})}+n^{(\mathrm{ii})}} \cos\left(a^{(\mathrm{i})} - a^{(\mathrm{ii})} - b^{(\mathrm{i})} + b^{(\mathrm{ii})}\right) + \cos\left(a^{(\mathrm{i})} - a^{(\mathrm{ii})}\right) + \cos\left(b^{(\mathrm{i})} - b^{(\mathrm{ii})}\right) \tag{B.41}$$

$$0 = \mathrm{Tr}(Q_5 Q_4) \propto (-1)^{n^{(\mathrm{i})}+n^{(\mathrm{ii})}} \sin\left(a^{(\mathrm{i})} - a^{(\mathrm{ii})} - b^{(\mathrm{i})} + b^{(\mathrm{ii})}\right) - \sin\left(a^{(\mathrm{i})} - a^{(\mathrm{ii})}\right) + \sin\left(b^{(\mathrm{i})} - b^{(\mathrm{ii})}\right). \tag{B.42}$$

The orthogonality conditions for Q_6 impose the same constraints, since $\mathrm{Tr}(Q_6 Q_3) \propto \mathrm{Tr}(Q_5 Q_4)$ and $\mathrm{Tr}(Q_6 Q_4) \propto \mathrm{Tr}(Q_5 Q_3)$ (as can be checked explicitly). Similarly, the or-

thogonality conditions on Q_7 evaluate to

$$0 = \mathrm{Tr}(Q_7 Q_3) \propto (-1)^{n^{(\mathrm{i})}+n^{(\mathrm{iii})}} \cos\!\left(a^{(\mathrm{i})} - a^{(\mathrm{iii})} - b^{(\mathrm{i})} + b^{(\mathrm{iii})}\right) + \cos\!\left(a^{(\mathrm{i})} - a^{(\mathrm{iii})}\right) + \cos\!\left(b^{(\mathrm{i})} - b^{(\mathrm{iii})}\right), \tag{B.43}$$

$$0 = \mathrm{Tr}(Q_7 Q_4) \propto (-1)^{n^{(\mathrm{i})}+n^{(\mathrm{iii})}} \sin\!\left(a^{(\mathrm{i})} - a^{(\mathrm{iii})} - b^{(\mathrm{i})} + b^{(\mathrm{iii})}\right) - \sin\!\left(a^{(\mathrm{i})} - a^{(\mathrm{iii})}\right) + \sin\!\left(b^{(\mathrm{i})} - b^{(\mathrm{iii})}\right), \tag{B.44}$$

$$0 = \mathrm{Tr}(Q_7 Q_5) \propto (-1)^{n^{(\mathrm{ii})}+n^{(\mathrm{iii})}} \cos\!\left(a^{(\mathrm{ii})} - a^{(\mathrm{iii})} - b^{(\mathrm{ii})} + b^{(\mathrm{iii})}\right) + \cos\!\left(a^{(\mathrm{ii})} - a^{(\mathrm{iii})}\right) + \cos\!\left(b^{(\mathrm{ii})} - b^{(\mathrm{iii})}\right), \tag{B.45}$$

$$0 = \mathrm{Tr}(Q_7 Q_6) \propto (-1)^{n^{(\mathrm{ii})}+n^{(\mathrm{iii})}} \sin\!\left(a^{(\mathrm{ii})} - a^{(\mathrm{iii})} - b^{(\mathrm{ii})} + b^{(\mathrm{iii})}\right) - \sin\!\left(a^{(\mathrm{ii})} - a^{(\mathrm{iii})}\right) + \sin\!\left(b^{(\mathrm{ii})} - b^{(\mathrm{iii})}\right). \tag{B.46}$$

The orthogonality conditions for Q_8 impose the same constraints [Eqs. (B.43)-(B.46)].

We now identify sets of $a^{(\ell)}, b^{(\ell)}$, and $n^{(\ell)}$ that are solutions for all six constraints, Eqs. (B.41)-(B.46). First, we define $x_{\ell m} := a^{(\ell)} - a^{(m)}$ and $y_{\ell m} := b^{(\ell)} - b^{(m)}$, for $(\ell, m) = (2,3), (2,4), (3,4)$. By these definitions, $x_{24} = x_{23} + x_{34}$, and $y_{24} = y_{23} + y_{34}$. Second, the values of the $n^{(\ell)}$ themselves are irrelevant. Only whether $n^{(\ell)} + n^{(m)}$ is even or odd matters. Only four unique possibilities for the $n^{(\ell)}$ exist: All the $n^{(\ell)} + n^{(m)}$ are even; or one $n^{(\ell)} + n^{(m)}$ is even, while the other two sums are odd. A solution can therefore be expressed in terms of just four quantities: x_{23}, x_{34}, y_{23}, and y_{34}. Each solution is periodic:

$$(x_{23}, x_{34}, y_{23}, y_{34}) \equiv (x_{23}, x_{34}, y_{23}, y_{34}) + (2\pi n, 2\pi n, 2\pi n, 2\pi n), \tag{B.47}$$

wherein $n \in \mathbb{Z}$. Therefore, we omit the $2\pi n$ when listing the solutions below.

First, suppose that all the $n^{(\ell)} + n^{(m)}$ are even. The constraints (B.41)-(B.46) admit of 18 solutions. The first ten are

$$\begin{aligned}(x_{23}, x_{34}, y_{23}, y_{34}) = &\left(0, \pm\frac{2\pi}{3}, \mp\frac{2\pi}{3}, \pm\frac{2\pi}{3}\right), \left(0, 0, \pm\frac{2\pi}{3}, \pm\frac{2\pi}{3}\right), \left(0, \pm\frac{2\pi}{3}, \pm\frac{2\pi}{3}, 0\right), \\ &\left(\pm\frac{2\pi}{3}, 0, \pm\frac{2\pi}{3}, \mp\frac{2\pi}{3}\right), \left(\pm\frac{2\pi}{3}, \pm\frac{2\pi}{3}, \pm\frac{2\pi}{3}, \pm\frac{2\pi}{3}\right).\end{aligned} \tag{B.48}$$

The next eight solutions are identical to the first eight, except that each $x_{\ell m}$ is swapped with the corresponding $y_{\ell m}$.

Second, $n^{(\mathrm{i})} + n^{(\mathrm{iii})}$ can be even while $n^{(\mathrm{i})} + n^{(\mathrm{ii})}$ and $n^{(\mathrm{ii})} + n^{(\mathrm{iii})}$ are odd. The constraints (B.41)-(B.46) admit of another 18 solutions. The first ten are

$$\begin{aligned}(x_{23}, x_{34}, y_{23}, y_{34}) = &\left(\pi, \pm\frac{\pi}{3}, \mp\frac{\pi}{3}, \pm\frac{\pi}{3}\right), \left(\pi, \pi, \pm\frac{\pi}{3}, \pm\frac{\pi}{3}\right), \left(\pi, \pm\frac{\pi}{3}, \pm\frac{\pi}{3}, \pi\right), \\ &\left(\pm\frac{\pi}{3}, \pi, \pm\frac{\pi}{3}, \mp\frac{\pi}{3}\right), \left(\pm\frac{\pi}{3}, \pm\frac{\pi}{3}, \pm\frac{\pi}{3}, \pm\frac{\pi}{3}\right).\end{aligned} \tag{B.49}$$

The next eight solutions are identical to the first eight, except that each $x_{\ell m}$ is swapped with the corresponding $y_{\ell m}$.

Third, $n^{(\mathrm{i})} + n^{(\mathrm{ii})}$ can be even while $n^{(\mathrm{i})} + n^{(\mathrm{iii})}$ and $n^{(\mathrm{ii})} + n^{(\mathrm{iii})}$ are odd. The constraints (B.41)-(B.46) admit of another 18 solutions. The first ten are

$$(x_{23}, x_{34}, y_{23}, y_{34}) = \left(0, \pm\frac{\pi}{3}, \pm\frac{2\pi}{3}, \pm\frac{\pi}{3}\right), \left(0, \pi, \pm\frac{2\pi}{3}, \mp\frac{\pi}{3}\right), \left(0, \mp\frac{\pi}{3}, \pm\frac{2\pi}{3}, \pi\right), \left(\pm\frac{2\pi}{3}, \pi, \pm\frac{2\pi}{3}, \pm\frac{\pi}{3}\right), \left(\pm\frac{2\pi}{3}, \mp\frac{\pi}{3}, \pm\frac{2\pi}{3}, \mp\frac{\pi}{3}\right). \tag{B.50}$$

The next eight solutions are identical to the first eight, except that each $x_{\ell m}$ is swapped with the corresponding $y_{\ell m}$.

Fourth, suppose that $n^{(\mathrm{ii})} + n^{(\mathrm{iii})}$ is even while $n^{(\mathrm{i})} + n^{(\mathrm{ii})}$ and $n^{(\mathrm{i})} + n^{(\mathrm{iii})}$ are odd. The constraints (B.41)-(B.46) admit of another 18 solutions. The first ten are

$$(x_{23}, x_{34}, y_{23}, y_{34}) = \left(\pi, \pm\frac{2\pi}{3}, \pm\frac{\pi}{3}, \pm\frac{2\pi}{3}\right), \left(\pi, 0, \pm\frac{\pi}{3}, \mp\frac{2\pi}{3}\right), \left(\pi, \mp\frac{2\pi}{3}, \pm\frac{\pi}{3}, 0\right), \left(\pm\frac{\pi}{3}, 0, \pm\frac{\pi}{3}, \pm\frac{2\pi}{3}\right), \left(\pm\frac{\pi}{3}, \mp\frac{2\pi}{3}, \pm\frac{\pi}{3}, \mp\frac{2\pi}{3}\right). \tag{B.51}$$

The next eight solutions are identical to the first eight, except that each $x_{\ell m}$ is swapped with the corresponding $y_{\ell m}$.

One can check explicitly that the tuple $(x_{23} + y_{23},\, x_{34} + y_{34})$ has three possible values: $(x_{23} + y_{23},\, x_{34} + y_{34}) = (\pm 2\pi/3,\, \pm 2\pi/3), (\pm 4\pi/3,\, \pm 4\pi/3), (\pm 2\pi/3,\, \mp 4\pi/3)$. Three sets of solutions follow. For example, the first set of solutions is $(x_{23} + y_{23},\, x_{34} + y_{34}) = (\pm 2\pi/3,\, \pm 2\pi/3)$. Hence

$$a^{(\mathrm{i})} - a^{(\mathrm{ii})} + b^{(\mathrm{i})} - b^{(\mathrm{ii})} = \pm\frac{2\pi}{3}, \qquad a^{(\mathrm{ii})} - a^{(\mathrm{iii})} + b^{(\mathrm{ii})} - b^{(\mathrm{iii})} = \pm\frac{2\pi}{3}, \tag{B.52}$$

$$a^{(\ell)} - a^{(m)} \in \left\{0, \frac{\pm\pi}{3}, \frac{\pm 2\pi}{3}, \pi\right\}, \quad \text{and} \quad b^{(\ell)} - b^{(m)} \in \left\{0, \frac{\pm\pi}{3}, \frac{\pm 2\pi}{3}, \pi\right\}, \tag{B.53}$$

for $(\ell, m) = (2, 3)$ and $(3, 4)$. All the solutions lead to the same Hamiltonian, Eq. (25).

B.5.3 Ladder operators for $\mathfrak{su}(3)$

The conventional Cartan-Weyl basis contains six ladder operators [Eqs. (24)]. We transform $L_{\pm 1,2,3}$ with the unitaries U_{i}, U_{ii}, and U_{iii} of Sec. B.5.2, to construct the rest of

the ladder operators: $L_{\pm4} = U_{\rm i}^\dagger L_{\pm1} U_{\rm i}$, $L_{\pm5} = U_{\rm i}^\dagger L_{\pm2} U_{\rm i}$, and $L_{\pm6} = U_{\rm i}^\dagger L_{\pm3} U_{\rm i}$. Substituting in for $L_{\pm1,2,3}$ from Eq. (24) yields

$$\begin{aligned} L_{\pm4} = \frac{ie^{\mp i\phi_1^{(\rm i)}}}{6}\Big\{ & 2i\cos\big(a^{(\rm i)} - b^{(\rm i)}\big)\tau_1 - 2i\sin\big(a^{(\rm i)} - b^{(\rm i)}\big)\tau_2 \\ & \mp \Big[\sqrt{3} \mp i(-1)^{n^{(\rm i)}}\Big]\Big[\cos\big(a^{(\rm i)}\big)\tau_4 - \sin\big(a^{(\rm i)}\big)\tau_5\Big] \\ & \pm \Big[\sqrt{3} \pm i(-1)^{n^{(\rm i)}}\Big]\Big[\cos\big(b^{(\rm i)}\big)\tau_6 - \sin\big(b^{(\rm i)}\big)\tau_7\Big] \mp \sqrt{3}(-1)^{n^{(\rm i)}}\tau_3 - \sqrt{3}i\tau_8\Big\}, \end{aligned} \tag{B.54}$$

$$\begin{aligned} L_{\pm5} = \frac{ie^{\mp\frac{i}{2}(\phi_3^{(\rm i)} + \phi_1^{(\rm i)})}}{6}\Big(& i\Big[\cos\big(a^{(\rm i)} - b^{(\rm i)}\big) - \sqrt{3}(-1)^{n^{(\rm i)}}\sin\big(a^{(\rm i)} - b^{(\rm i)}\big)\Big]\tau_1 \\ & - i\Big[\sin\big(a^{(\rm i)} - b^{(\rm i)}\big) + \sqrt{3}(-1)^{n^{(\rm i)}}\cos\big(a^{(\rm i)} - b^{(\rm i)}\big)\Big]\tau_2 \\ & \pm \frac{1}{2}\Big\{(-1)^{n^{(\rm i)}}\big[3\sin\big(a^{(\rm i)}\big) \pm i\cos\big(a^{(\rm i)}\big)\big] + \sqrt{3}e^{\pm ia^{(\rm i)}}\Big\}\tau_4 \\ & \pm \frac{1}{2}\Big\{(-1)^{n^{(\rm i)}}\big[3\cos\big(a^{(\rm i)}\big) \mp i\sin\big(a^{(\rm i)}\big)\big] \pm i\sqrt{3}e^{\pm ia^{(\rm i)}}\Big\}\tau_5 \\ & \pm \frac{1}{2}\Big\{(-1)^{n^{(\rm i)}}\big[3\sin\big(b^{(\rm i)}\big) \pm i\cos\big(b^{(\rm i)}\big)\big] - \sqrt{3}e^{\pm ib^{(\rm i)}}\Big\}\tau_6 \\ & \pm \frac{1}{2}\Big\{(-1)^{n^{(\rm i)}}\big[3\cos\big(b^{(\rm i)}\big) \mp i\sin\big(b^{(\rm i)}\big)\big] \mp i\sqrt{3}e^{\pm ib^{(\rm i)}}\Big\}\tau_7 \mp \sqrt{3}(-1)^{n^{(\rm i)}}\tau_3 + \sqrt{3}i\tau_8\Big), \end{aligned} \tag{B.55}$$

$$\begin{aligned} L_{\pm6} = \frac{ie^{\mp\frac{i}{2}\left(\phi_3^{(\rm i)} - \phi_1^{(\rm i)}\right)}}{6}\Big(& - i\Big[\cos\left(a^{(\rm i)} - b^{(\rm i)}\right) + \sqrt{3}(-1)^{n^{(\rm i)}}\sin\big(a^{(\rm i)} - b^{(\rm i)}\big)\Big]\tau_1 \\ & + i\Big[\sin\big(a^{(\rm i)} - b^{(\rm i)}\big) - \sqrt{3}(-1)^{n^{(\rm i)}}\cos\big(a^{(\rm i)} - b^{(\rm i)}\big)\Big]\tau_2 \\ & \mp \frac{1}{2}\Big\{(-1)^{n^{(\rm i)}}\big[3\sin\big(a^{(\rm i)}\big) \pm i\cos\big(a^{(\rm i)}\big)\big] - \sqrt{3}e^{ia^{(\rm i)}}\Big\}\tau_4 \\ & \mp \frac{1}{2}\Big\{(-1)^{n^{(\rm i)}}\big[3\cos\big(a^{(\rm i)}\big) \mp i\sin\big(a^{(\rm i)}\big)\big] \mp i\sqrt{3}e^{ia^{(\rm i)}}\Big\}\tau_5 \\ & \mp \frac{1}{2}\Big\{(-1)^{n^{(\rm i)}}\big[3\sin\big(b^{(\rm i)}\big) \pm i\cos\big(b^{(\rm i)}\big)\big] + \sqrt{3}e^{ib^{(\rm i)}}\Big\}\tau_6 \\ & \mp \frac{1}{2}\Big\{(-1)^{n^{(\rm i)}}\big[3\cos\big(b^{(\rm i)}\big) \mp i\sin\big(b^{(\rm i)}\big)\big] \pm i\sqrt{3}e^{ib^{(\rm i)}}\Big\}\tau_7 \mp \sqrt{3}(-1)^{n^{(\rm i)}}\tau_3 - \sqrt{3}i\tau_8\Big). \end{aligned} \tag{B.56}$$

$L_{\pm7}$, $L_{\pm8}$, and $L_{\pm9}$ have the same forms. However, (ii)'s replace the superscripts (i)'s. $L_{\pm10}$, $L_{\pm11}$, and $L_{\pm12}$ likewise have the same form, except that (iii)'s replace the (i)'s.

Appendix C

Appendices for "Noncommuting charges can increase average entanglement"

C.1 Analytic expressions for state-counting terms in microcanonical subspaces' Page curves

The Page curve (4.2) naturally splits into two terms, the state-counting term [$S(\langle\rho_A\rangle_{\mathcal{S}})$ from Eq. (4.4)] and the interference term. The interference term is exponentially small in $N_B - N_A$. Thus, if $N_A \ll N_B$, the Page curve approximately equals the state-counting term. As explained in Sec. 4.2, the state-counting term is easier to calculate than the Page curve is. We calculate the term in this appendix.

To recall the term's definition, consider a system restricted to a subspace $\mathcal{S}$ (e.g., a microcanonical or an AMC subspace) of dimensionality D. Denote by $\{|\psi_\ell\rangle\}$ any orthonormal basis for the subspace. Taking any pure state from that subspace and Haar-averaging it yields the maximally mixed state, $\langle\rho\rangle_{\mathcal{S}} = \frac{1}{D}\sum_\ell^D |\psi_\ell\rangle\langle\psi_\ell|$. Tracing out B yields $\langle\rho_A\rangle_{\mathcal{S}} \coloneqq \mathrm{Tr}_B(\langle\rho\rangle_{\mathcal{S}})$, whose entropy is the state-counting term:

$$S(\langle\rho_A\rangle_{\mathcal{S}}) = -\mathrm{Tr}(\langle\rho_A\rangle_{\mathcal{S}} \log \langle\rho_A\rangle_{\mathcal{S}}). \tag{C.1}$$

We calculate this term for microcanonical subspaces below. First, we introduce notation, a technical tool, and assumptions (App. C.1.1). We address the commuting-charge model in App. C.1.2 and the noncommuting-charge model in App. C.1.3.

C.1.1 Preliminaries

We use the following notation throughout this appendix. Denote by $X_a^{\rm tot} := \sum_{j=1}^N X_a$ the sum of the a qubits' X operators, and define $Y_a^{\rm tot}$ and $Z_a^{\rm tot}$ analogously. The a qubits' total-spin-squared operator, $\vec{S}_a^2 = [(X_a^{\rm tot})^2 + (Y_a^{\rm tot})^2 + (Z_a^{\rm tot})^2]/4$, has eigenvalues $s(s+1)$ (we set $\hbar = 1$). Denote by m the $Z_a^{\rm tot}/2$ eigenvalue. Denote by s_A subsystem A's spin quantum number, and denote by m_A subsystem A's magnetic spin quantum number. Define s_B and m_B analogously.

We will use Catalan's triangle, a triangular array of numbers related to the dimensionalities of qubit systems' Hilbert spaces [197, 196]. The element in row a and column b is

$$C_{a,b} = \frac{a-b+1}{a+1} \binom{a+b}{b}, \quad \text{for} \quad a \geq b. \tag{C.2}$$

The bound $a \geq b$ lends the array its triangular shape. Temporarily consider an N-qubit system that has quantum numbers s and m. For arbitrary m, $C_{\frac{N}{2}+s, \frac{N}{2}-s}$ equals the s eigenspace's dimensionality.

Throughout our approximations, we assume that parameters approximately equal their typical values: $m, s, m_A, s_A, m_B, s_B = \mathcal{O}\left(N^{-1/2}\right)$; and $N_A, N_B = \mathcal{O}\left(N\right)$. We assume also that the global system is large: $N \gg 1$.

C.1.2 Commuting-charge model's state-counting term

Appendix C.1.2 describes how the commuting-charge model is constrained in a microcanonical subspace. In App. C.1.2, we calculate the commuting-charge state-counting term exactly. How the exact formula scales with N is unclear. Therefore, we approximate the term to $\mathcal{O}(N^{-1})$ in App. C.1.2, to identify differences from the noncommuting-charge model.

Constraints on commuting-charge model in microcanonical subspace

The microcanonical subspace $\mathcal{C}_0$ parallels the noncommuting-charge model's $s = m = 0$ subspace. Let us specify quantitatively how the commuting-charge model is constrained. First, we introduce notation.

The local charges $C_{1,2,3}$ share four eigenstates, the maximally entangled *Bell states* [37]. They are, if $|\uparrow\rangle$ and $|\downarrow\rangle$ denote the Z eigenstates,

$$|\mathcal{B}_1\rangle \coloneqq \frac{1}{\sqrt{2}} \left(|\downarrow\rangle_a |\uparrow\rangle_b - |\uparrow\rangle_a |\downarrow\rangle_b \right), \quad |\mathcal{B}_2\rangle \coloneqq \frac{1}{\sqrt{2}} \left(|\downarrow\rangle_a |\downarrow\rangle_b - |\uparrow\rangle_a |\uparrow\rangle_b \right), \tag{C.3}$$

$$|\mathcal{B}_3\rangle \coloneqq \frac{1}{\sqrt{2}} \left(|\downarrow\rangle_a |\downarrow\rangle_b + |\uparrow\rangle_a |\uparrow\rangle_b \right), \quad \text{and} \quad |\mathcal{B}_4\rangle \coloneqq \frac{1}{\sqrt{2}} \left(|\downarrow\rangle_a |\uparrow\rangle_b + |\uparrow\rangle_a |\downarrow\rangle_b \right). \tag{C.4}$$

The Bell states correspond to the (C_1, C_2, C_3) eigenvalues $(-1,-1,-1)$, $(-1,1,1)$, $(1,-1,1)$, and $(1,1,-1)$, respectively. We will use a $\mathcal{C}_0$ basis formed from tensor products of single-site Bell states. For a given basis state, let P_k denote the number of sites in Bell state k.

Having specified notation, we use it to derive constraints on the system. The microcanonical subspace $\mathcal{C}_0$ is the eigenvalue-0 eigenspace of $C^{\text{tot}}_{1,2,3}$, by analogy with the noncommuting-charge $s = 0$ subspace. If the global system is in an eigenvalue-0 eigenstate of C^{tot}_1, then $P_1 + P_2 = P_3 + P_4 = \frac{N}{2}$. If the system is in an eigenvalue-0 eigenstate of C^{tot}_2, then $P_1 + P_3 = P_2 + P_4 = \frac{N}{2}$. If the system is in an eigenvalue-0 eigenstate of C^{tot}_3, then $P_1 + P_4 = P_2 + P_3 = \frac{N}{2}$. Together, these constraints imply

$$P_1 = P_2 = P_3 = P_4 = N/4 \,. \tag{C.5}$$

Since N is an integer, these constraints can be met if N is a multiple of 4, which we assume.

Exact expression for the commuting-charge state-counting term

We first calculate $\langle \rho_A \rangle_{\mathcal{C}_0}$, the reduced state of system A when the global system is maximally mixed. In addition to the definitions above, we invoke the "quadnomial" coefficient $\binom{n}{k_1,k_2,k_3,k_4} \coloneqq \frac{n!}{k_1!k_2!k_3!k_4!}$. Under the population restriction (C.5), the global system's Hilbert space is of dimensionality

$$D = \binom{N}{\frac{N}{4}, \frac{N}{4}, \frac{N}{4}, \frac{N}{4}}. \tag{C.6}$$

Denote by A_k the number of A sites in the Bell state $|\mathcal{B}_k\rangle$, and denote by B_k the number of B sites in $|\mathcal{B}_k\rangle$. The global system is restricted to a subspace of dimensionality

$$D_A = \binom{N_A}{A_1, A_2, A_3, A_4} \binom{N_B}{B_1, B_2, B_3, B_4} \tag{C.7}$$

$$= \binom{N_A}{\frac{N_A}{4} + m_1, \frac{N_A}{4} + m_2, \frac{N_A}{4} + m_3, \frac{N_A}{4} + m_4} \binom{N_B}{\frac{N_B}{4} - m_1, \frac{N_B}{4} - m_2, \frac{N_B}{4} - m_3, \frac{N_B}{4} - m_4}. \tag{C.8}$$

In accordance with Eq. (C.5), $A_k + B_k = N/4$. Furthermore, A is restricted to a subspace of dimensionality

$$d_A = \binom{N_A}{A_1, A_2, A_3, A_4} = \binom{N_A}{\frac{N_A}{4} + m_1, \frac{N_A}{4} + m_2, \frac{N_A}{4} + m_3, \frac{N_A}{4} + m_4}. \tag{C.9}$$

The global maximally mixed state is $\langle \rho \rangle_{\mathcal{C}_0} = \frac{1}{D} \sum_{\ell=1}^{D} |\psi_\ell\rangle\langle\psi_\ell|$; the sum runs over all the states in our basis for $\mathcal{C}_0$. Denote by $\{|A_1, A_2, A_3, A_4, i\rangle\}$ a basis for subsystem A's Hilbert space. The index i distinguishes basis states that share the same A_1, A_2, A_3, and A_4. Tracing out subsystem B yields

$$\langle \rho_A \rangle_{\mathcal{C}_0} = \frac{1}{D} \sum_{A_1, A_2, A_3, A_4, i} \frac{D_A}{d_A} |A_1, A_2, A_3, A_4, i\rangle\langle A_1, A_2, A_3, A_4, i| \,. \tag{C.10}$$

The $\frac{D_A}{d_A}$ equals the dimensionality of the subsystem-B subspace that is consistent with the subsystem-A populations A_1, A_2, A_3, and A_4. Taking the spectral decomposition, we calculate $\langle \rho_A \rangle_{\mathcal{C}_0}$'s entropy and so the state-counting term:

$$S(\langle \rho_A \rangle_{\mathcal{C}_0}) = - \sum_{A_1, A_2, A_3, A_4} \frac{D_A}{D} \log\left(\frac{D_A}{d_A D}\right) \tag{C.11}$$

$$= - \sum_{A_1, A_2, A_3, A_4} \binom{N_A}{A_1, A_2, A_3, A_4} \frac{\binom{N_B}{B_1, B_2, B_3, B_4}}{\binom{N}{\frac{N}{4}, \frac{N}{4}, \frac{N}{4}, \frac{N}{4}}} \log\left(\frac{\binom{N_B}{B_1, B_2, B_3, B_4}}{\binom{N}{\frac{N}{4}, \frac{N}{4}, \frac{N}{4}, \frac{N}{4}}}\right). \tag{C.12}$$

Closed-form approximation to the commuting-charge state-counting term

Let us approximate the $\frac{D_A}{D}$ in Eq. (C.11) as a Gaussian function. Via differentiation, we determine that $\log\left(\frac{D_A}{D}\right)$ maximizes at $m_k = 0$ for all k. We Taylor-expand $\log\left(\frac{D_A}{D}\right)$ around this maximum, keeping only terms larger than $\mathcal{O}\left(N^{-3/2}\right)$. For conciseness, we define $c \coloneqq \frac{2N}{N_A N_B} = O\left(\frac{1}{N}\right)$, $d \coloneqq \frac{1}{3}\left(\frac{8}{N_B^2} - \frac{8}{N_A^2}\right) = O\left(\frac{1}{N^2}\right)$, $f \coloneqq \frac{1}{2}\left(\frac{8}{N_A^2} + \frac{8}{N_B^2}\right) = O\left(\frac{1}{N^2}\right)$, and $g \coloneqq \frac{1}{2}\left(\frac{32}{3N_A^3} + \frac{32}{3N_B^3}\right) = O\left(\frac{1}{N^3}\right)$. We substitute these definitions into the expansion of $\log\left(\frac{D_A}{D}\right)$:

$$\log\left(\frac{D_A}{D}\right) = \log\left(\frac{2c^{3/2}}{\pi^{3/2}}\right) - c\left(\sum_{i=1}^{4} m_i^2\right) - d\left(\sum_{i=1}^{4} m_i^3\right) + f\left(\sum_{i=1}^{4} m_i^2\right) - g\left(\sum_{i=1}^{4} m_i^4\right) + \frac{5}{4N} - \frac{5}{4N_A} - \frac{5}{4N_B} + \mathcal{O}\left(N^{-3/2}\right). \tag{C.13}$$

Exponentiating each side yields

$$\frac{D_A}{D} = 2\left(\frac{c}{\pi}\right)^{\frac{3}{2}} \exp\left(-c\sum_{i=1}^{4} m_i^2\right)\left[1 - d\left(\sum_{i=1}^{4} m_i^3\right) + \frac{d^2}{2}\left(\sum_{i=1}^{4} m_i^3\right)^2 + f\left(\sum_{i=1}^{4} m_i^2\right) - g\left(\sum_{i=1}^{4} m_i^4\right) + \frac{5}{4N} - \frac{5}{4N_A} - \frac{5}{4N_B} + \mathcal{O}\left(N^{-3/2}\right)\right]. \tag{C.14}$$

We check that this function is normalized to $O(N^{-3/2})$ (as $\frac{D_A}{D}$ should be normalized), but omit the check from this appendix.

Having approximated the first factor in the state-counting term (C.11), we address the second, $\log\left(\frac{D_A}{d_A D}\right)$. By Stirling's approximation (C.15),

$$\log(n) = n\log(n) - n + \frac{1}{2}\log(2\pi n) + \frac{1}{12n} + \mathcal{O}\left(n^{-2}\right), \tag{C.15}$$

the logarithm is

$$\begin{aligned}\log\left(\frac{D_A}{d_A D}\right) = & -N\log(4) + \frac{N_B}{4}\log\left(\frac{N_B^4}{\left(\frac{N_B}{4}-m_1\right)\left(\frac{N_B}{4}-m_2\right)\left(\frac{N_B}{4}-m_3\right)\left(\frac{N_B}{4}-m_4\right)}\right) \\ & + m_1\log\left(\frac{N_B}{4}-m_1\right) + m_2\log\left(\frac{N_B}{4}-m_2\right) + m_3\log\left(\frac{N_B}{4}-m_3\right) \\ & + m_4\log\left(\frac{N_B}{4}-m_4\right) + \frac{1}{2}\log\left(\frac{N_B(\frac{N}{4})^4}{N\left(\frac{N_B}{4}-m_1\right)\left(\frac{N_B}{4}-m_2\right)\left(\frac{N_B}{4}-m_3\right)\left(\frac{N_B}{4}-m_4\right)}\right) \\ & + \frac{5}{4N} + \frac{1}{12N_B} - \frac{1}{12\left(\frac{N_B}{4}-m_1\right)} - \frac{1}{12\left(\frac{N_B}{4}-m_2\right)} - \frac{1}{12\left(\frac{N_B}{4}-m_3\right)} \\ & - \frac{1}{12\left(\frac{N_B}{4}-m_4\right)} + \mathcal{O}\left(N^{-3/2}\right).\end{aligned} \tag{C.16}$$

We Taylor-approximate about $N = \infty$ and reorganize:

$$\begin{aligned}\log\left(\frac{D_A}{d_A D}\right) = & -N_A\log(4) + \frac{3}{2}\log\left(\frac{N}{N_B}\right) + \sum_i\left(-\frac{2m_i^2}{N_B} - \frac{8m_i^3}{3N_B^2} + \frac{4m_i^2}{N_B^2} - \frac{16m_i^4}{3N_B^3}\right) + \frac{5}{4N} \\ & - \frac{5}{4N_B} + \mathcal{O}\left(N^{-3/2}\right).\end{aligned} \tag{C.17}$$

The logarithm approximation (C.14) and the ratio approximation (C.17) can now be substituted into the state-counting term (C.11). The summand varies slowly where its value is large, so we approximate the sum as an integral. Also, the integrand falls off quickly enough at large $|A_k|$ that we approximate the limits as $\pm\infty$. Evaluating the resulting Gaussian integrals, we obtain the commuting-charge state-counting term:

$$S(\langle\rho_A\rangle_{\mathcal{C}_0}) = N_A \log(4) - \frac{3}{2}\log\left(\frac{N}{N_B}\right) + \frac{3N_A}{N} + \frac{3N_A}{4N^2} - \frac{N_A^2}{2N^2 N_B} + \mathcal{O}\left(N^{-3/2}\right). \quad \text{(C.18)}$$

C.1.3 Noncommuting-charge model's state-counting term

The noncommuting charges share exactly one eigenspace, $\mathcal{N}_0$, specified as follows. Recall that the a qubits' total-spin-squared operator, $\vec{S}_a^2$, has eigenvalues $s(s+1)$. Consider tensoring the a qubits' $s = 0$ eigenspace onto the b qubits' full Hilbert space. The product is the eigenvalue-0 eigenspace shared by $Q_{1,2,3}^{\text{tot}}$.

We calculate first the a qubits' contribution to the state-counting term, then the b qubits' contribution (App. C.1.3). In App. C.1.3, we approximate the state-counting term to order $\mathcal{O}(N^{-1})$, as is necessary for identifying differences from the commuting-charge model.

Exact expression for the noncommuting-charge model's state-counting term

First, we calculate the a qubits' contribution to the state-counting term. By the rules for angular-momentum addition, $s = |s_A - s_B|, |s_A - s_B| + 1, \ldots, s_A + s_B$. Therefore, $s = m = 0$ only if $|s_A - s_B| = 0$—equivalently, only if $s_A = s_B$ and $m_A = -m_B$. This restriction constrains the global system to a subspace $\mathcal{N}_0$ of dimensionality

$$D = C_{\frac{N}{2},\frac{N}{2}} = \frac{1}{\frac{N}{2}+1}\binom{N}{\frac{N}{2}}. \quad \text{(C.19)}$$

We now choose a basis for this subspace. A natural choice consists of states with quantum numbers $s_A = s_B$. If $s_A = s_B = 0$, these basis states are tensor products. However, almost all the basis states correspond to $s_A = s_B > 0$ and encode entanglement between A and B, unlike the basis states chosen for the commuting-charge model. The noncommuting-charge basis states Schmidt-decompose as

$$|s_A, i, j\rangle = \sum_{m_A=-s_A}^{s_A} \frac{(-1)^{m_A}}{\sqrt{2s_A+1}} |s_A, m_A, i\rangle_A |s_B{=}s_A, m_B{=}-m_A, j\rangle_B. \quad \text{(C.20)}$$

The i indexes the elements of an arbitrary orthonormal basis for the subsystem-A subspace associated with the quantum numbers s_A and m_A. This subspace is of dimensionality

$$d_A = C_{\frac{N_A}{2}+s_A, \frac{N_A}{2}-s_A} = \frac{2s_A+1}{\frac{N_A}{2}+s_A+1} \binom{N_A}{\frac{N_A}{2}-s_A} . \tag{C.21}$$

The j in (C.20) indexes the elements of an arbitrary orthonormal basis for the subsystem-B subspace associated with the quantum numbers s_B and m_B. This subspace is of dimensionality

$$d_B = C_{\frac{N_B}{2}+s_B, \frac{N_B}{2}-s_B} = \frac{2s_B+1}{\frac{N_B}{2}+s_B+1} \binom{N_B}{\frac{N_B}{2}-s_B} . \tag{C.22}$$

The global system's maximally mixed state is

$$\langle \rho \rangle_{\mathcal{N}_0} = \frac{1}{D} \sum_{s_A,i,j} |s_A, i, j\rangle\langle s_A, i, j| \ . \tag{C.23}$$

Tracing out subsystem B yields

$$\langle \rho_A \rangle_{\mathcal{N}_0} = \frac{1}{D} \sum_{s_A,m_A,i} \frac{d_B}{2s_A+1} |s_A, m_A, i\rangle\langle s_A, m_A, i| . \tag{C.24}$$

Taking the spectral decomposition, we calculate the state's entropy and so the a qubits' contribution to the state-counting term:

$$S(\langle \rho_A \rangle_{\mathcal{N}_0}) = -\sum_{s_A=0}^{\frac{N_A}{2}} \frac{d_A d_B}{D} \log\left(\frac{d_B}{D(2s_A+1)}\right) \tag{C.25}$$

$$= -\sum_{s_A=0}^{\frac{N_A}{2}} \left(\frac{N}{2}+1\right) \frac{\left(\frac{N}{2}\right)!\left(\frac{N}{2}\right)!}{N!} \left(\frac{2s_A+1}{\frac{N_A}{2}+s_A+1}\right) \left(\frac{2s_A+1}{\frac{N_B}{2}+s_A+1}\right) \binom{N_A}{\frac{N_A}{2}-s_A}$$
$$\times \binom{N_B}{\frac{N_B}{2}-s_A} \log\left(\frac{\left(\frac{N}{2}\right)!\left(\frac{N}{2}\right)!}{N!} \frac{\left(\frac{N}{2}+1\right)}{\left(\frac{N_B}{2}+s_A+1\right)} \binom{N_B}{\frac{N_B}{2}-s_A}\right) . \tag{C.26}$$

We now calculate the b qubits' contribution. N_A unconstrained qubits have a state-counting term of $N_A \log(2)$. Adding $N_A \log(2)$ to Eq. (C.26) yields the noncommuting-

charge state-counting term:

$$S(\langle\rho_A\rangle_{\mathcal{N}_0}) = N_A \log(2) - \sum_{s_A=0}^{\frac{N_A}{2}} \left(\frac{N}{2}+1\right) \frac{\left(\frac{N}{2}\right)!\left(\frac{N}{2}\right)!}{N!} \left(\frac{2s_A+1}{\frac{N_A}{2}+s_A+1}\right)\left(\frac{2s_A+1}{\frac{N_B}{2}+s_A+1}\right) \times \binom{N_A}{\frac{N_A}{2}-s_A}\binom{N_B}{\frac{N_B}{2}-s_A} \times \log\left(\frac{\left(\frac{N}{2}\right)!\left(\frac{N}{2}\right)!}{N!}\frac{(\frac{N}{2}+1)}{(\frac{N_B}{2}+s_A+1)}\binom{N_B}{\frac{N_B}{2}-s_A}\right). \tag{C.27}$$

Closed-form approximation to the noncommuting-charge model's state-counting term

First, we approximate the $\frac{d_A d_B}{D}$ in Eq. (C.25) as a Gaussian function. We break $\frac{d_A d_B}{D}$ into two factors, one consisting of factorials and the other of everything else: $\frac{d_A d_B}{D} = f(s_A)g(s_A)$, wherein

$$f(s_A) \coloneqq \frac{\left(\frac{N}{2}\right)!\left(\frac{N}{2}\right)!}{(N)!} \frac{(N_A)!}{\left(\frac{N_A}{2}+s_A\right)!\left(\frac{N_A}{2}-s_A\right)!} \frac{(N_B)!}{\left(\frac{N_B}{2}+s_B\right)!\left(\frac{N_B}{2}-s_B\right)!} \quad \text{and} \tag{C.28}$$

$$g(s_A) \coloneqq \left(\frac{2s_A+1}{\frac{N_A}{2}+s_A+1}\right)\left(\frac{2s_A+1}{\frac{N_B}{2}+s_A+1}\right)\left(\frac{N}{2}+1\right). \tag{C.29}$$

We Taylor-expand $\log\big(f(s_A)\big)$ around its maximum, $s_A = 0$, to $\mathcal{O}\left(N^{-1}\right)$, assuming $s_A^2 \sim N$. Then, we exponentiate the result:

$$f(s_A) = \sqrt{\frac{2N}{N_A N_B \pi}} \exp\left(\frac{-2Ns_A^2}{N_A N_B}\right)\left[1 + \frac{1}{4N} - \frac{1}{4N_A} - \frac{1}{4N_B} + \frac{2s_A^2}{N_A^2} + \frac{2s_A^2}{N_B^2} - \frac{4s_A^4}{3N_A^3} - \frac{4s_A^4}{3N_B^3} + \mathcal{O}\left(N^{-2}\right)\right]. \tag{C.30}$$

Next, we expand $g(s_A)$ [Eq. (C.29)]:

$$g(s_A) = \frac{8Ns_A^2}{N_A N_B}\left[1 + \frac{1}{s_A} - \frac{2s_A}{N_A} - \frac{2s_A}{N_B} + \frac{2}{N} - \frac{4}{N_A} - \frac{4}{N_B} + \frac{1}{4s_A^2} + \frac{4s_A^2}{N_A^2} + \frac{4s_A^2}{N_B^2} + \frac{4s_A^2}{N_A N_B} + \mathcal{O}\left(N^{-3/2}\right)\right]. \tag{C.31}$$

The right-hand sides of (C.30) and (C.31) multiply to

$$\frac{d_A d_B}{D} = \frac{4(2N)^{\frac{3}{2}}}{(N_A N_B)^{\frac{3}{2}}\sqrt{\pi}}\, s_A^2 \exp\left(\frac{-2Ns_A^2}{N_A N_B}\right)\left[1 + \frac{1}{s_A} - \frac{2Ns_A}{N_A N_B} + \frac{9}{4N} - \frac{17N}{4N_A N_B} + \frac{6s_A^2}{N_A^2} + \frac{6s_A^2}{N_B^2} + \frac{4s_A^2}{N_A N_B} + \frac{1}{4s_A^2} - \frac{4s_A^4}{3N_A^3} - \frac{4s_A^4}{3N_B^3} + \mathcal{O}\left(N^{-3/2}\right)\right]. \tag{C.32}$$

We check that this function is normalized to $O(N^{-3/2})$ (as $\frac{d_A d_B}{D}$ must be normalized), but omit the details of the check.

Having approximated the first factor in the state-counting term (C.25), we proceed to the second. According to the Stirling approximation (C.15), the logarithm is

$$\begin{aligned}\log\left(\frac{d_B}{D(2s_A+1)}\right) = & -N\log(2) + \frac{N_B}{2}\log\left(\frac{N_B^2}{\left(\frac{N_B}{2}-s_A\right)\left(\frac{N_B}{2}+s_A\right)}\right) + s_A \log\left(\frac{\frac{N_B}{2}-s_A}{\frac{N_B}{2}+s_A}\right) \\ & + \frac{1}{2}\log\left(\frac{NN_B}{4\left(\frac{N_B}{2}-s_A\right)\left(\frac{N_B}{2}+s_A\right)}\right) + \log\left(\frac{\frac{N}{2}+1}{\frac{N_B}{2}+s_A+1}\right) \\ & + \frac{1}{4N} + \frac{1}{12N_B} - \frac{1}{12\left(\frac{N_B}{2}-s_A\right)} - \frac{1}{12\left(\frac{N_B}{2}+s_A\right)} + \mathcal{O}\left(N^{-2}\right).\end{aligned} \tag{C.33}$$

Taylor-approximating about $N = \infty$ yields

$$\begin{aligned}\log\left(\frac{d_B}{D(2s_A+1)}\right) = & -N_A\log(2) + \frac{3}{2}\log\left(\frac{N}{N_B}\right) - \frac{2s_A^2}{N_B} - \frac{2s_A}{N_B} - \frac{4s_A^4}{3N_B^3} + \frac{4s_A^2}{N_B^2} + \frac{9}{4N} - \frac{9}{4N_B} \\ & + \mathcal{O}\left(N^{-3/2}\right).\end{aligned} \tag{C.34}$$

We can now substitute the logarithm (C.34) and the $d_A d_B/D$ factor (C.32) into the state-counting term (C.25). Since the summand varies slowly where its value is large, we approximate the sum as an integral. Also, since the integrand falls off rapidly at large s_A, we approximate the integral's upper limit with ∞. Evaluating the integral, we calculate the a qubits' contribution to the state-counting term. Adding the b qubits' state-counting term, $N_A \log(2)$, we obtain the noncommuting-charge state-counting term:

$$\langle S_{\mathrm{E}} \rangle_{\mathcal{S}} = N_A \log(4) - \frac{3}{2}\log\left(\frac{N}{N_B}\right) + \frac{3N_A}{2N} + \frac{3N_A}{4N^2} + \frac{N_A^2}{2N^2 N_B} + \mathcal{O}\left(N^{-3/2}\right). \tag{C.35}$$

C.2 How our models' charges restrict the microcanonical subspaces

The main text posits an explanation for why, in the microcanonical-subspace study, the noncommuting-charge Page curve lies above the commuting-charge Page curve. We propose another explanation, using specifics of our models, here. To what extent this reasoning generalizes beyond those models merits further study.

Consider beginning with an unconstrained system, then restricting the Hilbert space to the eigenvalue-0 eigenspace of $Q_1^{\rm tot}$, then restricting further to the eigenvalue-0 eigenspace of $Q_2^{\rm tot}$, then restricting to the eigenvalue-0 eigenspace of $Q_3^{\rm tot}$. The first two restrictions already restrict the system to the $s = 0$ subspace; the third restriction is redundant.

Now, consider undertaking the same process but replacing the $Q_\alpha^{\rm tot}$'s with $C_\alpha^{\rm tot}$'s. The first two restrictions only partially imply the third, which therefore constrains the Hilbert space nontrivially. (Appendix C.2.1 contains a proof.) One might therefore expect the microcanonical subspace to be larger when defined by our three noncommuting charges than when defined by our three commuting charges. We have confirmed this expectation by direct calculation. Furthermore, the available Hilbert space's dimensionality upper-bounds the entanglement entropy [Eq. (4.1)]. Hence the noncommuting charges should enable more entanglement—a higher Page curve—than the commuting charges do.

C.2.1 Constraining $C_1^{\rm tot}$ and $C_2^{\rm tot}$ constrains $C_3^{\rm tot}$ only partially

Consider an unconstrained system of N 4-level qudits. Consider restricting the Hilbert space to the eigenvalue-0 eigenspace of $C_1^{\rm tot}$, then restricting further to the eigenvalue-0 eigenspace of $C_2^{\rm tot}$, and then restricting to the eigenvalue-0 eigenspace of $C_3^{\rm tot}$. The first two restrictions partially imply the third, which constrains the Hilbert space nontrivially. We prove this claim here.

The local charges $C_{1,2,3}$ share four eigenstates, the maximally entangled Bell states [37]. They are, if $|\uparrow\rangle$ and $|\downarrow\rangle$ denote the Z eigenstates,

$$|\mathcal{B}_1\rangle := \frac{1}{\sqrt{2}} \left(|\downarrow\rangle_a |\uparrow\rangle_b - |\uparrow\rangle_a |\downarrow\rangle_b \right), \quad |\mathcal{B}_2\rangle := \frac{1}{\sqrt{2}} \left(|\downarrow\rangle_a |\downarrow\rangle_b - |\uparrow\rangle_a |\uparrow\rangle_b \right), \tag{C.36}$$

$$|\mathcal{B}_3\rangle := \frac{1}{\sqrt{2}} \left(|\downarrow\rangle_a |\downarrow\rangle_b + |\uparrow\rangle_a |\uparrow\rangle_b \right), \quad \text{and} \quad |\mathcal{B}_4\rangle := \frac{1}{\sqrt{2}} \left(|\downarrow\rangle_a |\uparrow\rangle_b + |\uparrow\rangle_a |\downarrow\rangle_b \right). \tag{C.37}$$

Denote by ρ_j the j^{th} qubit's reduced state, which has a weight $\langle \mathcal{B}_k | \rho_j | \mathcal{B}_k \rangle$ on the k^{th} Bell state. Summing over qudits yields the total population $P_k \coloneqq \sum_{j=1}^{N} \langle \mathcal{B}_k | \rho_j | \mathcal{B}_k \rangle$.

If the system is in an eigenvalue-0 eigenstate of C_1^{tot}, then $P_1 + P_2 = P_3 + P_4$. If the system is in an eigenvalue-0 eigenstate of C_2^{tot}, then $P_1 + P_3 = P_2 + P_4$. Together, these constraints imply $P_1 = P_4$ and $P_2 = P_3$. Furthermore, $\langle C_3^{\text{tot}} \rangle = P_2 + P_3 - P_1 - P_4$. This expectation value, under the $C_{1,2}^{\text{tot}}$ constraints, is restricted to $2(P_2 - P_1)$, which need not vanish. Thus, the first two charges do not restrict the C_3^{tot} expectation value completely. Contrarily, if in an eigenstate of $Q_{1,2}^{\text{tot}}$, the system is in the eigenvalue-0 eigenstate of Q_3^{tot}. Hence $C_{1,2}^{\text{tot}}$ restrict the Hilbert space less than $Q_{1,2}^{\text{tot}}$ do.

C.3 How sequentially introduced charges change the Page curve: superadditively, subadditively, or additively

Figure 4.2 shows Page curves constructed from microcanonical subspaces. At finite N, the curves violate an expectation that one might gather from earlier literature. We explain the expectation, discuss the violation, and provide numerical evidence for the expectation in the thermodynamic limit (as $N \to \infty$).

Consider beginning with an unconstrained N-site system, restricting the Hilbert space to the eigenvalue-0 eigenspace of C_1^{tot}, then restricting further to the eigenvalue-0 eigenspace of C_2^{tot}, and then restricting to the eigenvalue-0 eigenspace of C_3^{tot}. One might expect that, as more charges were introduced, each successive charge would lower the Page curve by the same amount as the last charge. Such lowering has been argued to happen in the thermodynamic limit, with commuting charges [104]. We call an expectation of such lowering the *additivity ansatz*. One might posit it, expanding on [104], (i) for noncommuting charges in the thermodynamic limit and (ii) for commuting and noncommuting charges at finite N.

If the additivity ansatz were true, the Page curve (for three equivalent commuting or noncommuting charges) could be constructed as follows. Consider restricting the global Hilbert space to one charge's eigenvalue-0 eigenspace (any C_α^{tot} or Q_α^{tot}—which one does not affect the curve). The corresponding Page curve, we denote by $\langle S_{\text{E}} \rangle_{\mathcal{S}}^{(1)}$. Recall that $\langle S_E \rangle_{\mathcal{H}}$ denotes the unrestricted Page curve. The additivity ansatz predicts the Page curve $\langle S_E \rangle_{\mathcal{H}} - 3 \left(\langle S_E \rangle_{\mathcal{H}} - \langle S_{\text{E}} \rangle_{\mathcal{S}}^{(1)} \right)$ for our models with three equivalent charges constrained in

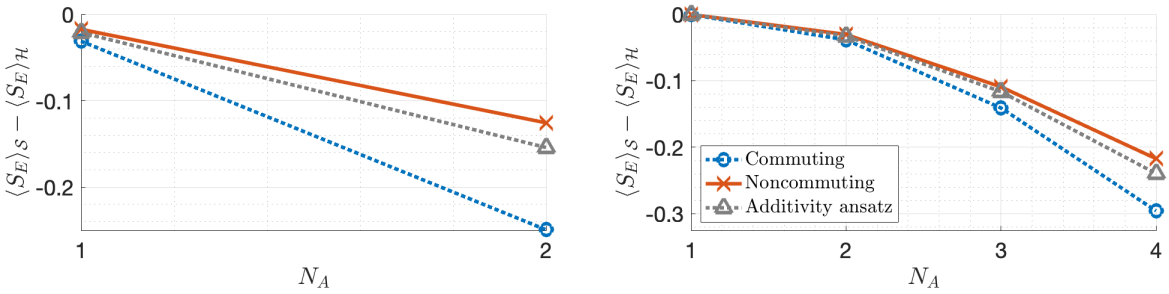

Figure C.1: **Testing the additivity ansatz.** $\langle S_{\rm E} \rangle_{\mathcal{S}}$ denote any Page curve restricted by charges; and $\langle S_E \rangle_{\mathcal{H}}$, the unrestricted Page curve. The red x's form the noncommuting-charge model's Page curve, and the circular blue markers form the commuting-charge model's Page curve. Both curves were calculated using microcanonical subspaces. The gray triangles illustrate the additivity ansatz.

each.

Figure C.1 tests this prediction at finite N. The gray triangles form the additivity-ansatz curve. It lies below the noncommuting-charge Page curve (red x's), which are therefore superadditive. The ansatz curve also lies above the commuting-charge Page curve (blue circles), which are subadditive. Hence the additivity ansatz breaks in a commutation-dependent manner at finite N. However, all three curves converge as N grows. We hence provide numerical evidence for the additivity ansatz, supported analytically in [104] and in App. C.1 above, in the thermodynamic limit.

C.4 Analogous approximate microcanonical subspaces

The main text specifies how to construct AMC subspaces in the noncommuting-charge model. We augment this explanation with examples. Then, we explain how to construct analogous AMC subspaces in the commuting-charge model. We also specify the six analogous-AMC-subspace pairs reported in the main text.

First, we review how to construct AMC subspaces in the noncommuting-charge model. Denote by $2m$ the $Z_a^{\rm tot}$ eigenvalue. $Z_a^{\rm tot}$ shares eigenstates with $\vec{S}_a^2$. Shared eigenstates labeled by the same two quantum numbers form the (s, m) *eigenspace*. Some such eigenspaces are AMC subspaces, we find by direct calculation. For each (s, m) value, we calculate the probability distributions $p_\alpha^{\mathcal{N}}(\gamma)$. Each distribution should exhibit one peak for the eigenspace to satisfy the AMC subspace's definition. $p_3^{\mathcal{N}}(\gamma)$, being a Kronecker delta function in the (s, m) subspace, meets this criterion. Also, according to direct calcula-

(s, m)	Possible measurement outcomes								
	-4	-3	-2	-1	0	1	2	3	4
$(1, 0)$				0.500	0	0.500			
$(1, 1)$				0.250	0.500	0.250			
$(2, 0)$			0.375	0	0.250	0	0.375		
$(2, 1)$			0.250	0.250	0	0.250	0.250		
$(2, 2)$			0.063	0.250	0.375	0.250	0.063		
$(3, 0)$		0.313	0	0.188	0	0.188	0	0.313	
$(3, 1)$		0.234	0.156	0.016	0.188	0.016	0.156	0.234	
$(3, 2)$		0.094	0.250	0.156	0	0.156	0.250	0.094	
$(3, 3)$		0.016	0.094	0.234	0.313	0.234	0.094	0.016	
$(4, 0)$	0.273	0	0.156	0	0.141	0	0.156	0	0.273
$(4, 1)$	0.219	0.109	0.031	0.141	0	0.141	0.031	0.109	0.219
$(4, 2)$	0.109	0.219	0.063	0.031	0.156	0.031	0.063	0.219	0.109
$(4, 3)$	0.031	0.141	0.219	0.109	0	0.109	0.219	0.141	0.031
$(4, 4)$	0.004	0.031	0.109	0.219	0.273	0.219	0.109	0.031	0.004

Table C.1: **Probabilities $p_1^{\mathcal{N}}(\gamma)$ that characterize (s, m) eigenspaces.** Denote by $|\psi\rangle$ any state from an (s, m) eigenspace of the noncommuting-charge model. Measuring Q_1^{tot} yields outcome γ with some probability. This probability, averaged over the $|\psi\rangle$, we denote by $p_1^{\mathcal{N}}(\gamma)$. The possible measurement outcomes range from $-s$ to s. The probabilities $p_1^{\mathcal{N}}(\gamma)$ are listed for each (s, m) and are independent of the system size, N. $p_1^{\mathcal{N}}(\gamma)$ has exactly one peak only if $s = m$.

tion, $p_1^{\mathcal{N}}(\gamma) = p_2^{\mathcal{N}}(\gamma)$ for all γ. Hence we need calculate only $p_1^{\mathcal{N}}(\gamma)$ to check whether an (s, m) eigenspace is an AMC subspace. Table C.1 presents these distributions for $s \leq 4$. Whenever $s = m$, each distribution exhibits one peak. Therefore, each $(s, m{=}s)$ subspace qualifies as an AMC subspace.

Having identified AMC subspaces defined by noncommuting charges, we construct analogs defined by commuting charges. For each N, we identify the eigenspaces shared by $C_{1,2,3}^{\text{tot}}$. For consistency with the noncommuting-charge model, we keep only the eigenvalue-m eigenspaces of C_3^{tot}. For each shared eigenspace, we calculate the distributions $p_\alpha^{\mathcal{C}}(\gamma)$. If they equal their noncommuting-charge counterparts $p_\alpha^{\mathcal{N}}(\gamma)$ (criterion 5), the eigenspace forms an analogous AMC subspace.

An illustrative example is parameterized by $N = 8$ and (in the noncommuting-charge model) $s = m = 1$. We keep only the eigenvalue-1 eigenspaces of C_3^{tot}. Denote by c_x the C_1^{tot}

N	$s = m$	NC	C	NC − C	% diff.
4	1	−0.455	−0.479	0.024	5.112
8	1	−0.364	−0.390	0.027	7.106
2	$N/2$	−0.587	−0.589	0.002	0.362
4	$N/2$	−1.350	−1.354	0.004	0.272
6	$N/2$	−2.074	−2.086	0.012	0.600
8	$N/2$	−2.770	−2.788	0.017	0.625

Table C.2: **Differences between Page curves, constructed from approximate microcanonical subspaces, at $N_A = N/2$.** The Page curves' values at $N_A = N/2$ are listed for various N and $s = m$ values. We abbreviate "difference" with "diff.," "noncommuting" with "NC," and "commuting" with "C."

eigenvalues and by c_y the C_2^{tot} eigenvalues. We label by $(c_x, c_y, 1)$ the eigenspaces shared by $C_{1,2,3}^{\text{tot}}$. For consistency with the noncommuting-charge model, we ignore any eigenspaces in which $c_x > s$ or $c_y > s$. Four eigenspaces remain: $(0, -1, 1)$, $(-1, 0, 1)$, $(1, 0, 1)$, and $(0, 1, 1)$. Each is of dimensionality 1680. The candidate AMC subspace is the union of these four subspaces and is of dimensionality 6720. These dimensionalities fix the probabilities $p_1^{\mathcal{C}}(\gamma)$. For example, $p_1^{\mathcal{C}}(0) = (1680 \times 2)/6720 = 0.5$. The remaining probabilities are $p_1^{\mathcal{C}}(-1) = 0.25$ and $p_1^{\mathcal{C}}(1) = 0.25$. This distribution equals the corresponding $p_1^{\mathcal{N}}(\gamma)$. Checking every eigenvalue-m eigenspace of C_3^{tot}, we find six eigenspaces for which $p_\alpha^{\mathcal{C}}(\gamma) = p_\alpha^{\mathcal{N}}(\gamma)$ $\forall \alpha, \gamma$, satisfying criterion 5.

We have identified six pairs of parallel (commuting-charge and noncommuting-charge) AMC subspaces. The pairs are labeled by $s = m = 1, N/2$ and $N = 4, 8$, as well as by $s = m = N/2$ and $N = 2, 6$. (Computational limitations restrict us to $N \leq 8$.) Table C.2 compares the two Page curves formed from each subspace pair. We compare the curves at their midpoints, $N_A = N/2$. The percent difference between the two curves varies from 0.199% to 3.06% across the subspace pairs. Hence noncommuting charges increase the average entanglement entropy in AMC subspaces as in microcanonical subspaces.

Appendix D

Appendices for "Noncommuting charges induce a critical phase in monitored quantum circuits"

D.1 Additional numerics elucidating the entanglement dynamics and spin sharpening

In Fig. 5.2, we plot $\log(S_A)$ [see Eq. (5.3)] against t/L^2. We claimed the different-L curves collapse for $p > p_c \approx 0.35$ and presented the plots for up to $p = 0.4$. To confirm that the curves remain collapsed for larger p we plot $p = 0.6, 0.8$, and 1.0 in Fig. D.1.

In Sec. 5.3.2, we claimed that L^2 time steps suffice for the bipartite entanglement entropy, S_f, to plateau. Figure D.2 justifies this claim, presenting S_f as a function of $\log(t)$ for $\leq L^2$ time steps at the extreme values $p = 0, 1$. At both extrema, S_f stops changing (to within minor fluctuations) by L^2 time steps.

Section 5.4 claimed that our $p > p_\#$ data are compatible with a sharpening time scale $\sim L^2$ deep in the critical phase. Figure D.3 justifies this claim. We plot $\log(S_A)$ against t/L^2 at various p values. The initial collapse occurs at $p > p_\#$. The L=8 numerics deviate from the collapse when $p \in [0.35, 0.45] \cup [0.8, 1]$. We suspect that these deviations arise from finite-size effects.

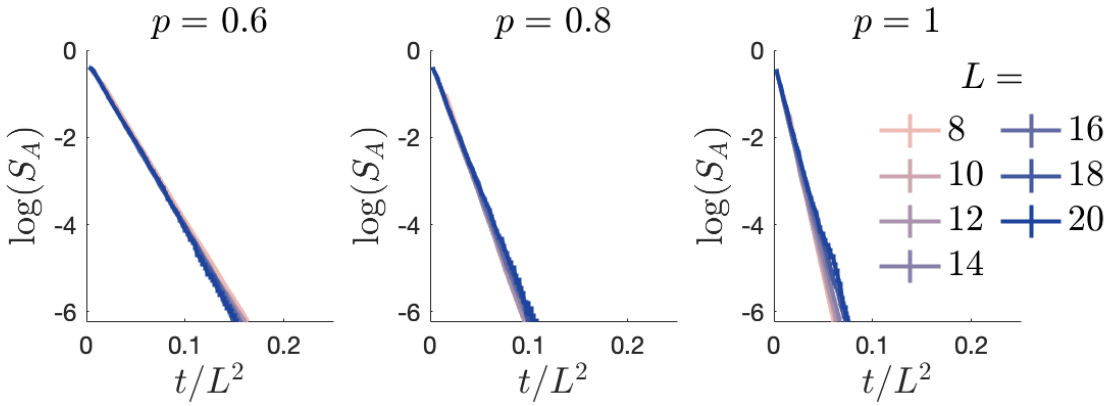

Figure D.1: **The purification time still reveals a $z = 2$ phase for $p > 0.4$.** The entropy S_A quantifies the ancilla qubit's entanglement with the system. We plot $\log(S_A)$ for clarity, as S_A decays exponentially. t/L^2 runs along the x-axis to demonstrate the existence of a phase in which the system purifies over a time scale $t_{\mathrm{P}} \sim L^2$. We used 30 000 samples when $L = 8$ to 16; 10 000 samples when $L = 18$; and 1 500 samples when $L = 20$. The y-axis's lower limit is $\log(10^{-3}) \approx -6.91$.

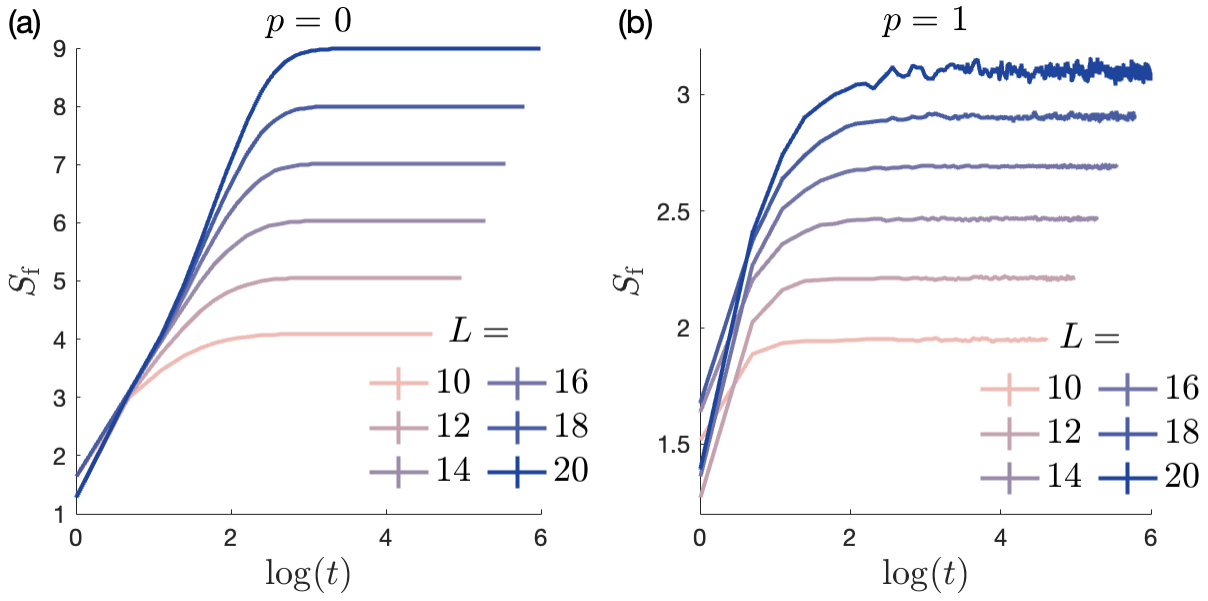

Figure D.2: **The bipartite entanglement entropy saturates after L^2 time steps.** At the extreme p values $p = 0, 1$, S_{f} quits changing (to within minor fluctuations).

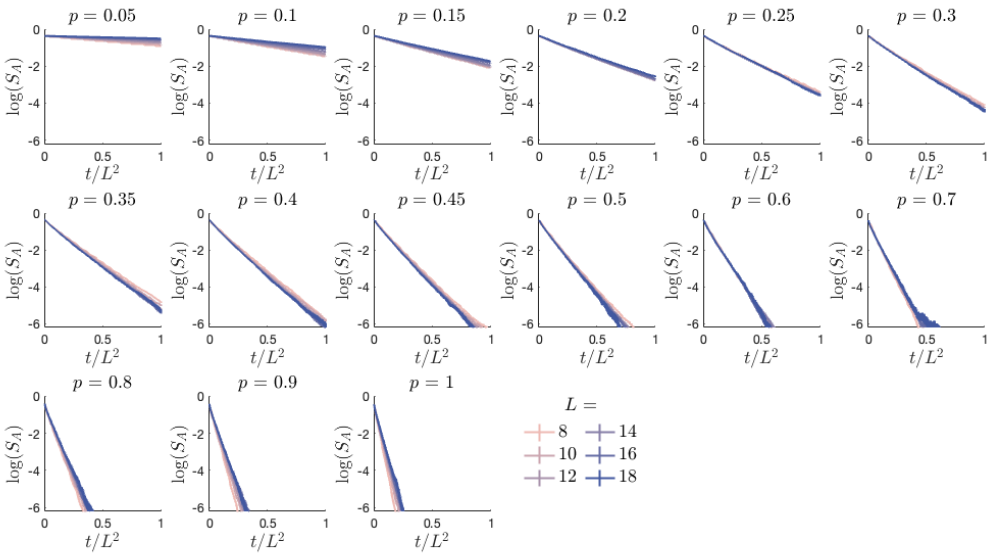

Figure D.3: **In the critical phase, the numerics are consistent with a $\sim L^2$ sharpening time scale.** The entropy S_A quantifies the ancilla qubit's entanglement with the system. We plot $\log(S_A)$ for clarity, as S_A decays exponentially. t/L^2 runs along the x-axis to demonstrate the numerics are consistent with a $\sim L^2$ sharpening time scale. We used 30 000 samples when $L = 8$ to 14; and 10 000 samples when $L = 16$ to $L = 18$. The y-axis's lower limit is $\log(10^{-3}) \approx -6.91$.

Index